Development of Polymeric Materials Chemistry via Physical Organic Simulations

by

Allison G. Roessler

A dissertation submitted in partial fulfillment
of the requirements for the degree of
Doctor of Philosophy
(Chemistry and Scientific Computing)
in the University of Michigan
2020

Doctoral Committee:

      Associate Professor Paul M. Zimmerman, Chair
      Professor Charles L. Brooks III
      Professor Krishnakumar Garikipati
      Professor Anne J. McNeil

Allison G. Roessler

kellyalg@umich.edu

ORCID iD: 0000-0002-1368-5374

Dedication

To my husband, Michael, who has never wavered in his belief in me.

I would be remiss if I did not mention my excellent undergraduate mentor, Jeff Rohde, who helped me realize my love for research and who has celebrated my successes every step of the way. It is my hope that I can inspire my own students in the same way that he has done for me and many others.

During my time in the Zimmerman Lab I have had the fortune to work with many brilliant and interesting lab mates who have livened my graduate school experience and who have inspired me. It was a joy to share a cubicle for three and a half years with Andy Vitek who was an excellent mentor and friend. I am grateful for his patience, for answering my many questions, and for many laughs. Thanks to Ian Pendleton for taking a genuine interest in my research and rooting for my success. To Amanda Dewyer, who made me laugh and made me think, I am grateful for the time spent editing my papers and talks and am grateful to have had another woman in the lab who welcomed me and challenged me. Josh Kammeraad is the most intelligent person I know, but more importantly, he is also the most generous. He has supported me throughout my Ph.D. from helping me through difficult coursework in my first few semesters to editing and workshopping ideas as I wrote my thesis. In addition to his professional support, Josh has been an excellent friend. To Matt Hannigan who has been a kindred spirit, I am so grateful to have had his listening ear and wise words during difficult times. I feel very lucky to have worked closely with him on a variety of projects both in and out of the lab. Matt and Josh have always been willing to let me bounce ideas off of them and both have contributed observations that have shaped many important aspects of this work. Finally, I have enjoyed sitting next to Nikki Perkins over the past year and a half and I wish her so much success.

The administrative staff in the Chemistry Department are top notch. I want to particularly thank Liz Oxford and Katie Foster who served as graduate coordinators during my time in the

Ph.D. He has been my sturdy shelter and has given me a wealth of encouragement and love. He kept me going when I did not know if I had it in me to go on. There are so many ways in which Michael contributed to this work behind-the-scenes, not least of which included him learning how to hunt down journal articles to add to my Mendeley library so I could cite them. Michael is the best person I know, and I feel very fortunate to have him in my corner. We will fondly look back on our newlywed years in Ann Arbor and I will never forget the many sacrifices he has made to allow me to pursue my education, career, and dreams. This is for you.

Table of Contents

List of Figures

List of Schemes

List of Tables

Abstract

Computational chemistry is an important and increasingly useful branch of chemistry. New technology has enabled faster and more accurate computations which allow researchers to quickly provide insights to experimentalists in real time. In order to do this, tools which allow for the discovery and prediction of new chemistries must be implemented. Chapter 1 provides an overview of computational chemistry and focuses on advancements in reaction discovery.

In chapter 2, these methods are applied to reactions that encompass a wide range of transformations from the field of mechanochemistry. Mechanically induced reactions often have unique selectivities or mechanisms compared to traditional means of activation (photo, catalytic, thermal) due to perturbations from the applied force to the underlying potential energy surface. Growing String Method with a newly developed force functionality proves to be useful in determining transition states and reaction paths on complicated, force-biased potential energy surfaces, and as a result, new chemistries are discovered. The ability to elucidate the details of three complex reactions is demonstrated in finding *cis* and *trans* isomers of the spiropyran to merocyanin transformation at varying magnitudes of force, in uncovering the fundamental means of flex mechanophore activation, and in showing the physical principles of force-transmittance through different polymer backbones.

Chapter 3 describes the first mechanistic study of the metal-free redox-mediated ring-opening metathesis polymerization (ROMP) process which yields poly(norbornene) of tunable *cis* and *trans* content. The ability to modulate product content is demonstrated by varying parameters

such as reaction conditions (solvent, temperature, time), counter anion size, and size and donating ability of the R-group on the initiator. The *trans* product is favored under most conditions, but product content can be shifted toward *cis* when the cation is sufficiently destabilized. Modifying the R-group on the initiator is found to be stereo-electronically important. Overall, computations provide key insights into the mechanism for stereoselectivity that allows for the potential to generate ROMP polymers with highly tunable microstructures.

In chapter 4, a bimetallic catalyst that yields highly isotactic poly (propylene oxide) is explored. The molecular geometry of the catalyst is determined to be in the closed conformation with head-to-tail stacking. A kink in the salen ligand is found to be energetically accessible. This geometric distortion may allow for less congested monomer addition and better molecular weight control. Computations are used to make a series of substitutions on the catalyst in order to establish structure-reactivity and structure-selectivity relationships. Chemical features such as S_N2 angle and bond formation distance are used to describe these relationships in the first detailed mechanistic exploration of this version of the catalyst.

The concluding chapter reflects on each of the projects described within the dissertation and discusses open areas for future consideration. Overall, this work outlines applications of modern computational tools to better understand polymeric materials chemistry.

Chapter 1. Introduction

Investigating Reaction Pathways with Computational Chemistry

Computational chemistry is used to study the fundamental properties of atoms, molecules, and chemical reactions using quantum mechanics and thermodynamics. A central goal of computational chemists is to integrate chemical theory and modeling with experimental data. Advances in the development of quantum mechanics (QM) and molecular dynamics (MD) methods and in computer power have increased the reliability and efficiency of computational modeling, making it possible to present complex analyses which can be used to design experiments, test predictions, and uncover important mechanistic details that illuminate experimental results.[1,2]

Density Functional Theory

Density functional theory (DFT) has emerged as a valuable tool in computing as its methods have proven to have a high accuracy to cost ratio. Due to DFT's efficiency, it has become an effective method for developing chemical understanding in cooperation with experimental studies by uncovering atomistic-level details of a chemical reaction. DFT can be used to obtain the geometries and relative energies of reactants, intermediates, products, and transition state structures along a reaction path. The energies can be used to explain or predict experimental activity and selectivity.

DFT methods are able to tackle large chemical systems because density functional methods use electron probability density of the system as opposed to the electronic wavefunction. This approximation allows DFT methods to circumvent the high-scaling cost of other high-accuracy

methods like coupled-cluster theory,[3,4] a numerical technique for describing many-body systems which is often considered the gold standard of quantum chemistry. The scaling for DFT is significantly better than for coupled cluster (N^3 for pure density functionals vs N^7 for coupled cluster).[5,6] The favorable low cost to high accuracy ratio makes DFT appealing for modeling a wide array of chemical systems including the ones presented within this document.[7–12]

In order to accurately model a chemical system with DFT methods, it is important to carefully chose appropriate functionals and basis sets. The functionals used to describe electron density vary in their approximations and therefore also in their suitability for handling various chemical reactions. While some functionals may be more suited to specific kinds of complexes, there are some functionals, such as B3LYP and others, which have been demonstrated to be applicable to a wide variety of systems.[13–15] Even these more comprehensive methods have their own challenges, however. B3LYP, for example, struggles to accurately model excited state transformations[16–18] or long range dispersion interactions between orbitals which account for the effect of distant orbitals on electron density.[15,19–23] Fortunately, a variety of methods for modeling these weak interactions have been developed to reduce these deficiencies. The addition of empirical dispersion corrections, for example, can be added to a functional.[22] These dispersion-corrected DFT methods improve the ability of DFT to accurately model reactions where long-range dispersion interactions play an important role.

Choosing an appropriate basis set is equally important. The basis set defines the orbitals in which the molecule's electrons can be occupied. Valence orbitals are essential, and polarization functions provide additional flexibility for electron density to adapt to an atom's molecular environment. Thus, for DFT calculations to be accurate, both the functional (level of theory), and the basis set must be carefully considered.

Despite some of the shortcomings of DFT, when appropriate functionals and basis sets are used, they have been demonstrated to accurately predict geometries that closely match experimentally determined geometries for polymers and transition metal systems relevant to this work.[24–28] Additionally, energetic calculations used to evaluate the thermodynamics and kinetics of a chemical system can be calculated within 2 kcal/mol for stable intermediates and within 5 kcal/mol for barrier heights when the right methods are applied.[1,29–39] These accurate energetic calculations have allowed DFT to be used to explain and predict chemical equilibria, relative rates, and stereoselectivity in a broad array of reactions.

Automated Reaction Discovery

Though big strides have been made by the computational chemistry community through the use of effective computational tools, many methods are still limited by what falls within the scope of traditional chemical intuition due to the necessity for input from a chemist. For many methods, the chemist must provide a guess structure for intermediates and transition states based on experimental data or on intuition they may have based on prior knowledge of how molecules tend to behave in similar systems. Many methods work best by evaluating previously hypothesized reaction steps and thus are not able to actually discover new chemistry. This means that traditionally, for new or unexpected reaction mechanisms, computation has not been able to provide a useful solution. This problem is further complicated if the mechanism is particularly challenging or nonobvious and proceeds through several reaction intermediates and transition states along the way. In these scenarios, if intermediates or unexpected side reactions are unable to be probed experimentally, then they are unlikely to be found using traditional computational methods.

Recently, a number of automated reaction discovery tools have been developed to help solve this problem. Automated reaction path finding has become increasingly important because of its ability to map a PES of interest and explore the relevant chemical space for unintuitive intermediates and transition states. The ability to readily uncover challenging and unexpected chemistries helps increase the speed at which progress can be made and allows for swift identification of structure-activity relationships. This means collaboration between computation and experiment can lead to understanding of reaction landscapes and more efficient optimization of advanced chemical systems.

This work describes the application of DFT and automated reaction discovery tools to uncover mechanistic details for complex chemical systems. Before discussing the applications of these methods in the following chapters, a brief introduction of the relevant background is discussed. While not exhaustive, the following will cover the relevant background material for the computational studies contained in this work. For a more detailed review, several thorough studies that examine current methods are available.

Chemical Space and Potential Energy Surfaces

Energy profiles are useful for understanding thermodynamic equilibrium, determining kinetic products and identifying minimum energy reaction paths. Figure 1-1 shows a representative reaction profile for a chemical reaction proceeding from the starting material (**A**) to the product species (**C**) through a transition state (**B**). The reaction profile is helpful for comparing relative energies of the various transition and stationary states found along the reaction path as the reaction progresses forward.

An energy profile is a cross section of the potential energy surface along the minimum energy reaction path as shown in Figure 1-1. A potential energy surface is a multi-dimensional surface that describes the energy of reactants as a function of their geometry. Computational tools allow for the efficient identification of stationary states along the PES. Once the relevant points on the PES are evaluated, they can be classified according to the first and second derivatives of the energy with respect to the position, which are the gradient and curvature, respectively. Stationary points, which have a gradient of zero, are minima and correspond to physically stable chemical species. Saddle points correspond to transition states, the highest energy point on the reaction coordinate.

Though the reactive space may be complex, when sampling the potential energy surface, it is of main importance to sample the relevant space to find low energy intermediates. Sampling relevant space but not the whole PES allows the computational chemist to quickly identify reaction intermediates and transition states at a low computational cost.
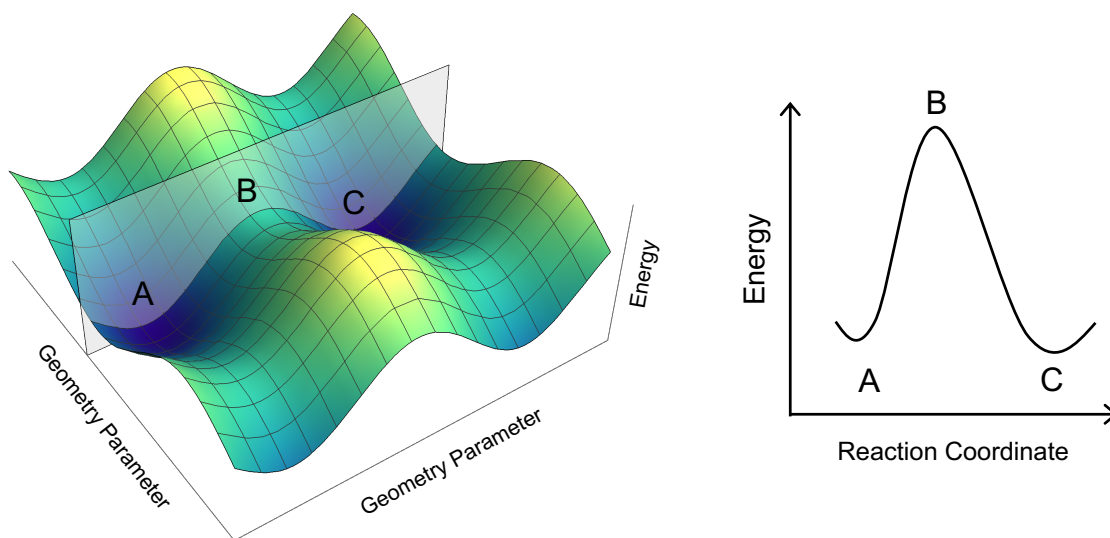
Figure 1-1. The energy profile on the right is a cross section of the potential energy surface on the left. Reactant species (A) proceeds through transition state (B) to arrive at product (C).

Thermodynamic and Kinetic Information from Potential Energy Surfaces

Once the energies of relevant species have been isolated, this information can be used to predict the efficiency of a reaction if it is thermodynamically controlled. Though in some systems experimental equilibrium constants may be trivial to obtain, in others there may be an equilibrium of reactive but unobservable intermediates that control the product distribution, and in these cases, computation is very valuable. For systems under thermodynamic control, computations can be used as a predictive tool with the equilibrium expression,

$$K_{eq} = e^{\frac{-\Delta G}{RT}}$$

where K_{eq} is the equilibrium constant for a reaction between chemical species [A] and [B], ΔG is the Gibbs free energy, T is the temperature, and R is the gas constant. The exponents σ and ρ correspond to the reaction order of [A] and [B], respectively. This example demonstrates how the calculated ΔGs can be used to predict experimentally observable quantities when reactions are under thermodynamic control.

The Eyring equation, shown below, relates transition state energies ($\Delta G^{\ddagger}$) with reaction rate, which describes reactions under kinetic control,

$$r_{A \to B} = \kappa \left(\frac{k_B T}{h}\right) e^{\frac{-\Delta G^{\ddagger}}{RT}}$$

where r is the rate of the reaction from A to B, κ is the transmission coefficient, k_B is the Boltzmann constant, T is temperature in Kelvin, h is Planck's constant, R is the gas constant, and $\Delta G^{\ddagger}$ is the transition state energy. The Eyring equation can be used to predict experimental reaction rates but computationally, it is typically more useful to predict relative rates of competing reactions so that they can be easily compared.

Transition State Finding Methods

While geometries for stable intermediates can be trivial to obtain, finding transition state (TS) structures has proven more challenging. Additionally, due to the high dimensionality of PESs, an exhaustive search of the chemical space is not feasible. Therefore, a method that only explores the local, relevant chemical space by finding low-energy intermediates and generating transition states that connect them is useful for low-cost, quick, and accurate TS finding.

There are two main methods for locating transition states. The first method includes local surface-walking algorithms[40–45] while the second includes interpolation methods.[46–55] Surface-walking algorithms start with a guess TS structure that is optimized until it meets the saddle point TS criteria. These calculations can be computationally intensive, especially if the guess structure is far from the true TS, which happens frequently if there is little information available about the TS structure. Interpolation methods generate TS structures between given reactant and product geometries. These methods are appealing because they require less user input and do not require an initial TS guess.

Two interpolation methods for TS finding in widespread use include the nudged elastic band method (NEB)[46–49] and growing string method (GSM).[50–55] NEB requires reactant and product geometries and generates an interpolated set of nodes (optimized geometries) to form a reaction path between the reactant and product points. Spring interaction between the neighboring nodes are used to create a continuous reaction path. GSM is described in comparison in the following section.

Transition State Finding via Growing String Method

GSM finds minimum energy reaction paths and TS structures by populating a reaction path with interpolated images, or nodes, between user-provided reactant and product geometries. For double-ended methods, nodes are added from both the reactant and product, growing strings toward a TS structure from both ends. In single-ended methods, only reactant geometry and driving coordinates that describe a desired reaction are required. The nodes are then added only from the reactant end to find both TS and product structures. In both cases, the generated nodes are optimized, reparametrized, and spaced along a reaction path. Once the string traverses a transition state region, the string is optimized to refine the reaction path and transition state. A figure demonstrating how single-ended GSM operates is provided below.
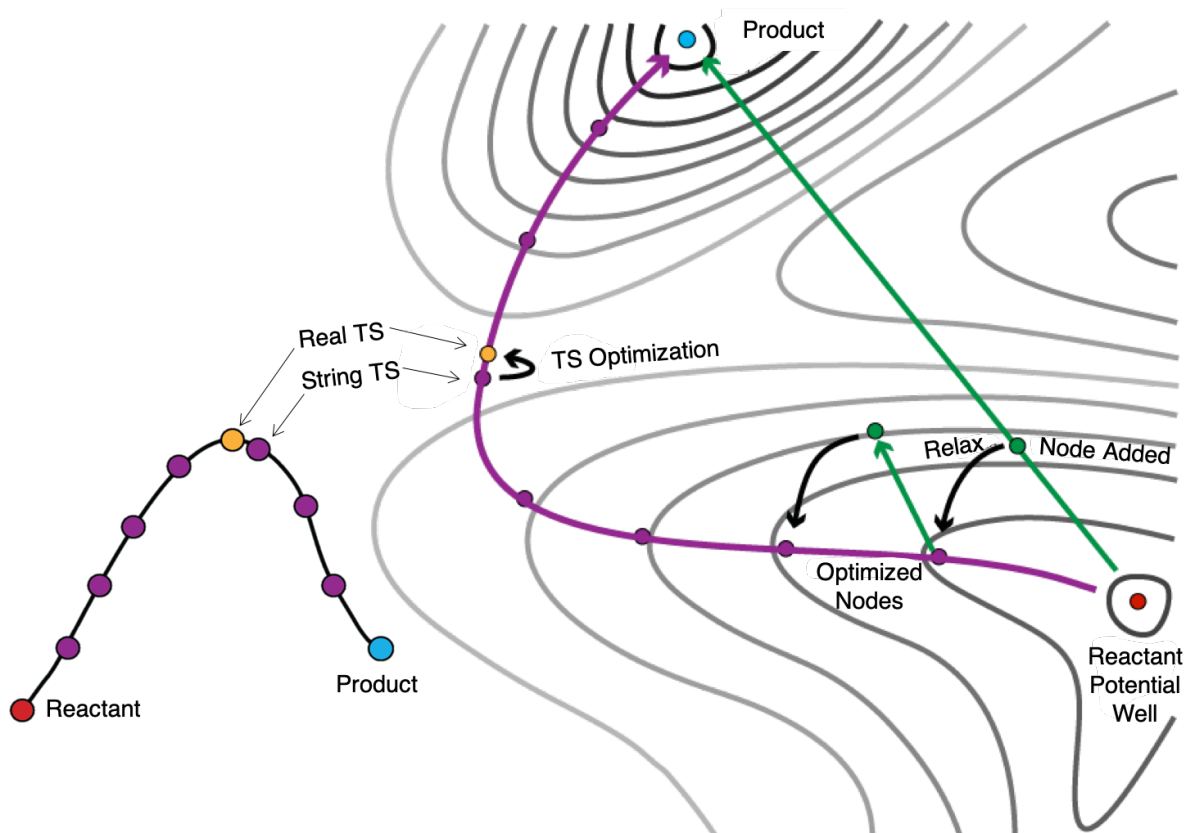
Figure 1-2. Single-ended GSM. The red node represents the user-provided reactant geometry sitting at a local minimum on the potential energy surface. The green nodes are the unoptimized nodes as they are added along the green vector which represents the provided driving coordinates. They are then optimized (purple nodes) and another node is again added in the direction of the

The Zimmerman Group continues to expand and adapt the application of GSM to challenging chemistries. Recently, functionalities have been developed for GSM so that photochemical,[56] surface,[57,58] or force-biased[59] reaction pathways can be explored.

Dissertation Outline and Chapter Overviews

Chapter 1 provided a brief overview of how computational tools are used to explore reaction pathways and inform chemical understanding. In Chapter 2, these tools are adapted to solve challenging chemical problems in mechanochemistry. Complex reaction mechanisms for three mechanochemical transformations are considered. First, examination of the spiropyran mechanophore which undergoes an electrocyclic ring-opening reveals a complex mechanism with two possible merocyanin product geometries. Second, a "flex-activated" reaction[60,61] is investigated to uncover the mechanical activation mechanism when the direction of the force is non-parallel to the breaking bonds. Finally, simulations explain and predict how polymer backbones transmit force to effect mechanophore activation.[62]

Chapter 3 is a complete mechanistic investigation of isomerization and propagation steps of a metal-free ring-opening metathesis polymerization (ROMP).[63] This polymerization shows promise as a good stereoselective system as it has been observed that the ratio of *trans* to *cis* product could be controlled by changing various parameters of the reaction such as reaction conditions (temperature, time, solvent), counter ion, and size of R-group. It is hypothesized that these parameters have the ability to control the *tran:cis* ratio through steric and electronic interactions. This study reports the mechanism of the redox-mediated metal-free ROMP and focuses on understanding how to regulate the *trans:cis* ratio of the polymer. Starting structures are

identified and used to determine transition states and product geometries using the single-ended GSM.[55]

Chapter 4 details the effects of substitutions on the activity and selectivity of a bimetallic chromium catalyst for the polymerization of propylene oxide. This investigation is an attempt to better understand how exchanging steric and electronic R groups in various positions on the catalyst could lead to the development of a better catalyst for isotactic polymerization. Five groups are considered at the ortho and para positions of the catalyst. At each position substitutions, that modulate either the electronics or the steric bulk are included. Transition states and products are obtained using the single-ended variant of GSM for the propagation step of each of the catalysts. Ultimately, this study describes how molecular geometry can control energetics and kinetics of the system including reaction rates and product selectivities.

Finally, Chapter 5 will include final remarks, a summary of the studies contained herein, and a discussion of the limitations of this work.

Chapter 2. Examining the Ways to Bend and Break Reaction Pathways Using Mechanochemistry

Introduction

The idea of mechanochemistry[64–69] emerged from the recognition that mechanical force can be utilized to induce chemical reactions. Mechanochemical reactions may also have unique selectivities and mechanisms compared to the more common means of activation (thermal, catalytic, or photochemical). The use of mechanical forces therefore can permit otherwise disallowed or unfavorable reactions,[70,71] resulting in products that differ from traditional expectations.[71–74] As a whole, mechanochemistry provides a host of unique reaction possibilities that have high potential for gaining full control over a diverse range of reactivity.

Ongoing developments in the field of mechanochemistry have led to new classes of reactions. The first class includes mechanofluorescence, mechanochromism, and molecular force sensing[64,75–77] that indicate a polymer is degrading under mechanical force. Next are reactions that can increase the lifespan of the polymer through strain-release motifs, which have led to the development of self-strengthening and self-healing materials.[78–81] Finally are reactions that release small molecules in the presence of a mechanical stimuli.[60,82–84] These reactions increase the functionality of polymers, and allow development of stronger, longer-lasting materials.

a) Spiropyran: Ring Opening Mechanochrome

b) Oxanorbornadiene: Flex-Activated Small Molecule Release

c) gem-dichlorocyclopropane: Mechanical Strain Release
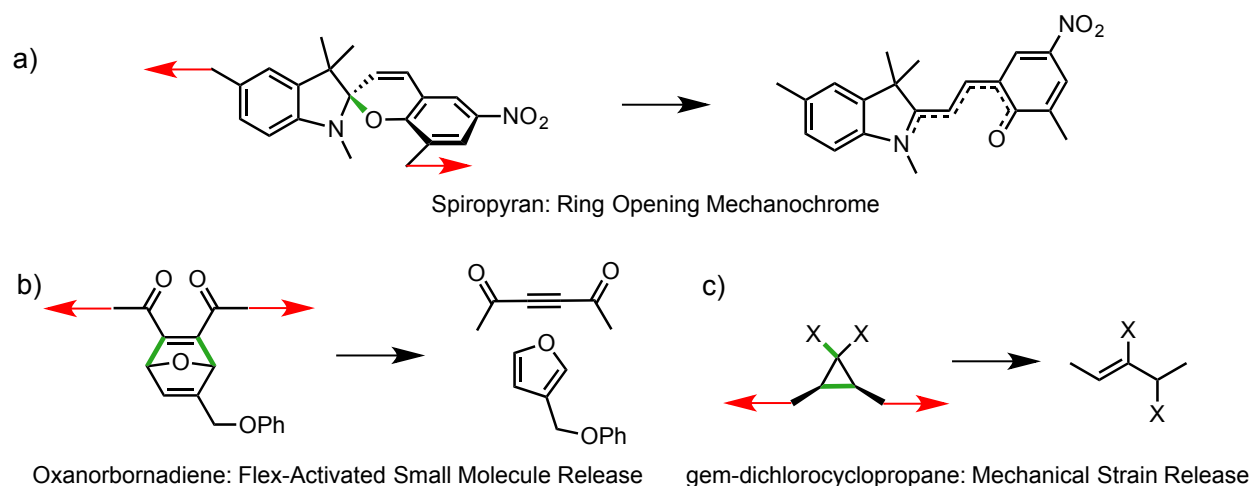
Figure 2-1. Modes of mechanical activation at common mechanophores.

Mechanophores, or mechanical-stress-responsive molecules, can be inserted into a polymer chain to respond to the application of strain. A few examples of mechanophores are shown in Figure 1, all of which are formally ring-opening reactions. For example, the spiropyran mechanophore (Figure 2-1a) is a good example of a molecular force sensor. Here, forces on the polymer selectively strain the relatively weak spiro C-O bond and induce electrocyclic ring-opening to its merocyanin form.[76,85,86] As the merocyanin product appears, the color of the mechanophore changes from yellow to red.[72,76] In the flex-activated reaction of Figure 2-1b, bond-breaking occurs only on nonintegral constituents of the polymer.[60,61] Instead of breaking a bond along the polymer backbone, bond angle distortions push the mechanophore toward an angle-differentiated product. This chemistry allows for the release of small molecules without directly harming the polymer chain.[84]

Though these reactions are functional, they all suffer from low mechanophore activation. Historical approaches to increasing activation have included attempts at modifying the points of attachment or the mechanophore itself.[76,87] On the other hand, it has recently been demonstrated that the polymer backbone also affects mechanophore activation.[62] A *gem*-dihalocyclopropane

ring-opening mechanophore (Figure 2-1c) has been used to show that the poly(norbornene) backbone gives a rate enhancement of 10^3 over the poly(butadiene) backbone.[62] It has thus been posited that the more rigid backbone has a "lever-arm effect"[62] that aids in activation of the mechanophore. Understanding these behaviors and developing new strategies for increasing mechanophore activation remain key questions for continued study.

| Loss of a Transition State | Transition State Shift | Loss of an Intermediate |
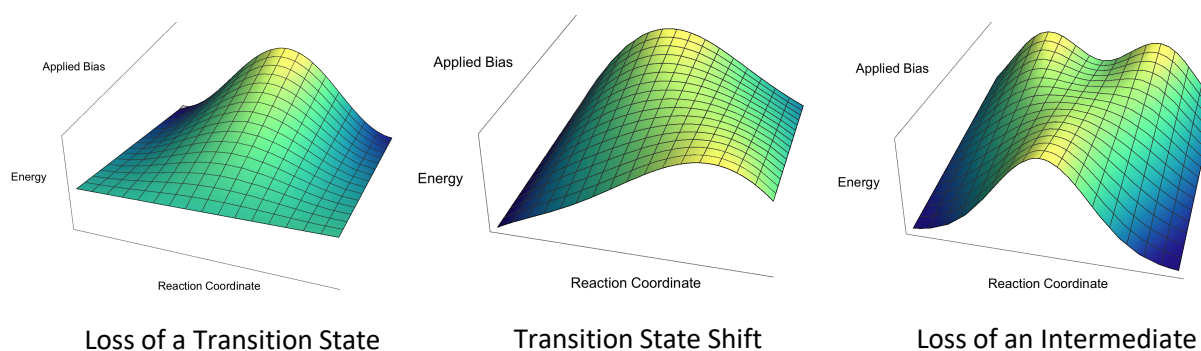
Figure 2-2. Examples of energy surface deformations that may occur in mechanochemical reactions.

The complexities and interest in force-induced reactions stem from underlying distortions of the potential energy surface (PES). At low forces, the reactions resemble their unbiased counterparts and TSs involve small geometric perturbations from the unbiased saddle points. At larger forces, however, the reaction landscape fundamentally changes,[8,28,29] resulting in at least three scenarios where large differences in reaction pathways emerge (Figure 2-2). First, a clearly defined TS on the unbiased surface could become an extended region of flat potential (Figure 2-2, left). Next, the TS may qualitatively change location, and could even merge with a stable intermediate (Figure 2-2, middle). In a third case (Figure 2-2, right), an intermediate could disappear from the landscape, resulting in a reaction profile with one TS instead of two. In these

cases, knowledge of the initial landscape does not provide a good representation of the force-biased landscape because the reaction pathways qualitatively change.

The present chapter reveals the complex reaction mechanisms for three mechanochemistries of contemporary interest in order to explore the possibilities of Figure 2-2. First, examination of the spiropyran mechanophore will show the disappearance of an intermediate on the reaction landscape with increasing force. Second, a "flex-activated" reaction[60,61] is investigated to uncover the mechanical activation mechanism when the direction of the force is not parallel to bonds that break. Finally, simulations will explain and predict how polymer backbones transmit force to effect mechanophore activation.[62] Together, these studies represent the first full reaction pathway optimizations for these challenging reactions, and provide deep understanding that can be used to design new mechanochemistries.

Computational Methods

Single-Ended Growing String Method

The single-ended Growing String Method (SE-GSM) is herein used to locate reaction paths and products without prior knowledge of the TS or product structure.[30–33] This is achieved by driving the reactants along a tangent vector toward a new stable intermediate, where the coordinates for this vector consist of bond addition or breaking directions. During the SE-GSM growth phase, the reactants are moved along the vector U_c,

$$U_c = \alpha \sum_{k=1}^{3N-6} \langle \delta q | U_k \rangle U_k \qquad (1)$$

where δq is a vector representing the primitive add/break coordinates, and U_k are the delocalized internal coordinates that span the internal motion of the molecular system. After moving forward away from the reactant, U_c also serves as a constraint to prevent structures from sliding back to the initial state. The unspecified coordinates are set to zero in δq such that they can relax without restriction during optimization. Since U_c is a single degree of freedom among 3N-6 coordinates, motion along U_c can be asynchronous.

After growing a string that passes over a transition state region, the nodes along the string are evenly redistributed and relaxed until an optimized reaction path is found. At this stage, the driving coordinates are discarded, and the string, therefore, is allowed to reach a minimum energy pathway without constraint. From this stage, an exact saddle point search occurs—which locates the TS within the reaction string—and the reaction path leading from the TS to the reactant and product is therefore found. Further details of GSM and SE-GSM methods are available in the Supporting Information and prior publications.[28-32]

GSM Application for Mechanochemistry

Because the underlying potential energy surface becomes distorted under applied mechanical bias, the single-ended string method will be appropriate for examining cases where the product geometry may not be intuitively known. Mechanical activation of a mechanophore effectively reduces the activation energy by coupling the mechanical work to the nuclear motion associated with the reaction. As a force is delivered to the mechanophore, the energy provided by the work can be quantified by

$$\Delta E = -F\Delta x \qquad (2)$$

where ΔE is the change in energy, F is the amount of force applied, and Δx is the change in distance over which the force is applied (Δx in the examples of this article will correspond to the distance between the two atoms where the tensile force is applied. Changes in this distance therefore correspond to interesting changes in the underlying PES). To operate GSM under an applied bias, the energies at each node are calculated by applying this energetic correction term, and the forces are also modified accordingly. Adding this bias potential to this single-ended string method produces a powerful means to explore and study mechanochemical reactions. The overall scheme for this method is shown in Figure 2-3.
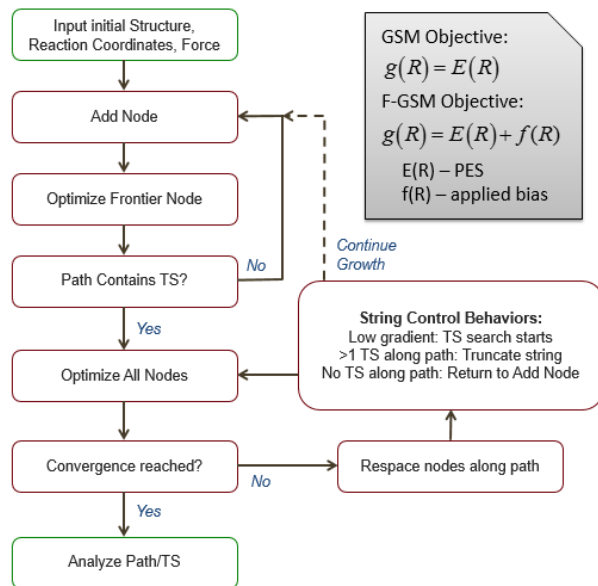
Figure 2-3. Algorithm for single-ended GSM when applied forces are included.

Computational Details

All quantum chemical computations utilized the B3LYP density functional[34–36] with the 6-31G* basis set,[37] though the GSM method is not limited to these choices. GSM is written in C++ and utilizes the electronic theory software package Q-Chem[38] for gradient information. All structure images were created in VMD.[39]

In GSM, the maximum step size was set as 0.8 Å-radian along the driving coordinate. The eigenvalue shift parameter λ of the eigenvector algorithm (see appendix)[32] is selected so all eigenvalues are positive, except from the exact TS search where λ shifts only the non-TS eigenvalues. Each new node is optimized during growth until the root mean square (RMS) gradient is less than 0.005 Hartree/Å, or 30 steps have occurred. Next, after the sum of perpendicular gradient magnitudes over all nodes, F, has been converged (F < 0.3), the climbing image search commences. Finally, the exact TS search begins after one of the following occurs: (1) the gradient is less than 0.2 Hartree/Å, the TS node converges to within 10 times the nodal convergence tolerance, and the constraint force is less than 0.01 Hartree/Å, (2) the gradient is less than 0.1 Hartree/Å, the TS node converges to within 10 times the nodal convergence tolerance, and the constraint force is less than 0.02 Hartree/Å, or (3) the TS node is within five times the nodal convergence tolerance. The nodal convergence tolerance was set to 0.0005 Hartree/Å. Once the TS node has reached a small RMS gradient (<0.0005 Hartree/Å) the RP is considered converged.

In all of the test cases, tensile force is applied at terminal carbons of the polymer backbone, or the carbons at the attachment points on the mechanophores (the method is not limited to the study of canceling tensile forces, but these are most pertinent). The force is applied along the vector that connects the two atoms at which the force is applied. Before GSM commences, the initial structure is optimized under the force that will also be applied during string optimization. While GSM is not restricted to this type of force, and can handle arbitrary force definitions, the tensile force should closely resemble AFM experiments that have been applied to the chemical systems under examination below.

For this initial structure optimization, geometries were allowed to relax from an extended polymer that was optimized under relatively high forces. This is because a relaxed polymer chain

in the ground state could have numerous low energy conformers existing in equilibrium with one another. When a small initial force is applied to a polymer, the polymer chain is straightened. At first, small forces make the polymer taut, and only after this is accomplished does the applied force begin to influence mechanophore reactivity. Therefore, in order to obtain data that is not reliant on arbitrary starting geometry configurations, calculations must use geometries relaxed from extended polymers.

Results and Discussion

All of the reactions presented herein were chosen due to their complexity and the combined breadth of difficult mechanochemical transformations they comprise. The first example, a spiropyran mechanochrome, was chosen due to its size and multiple possible ring-opening products, to demonstrate GSM can handle large systems.[72,76,82,85,86] The second, a flex-activated system, is discussed as an example of an unusual mode of activation where pulling along the polymer backbone is substantially orthogonal to the reaction direction.[60,61] The third mechanochemical reaction examines differing degrees of force transfer to the mechanophore via two polymer backbones, in the "lever-effect" polymers of recent interest.[62]

Spiropyran ring-opening mechanochrome
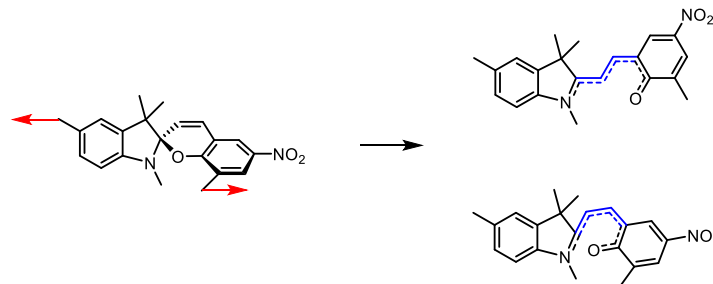
Figure 2-4. From the force-induced spiropyran reaction, two different merocyanin products were identified. The cis and trans isomers are shown on the right with the pertinent bonds highlighted in blue.

The spiropyran mechanochrome was designed to selectively stress the spiro C-O bond until it ruptures, as discussed in detail by Sottos.[76] The model for the spiropyran mechanophore in this study is shown in Figure 2-4. The model was stretched by optimization at 4 nN of force, then stepped down to 0 nN in sequences of 0.5 nN to obtain optimized geometries for the reactants. Once the optimized structures were obtained, these were used as starting points for reaction path finding with GSM. The driving coordinates (i.e. Equation 1) for ring opening were selected to break the spiro C-O bond.

Interestingly, two different merocyanin products, the *cis* and *trans* isomers of Figure 2-4, were identified. At forces less than 2nN, the *cis* product was found, but at higher (> 2nN) forces, the ring-opened structure isomerizes to the *trans* product without an energy barrier. Double-ended strings were then run from the initial geometry to both the *cis* and *trans* products as well from the *cis* intermediate to its *trans* product, as appropriate.

Ring Opening Coordinate vs cis-trans Isomerization Coordinate

Ring Opening Coordinate vs cis-trans Isomerization Coordinate
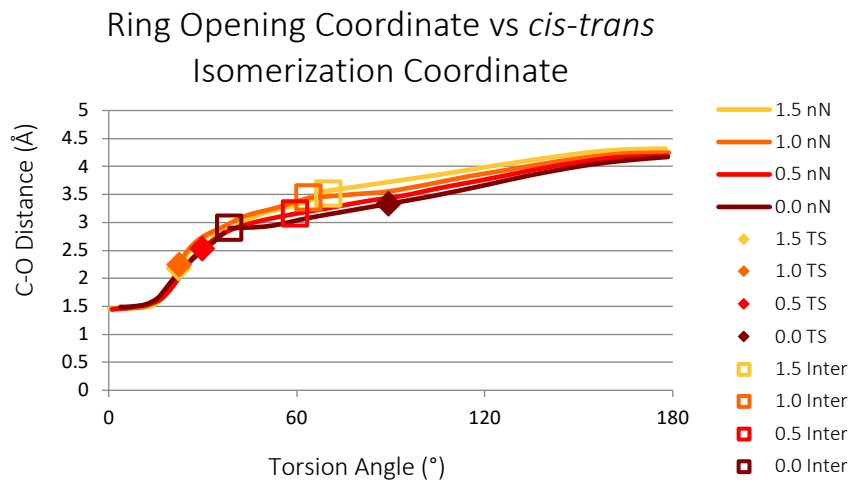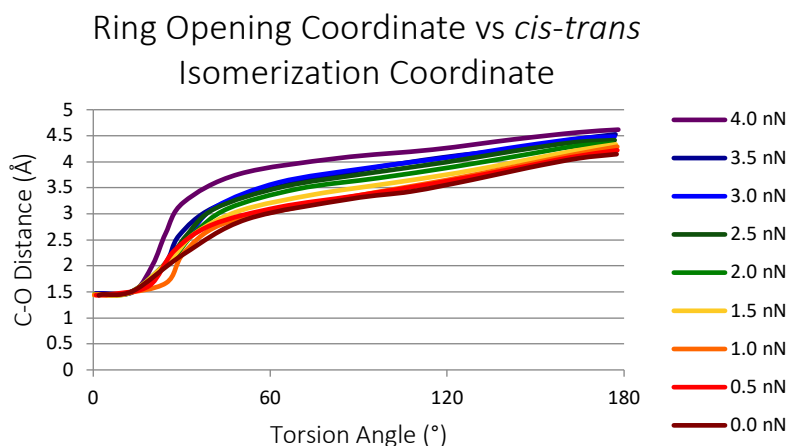
Figure 2-5. The breaking spiro C-O bond length plotted vs the torsion angle of the four carbon atoms between the heterocycles in Figure 4 at various forces. In the first graph, all reactions go to the trans configuration (torsion angle = 180°). In the second graph, the reactions with stable cis intermediates are plotted with these intermediates marked. These curves are comprised of the reactions to the cis product plus the cis-trans isomerization from that intermediate.

Figure 2-5 shows the progress of reaction for the mechanophore activation, comparing the ring-opening coordinate, as measured by spiro C-O bond distance, to the *cis-trans* isomerization coordinate measured by the corresponding torsion angle. In Figure 2-5, top, all reactions reach the *trans* product in a single elementary step. Figure 2-5, bottom, shows reaction paths that lead to a stable *cis* intermediate, as well as paths from this intermediate to the *trans* product. In the ground

state, the TS occurs after the ring-opening, during the *cis-trans* isomerization step. Higher forces result in only the *trans* product since the greater force leads to greater degree of elongation that only the *trans* product can provide.
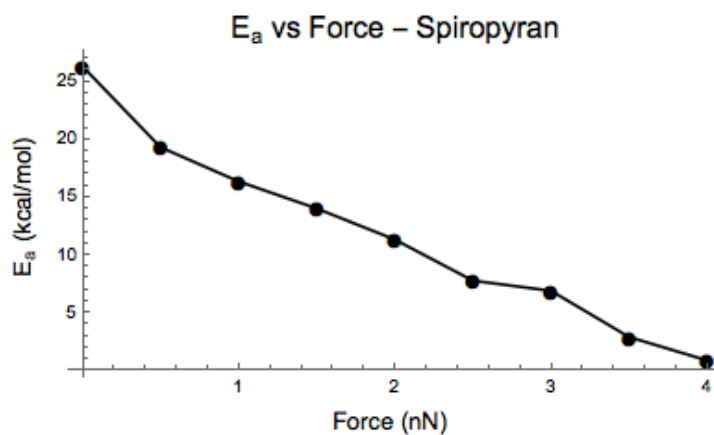
Figure 2-6. Activation energy vs. force for spiropyran ring opening. See Figure 2-4 for reaction description.

As expected for a reaction where the product is significantly stretched compared to the reactant, the activation barriers for ring-opening decrease as increasing force is applied (Figure 2-6). Because the transition states leading to the *cis* product and *trans* products are so similar, a roughly linear graph is produced, with a slope of -5.9 kcal/(mol*nN). This can be understood by noting that the *cis-trans* isomerization occurs after the rate-limiting, ring-opening TS.

Consistent with the observed decrease in activation barrier, the mechanophore eventually breaks open without barrier at high forces. The amount of force required for this direct cleavage of the spiro C-O bond is between 10.9 nN and 11.0 nN. Though it may be expected that the direct cleavage would occur at ~4.5 nN, the optimization does not break the bond with this amount of force because the nuclear motion associated with the bond breaking is not exactly parallel to the direction of the force. Specifically, the torsional motion begins at the spiro attachment prior to the

bond breaking and is nonparallel to the force. This example suggests that realistic reaction paths will almost always occur along directions that are not fully in-line with applied forces, but that force plus thermal activation is responsible for the mechanophore activity.

Flex-activated small molecule release

The bonds being broken in a flex-activated reaction are not directly elongated by the application of the force, but rather are "flexed" through angular distortions. This strategy is useful for promoting release of a small molecule that is embedded in the polymer, but not integral to its structural integrity. As opposed to typical mechanophores where a bond breaks in a parallel alignment to the applied force, the reaction coordinates involved in flex reactions are mostly perpendicular to the direction of the force. The flex-activated oxanorbornadiene reaction introduced by Boydston[60,61] is one such example where the breaking bonds are not obviously parallel to the applied force (Figure 2-7).
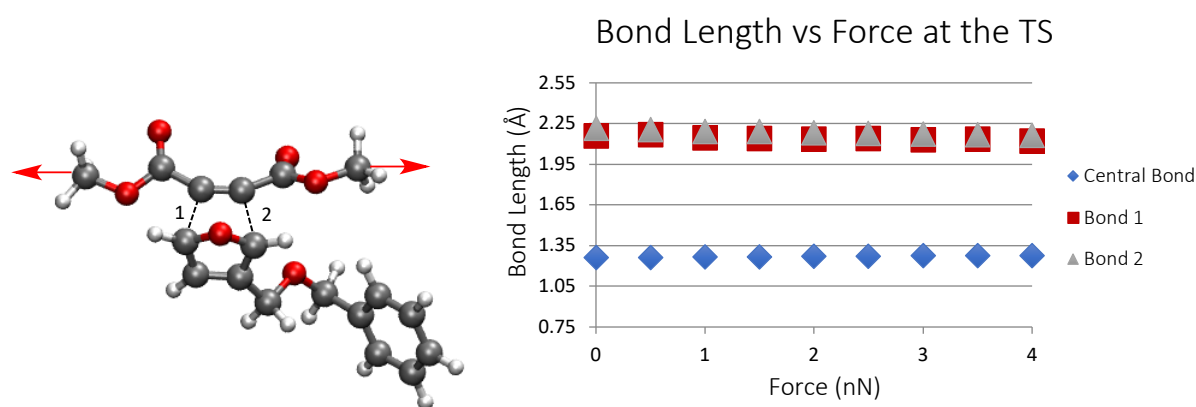
Figure 2-7. Ring-opening flex reaction (left) showing applied force direction with red arrows. Bond lengths of the labeled bonds stay relatively constant across the varying applied forces, indicating that the transition state geometry is largely unaffected by the strain.

Unlike in the spiropyran reaction, the key bond lengths at the TSs are roughly equal over the differing forces, being only marginally changed by varying forces. Figure 2-7 (right-hand side) shows that the bond lengths of key coordinates at the TS remain more or less constant under all the applied forces. For example, the central C-C bond is 1.26 Å at zero applied force, and 1.28 Å at 4 nN, while the C-C bonds of the ring opening reaction change from 2.16 and 2.21 to 2.12 and 2.16 Å from zero to 4 nN. Even with forces biasing the potential energy landscape, essentially the same TS geometry emerges at all realistic values of applied force.
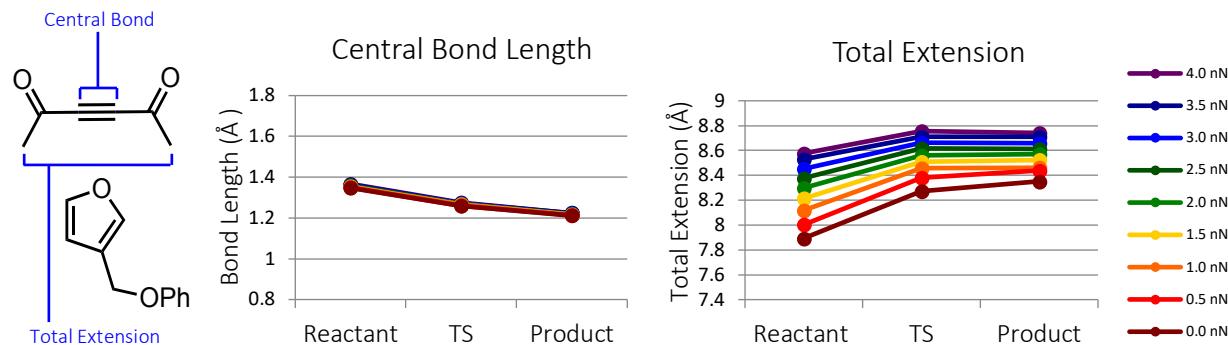
Figure 2-8. The central bond shortens as the reaction proceeds while the total extension of the mechanophore increases to provide local strain relief.

The flex-activated reaction is even more interesting when one notes that the central C-C bond contracts from a double bond to a triple bond during the course of the reaction. Extensive forces therefore are not biasing the C-C distance towards the product, but instead are allowing the total extension of the mechanophore to increase, as shown in Figure 2-8. The activation of the flex system therefore can be understood as biasing the structure to longer chain extension, which can occur due to linearizing the central carbon chain of the mechanophore. Incidentally with this extension, at a linear structure the triple bond is preferred, permitting the retrocycloaddition to proceed and release the furan.
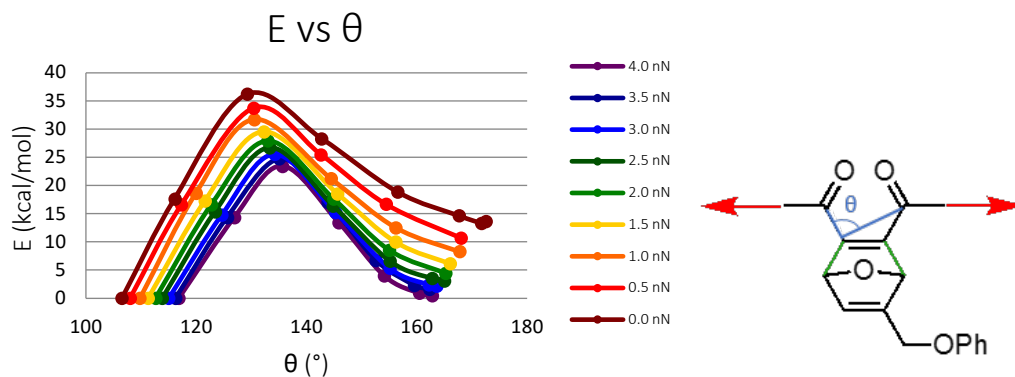
Figure 2-9. Plot of the energy vs θ. Note that there is not a single theta value that corresponds with the transition state at each of the forces.

While GSM provides a simple, yet detailed description of flex activation, this description differs from prior simulations which employed specific constraint coordinates to represent the force. In those studies, a constraint coordinate, θ,[60] was used to bias the reaction towards the product, as indicated in Figure 2-9. By imposing a geometric constraint on the angle and then systematically increasing the θ value, the desired bonds eventually break. The θ value does not provide a fully useful representation of the reaction, however, as it is just one piece of the total reaction puzzle. Figure 2-9 shows that the correct TS at each of the forces has a unique θ value, indicating that no single θ can appropriately represent the reaction. Mechanochemical reactions can therefore be considered to be multiparameter pathways, where many atomic coordinates change in concert. The true reaction path is activated not just by force that "bends" one coordinate, but thermal energy allows other degrees of freedom to move toward the TS on the force-biased PES.

The sequence of activation energies as a function of applied force is given in Figure 2-10. Just like the spiropyran reaction, a mostly linear decrease in barrier occurs with increasing force.

Here, the activation energy is just over 10 kcal/mol lower in the reaction where 4 nN of force is applied relative to the ground state reaction.
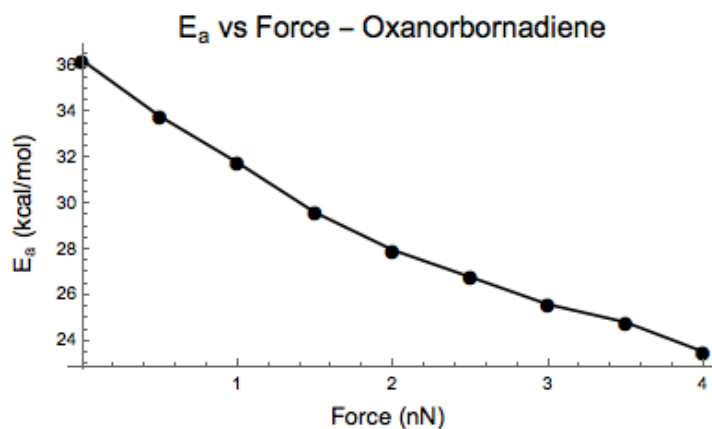
Figure 2-10. The activation energy of the oxanorbornadiene reaction.

Lever-arm effect mechanochemistry
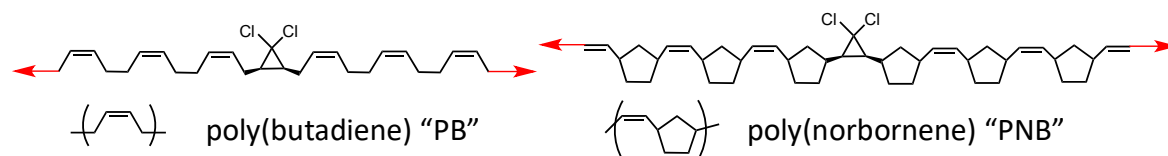
Figure 2-11. The gem-dichlorocyclopropane mechanophore at the center of poly(butadiene) and poly(norbornene) chains. Force is applied in the direction of the red arrows.

Lastly, we aimed to aid the understanding of the so-called "lever-arm" effect as presented by Craig and coworkers.[62,97] Two backbones, poly(butadiene) (PB) and poly(norbornene) (PNB) were studied to observe the effect that the polymer backbone can have on mechanophore activation. Experiments have reported that PNB provides a mechanical advantage by acting as a lever that accelerates rates of reaction relative to PB by three orders of magnitude.[62]

In agreement with previous studies,[41] systematic GSM studies determined that the chemistry in these systems is largely local (see Supporting Information) and not a strong function

of the length of polymer backbone. This is fortunate from a computational standpoint as the ability to truncate without the loss of chemical accuracy saves computational time and resources. Our chosen models for the gem-dichlorocyclopropane mechanophores are shown in Figure 2-11.
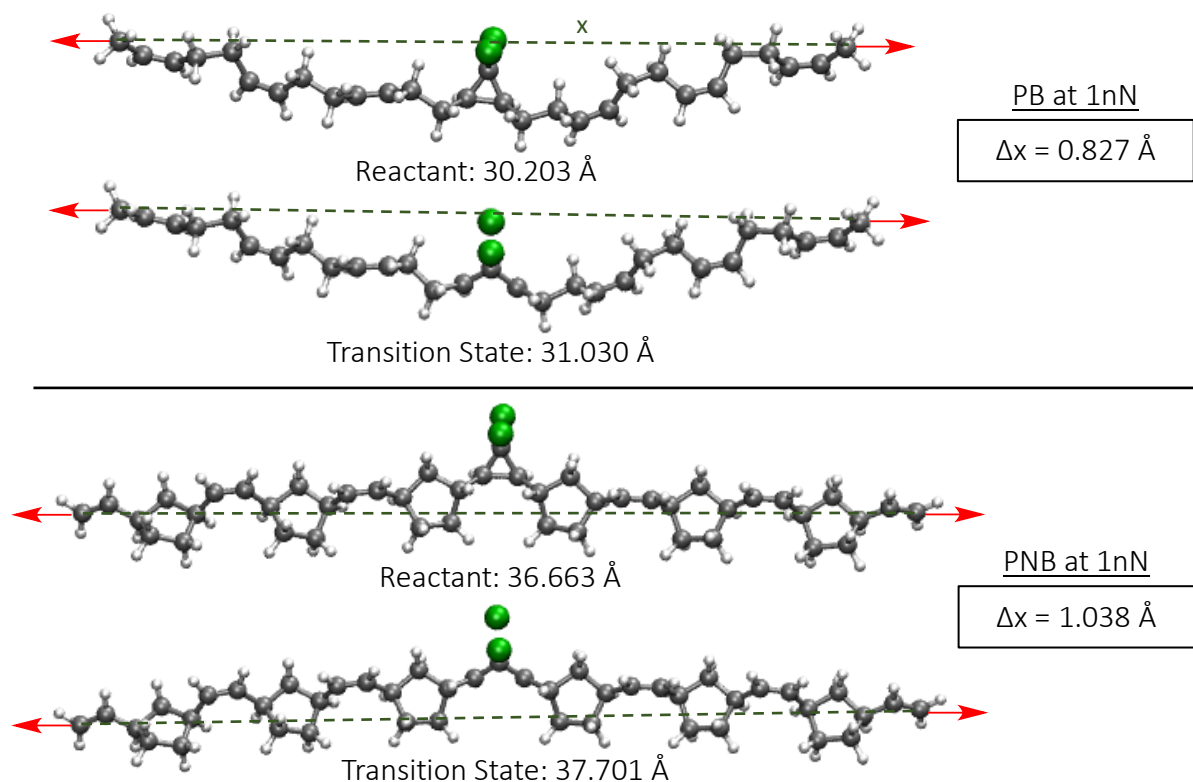
Figure 2-12. Measuring the Δx of the gem-dihalocyclopropane mechanophore inserted into either the PB or PNB backbone. The Δx was generally observed to be larger in the PNB chain, leading to a greater change in activation energy for the PNB backbone since ΔEa = -FΔx.

The function of mechanical advantage was studied by considering the total change in polymer extension from the reactant to the TS, Δx, under a range of applied forces (Equation 2). Figure 2-12 shows the reactant and TS structures in the PNB and PB backbones at 1 nN of force as well as Δx. Since PNB provides the larger Δx, it follows that PNB would also provide a greater change in energy relative to PB. Thus, the same amount of force applied to each backbone leads to greater relative extension of the polymer in PNB.
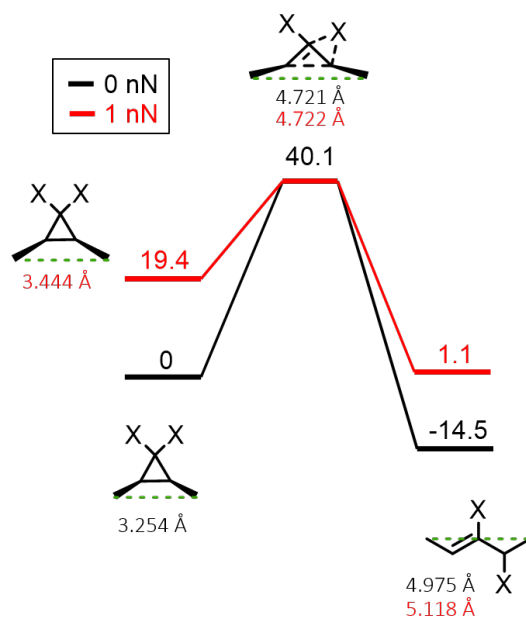
Figure 2-13. Mechanochemical activation effectively reduces the Ea by raising the reactant's energy. In this case, the reaction still goes through the same transition state.

Activation of the gDCC mechanophore couples the applied mechanical force largely in the direction of the reaction. While it might be imagined that this brings the energy of the TS down, the TS geometry at applied force is highly similar to that at zero force. Therefore the E_a is reduced by raising the initial energy of the reactants—which are highly stretched compared to the zero-force structure—as suggested by Figure 13.
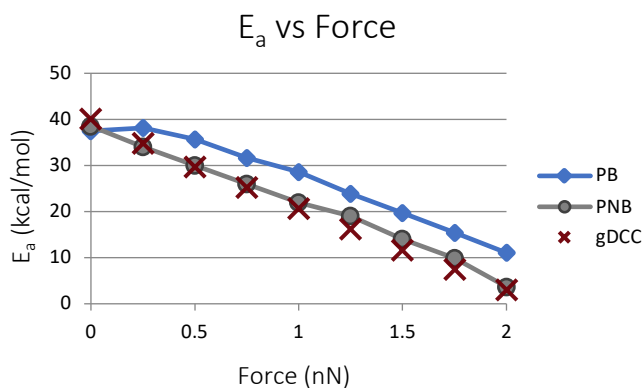
Figure 2-14. Activation energy vs force plot for PB and PNB each with three monomer units on either side of the mechanophore, and the mechanophore alone.

The results also suggest that although PNB does provide a mechanical advantage relative to PB, PNB is not acting as a lever in the sense of force amplification. When the activation energies of the gDCC mechanophore in PB and PNB models are plotted alongside the data for the mechanophore alone (Figure 14), it is clear that the isolated mechanophore activation barriers are nearly identical to the results for the PNB chain. This indicates that the full force is being transmitted to the mechanophore in the PNB chain. In the PB chain, however, some of the force is being lost in other degrees of freedom due to the backbone being less rigid. Overall, PNB does not enhance the force applied to the mechanophore so much as deliver it successfully. In passing, we note that an alternative lever-arm system[40] may exhibit different behavior, as preliminary data (unpublished results) indicate a different trend than seen in Figure 14. Further investigation will determine where and if a true "lever-effect" is present in those systems.

Conclusion

Mechanochemistry is an important, emerging branch of chemistry that encompasses a wide range of chemical transformations. Because mechanically enhanced reactions can permit otherwise disallowed or unfavorable reactions, it is vital that the underlying modes of these new reactivities be uncovered. This will allow identification of transition states and products for reactions that do not easily fit into the scope of well-established chemical intuition. For instance, reactions that don't follow ground state rules or have unknown products can be examined, such as those from several examples in the literature.[7,8,42,43] The ability to elucidate the details of these complex reactions was demonstrated, in finding the *cis* and *trans* isomers of the spiropyran to merocyanin transformation at different magnitudes of force, the fundamental means of flex mechanophore activation, and

showing the physical principles of force transmittance through different polymer backbones. First principles simulation's capacity for discovering reaction mechanisms under force will continue to prove useful for developing improved mechanochemical reactions, mechanophores, and ultimately, advanced functional materials.

Acknowledgements

Chapter 3. A Mechanistic Look at the Tunable Microstructure of Poly (Norbornene) via Stereocontrolled Metal-Free Ring-Opening Metathesis Polymerization

This chapter is based on a highly collaborative project with the research group of A.J. Boydston. Boydston Group Contributors: Xuejin Yang, Postdoctoral Associate, and Sean Gitter, Ph.D. Student.

Introduction

Poly (norbornene) (PNB) has high thermal stability (up to 400ºC), a high glass transition temperature (T_g above 300 ºC), and low moisture absorption making it a suitable polymer for vehicle fittings such as bumpers, arm rests, and engine mounts.[101] Additionally, due to its excellent optical transparency, low water uptake and low dielectric constant, PNB is also an ideal candidate for applications in optical devices or as thin films or protective coatings in opto-electronic materials.[102] Many of these desirable properties stem from the fact that in PNB, two adjacent carbon atoms are fixed in their conformation which makes rotation between two neighboring monomer units about the polymer chain axis strongly restricted.[101]
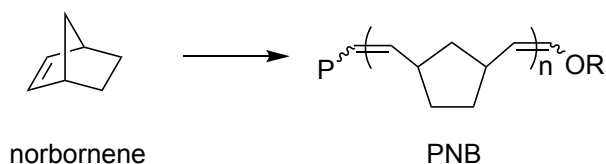
norbornene   PNB

Scheme 3-1. Polymerization of norbornene to poly (norbornene) via ROMP

Norbornene can be polymerized to high molecular weight either through the double bond while retaining both rings[103] or through ring-opening metathesis polymerization (ROMP), opening one ring.[104] This chapter is concerned with ROMP poly(norbornene). ROMP has been widely used for norbornene polymerization due to its ability to achieve living polymerizations, a superior

method for generating diblock and triblock co-polymers, and its ability to produce polymers with narrow dispersities.[105–109] The generalized mechanism for ROMP can be found in Scheme 3-2. A metal carbene initiator and a cycloolefin undergo metathesis to form a metallocyclobutane. The strained monomer then opens to form a metal carbene and the process can repeat with a new monomer. Because ROMP capitalizes on ring-strain as the driving force to open a cyclic olefin, the second step in Scheme 3-2 is essentially irreversible.
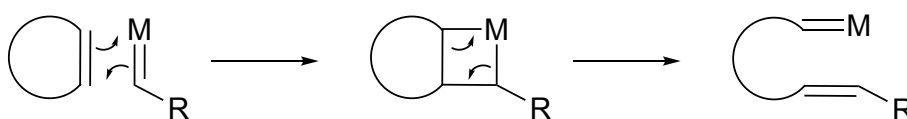
Scheme 3-2. Generalized mechanism for ring-opening metathesis polymerization.

ROMP of norbornenes can lead to a variety of microstructures depending on the resulting tacticity of the polymer (*isotactic, syndiotactic*) and double-bond configuration (*trans, cis*).[105,110,111] In PNB, the cyclopentylene rings necessarily have a cis configuration retained from the monomer, but the connecting vinylene moiety possesses *cis/trans* isomerism.[112] Further complexity comes from the fact that polymers may have all *trans* or *cis* C=C bonds but that have an *isotactic* or *syndiotactic* relationship between neighboring monomer units in the polymer.[113,114] Figure 3-1 shows the four possible configurations.

cis, isotactic   *trans, isotactic*

cis, syndiotactic   *trans, syndiotactic*
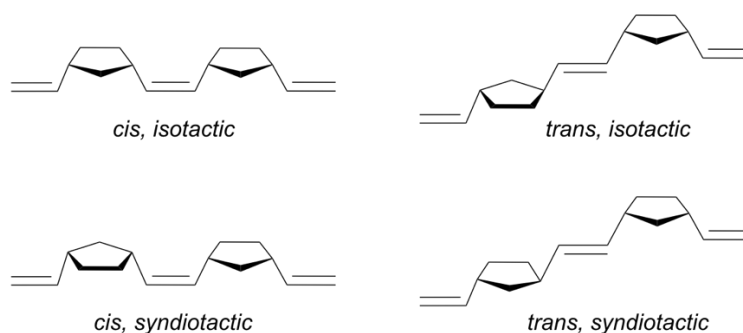
Figure 3-1. Possible microstructures for poly(norbornene).

Polymers with high percentage of a single microstructure have more well-defined and desirable properties than their atactic or non-stereospecific counterparts.[111,115,116] Stereocontrolled ROMP, however, has been difficult to achieve and still poses challenges in polymer chemistry. Only limited control of *trans/cis* content has been achieved with discrete Ru alkylidenes and the stereocontrol is typically dependent on specialized monomers.[117,118] It is believed that the lack of stereoselectivity in these systems is due in part to the Ru alkylidenes' ability to rotate easily and therefore inability to enforce the necessary steric constraints.[106,110,118,119] Recently, olefin metathesis catalysts of tungsten, molybdenum, and ruthenium were found to initiate ROMP of norbornene monomers with high stereocontrol of tacticity and *trans/cis* ratio.[111,117,118] The ability to tune the ROMP polymer microstructure comes in part from a series of catalysts with polydentate ligands which reduce the number of rotatable bonds on the metal center thereby locking the catalyst into a configuration which selectively produces one microstructure over another.

Though these more traditional metal-based catalysts have begun to be optimized for ROMP processes, undesirable metal-based byproducts are difficult to remove from the polymer after polymerization.[120] Additionally, these metal-based byproducts can complicate biological studies and electronic properties measurements. In order to remove the byproducts, complicated removal procedures[120] would have to be implemented, adding processing steps and therefore additional costs for manufacturing facilities.

The first metal-free ROMP was reported by the Boydston Group[63] in 2015 in a photo-mediated process. It was proposed that a metal-free process could potentially better control end-group functionality and provide a new mechanism for complicated polymerizations. This metal-free ROMP also shows promise as a good stereoselective system as it has been observed that the ratio of *trans* to *cis* product could be controlled by changing various parameters of the reaction

such as reaction conditions (temperature, time, solvent), counter ion, and size of R-group on the initiator. It is hypothesized that these parameters have the ability to control the *trans/cis* ratio through steric and electronic interactions.

The project described within this chapter seeks to provide a better grasp of the mechanics of the stereocontrolling steps of metal-free ROMP and in turn, use this insight to understand and control the selectivity. In order to do so, quantum chemical computations were employed to probe relevant intermediates and transition state structures involved in the reaction equilibrium. Next, the energies of the *trans* products were evaluated in comparison to the *cis* products when assorted factors such as counter anion and end group were varied. The ultimate goal of this work is to understand how these factors influence stereoselectivity, both individually and together, in order to develop a ROMP system that can produce polymers with high tunability of stereocontrol.

Computational Details

All quantum chemical calculations were carried out using the Q-Chem 5.0 software package[95] at the B3LYP level of theory[93] using a spin unrestricted formalism and the 6-31G* basis functionals[121] for optimization and frequency calculations. The structures without counterions were modeled as cationic doublets. Double-Ended Growing String Method (GSM) was used to identify transition states and minimum-energy reaction paths from optimized reactant and product structures.[50,51] SMD solvation corrections[122] were performed for all transition states and stable intermediates at B3LYP/6-31G*[93] using the ORCA quantum chemistry package[123] with toluene. Reported energies are Gibbs free energies with enthalpy and entropy corrections in the solvent phase. All geometries were confirmed to have the appropriate number of imaginary frequencies.

Discussion

We start by analyzing the mechanism of the photo-mediated, metal-free ROMP. The reported mechanism, as depicted in Scheme 3-3, is initiated by a single-electron oxidation of the vinyl ether initiator (**A**) to generate a radical cation (**B**). The radical cation can then react with cycloalkene monomer to form a [2+2] complex (**C**). The initiation phase concludes with the complex undergoing ring-opening in order to alleviate ring strain (**D**). Propagation with additional monomers yields ROMP polymers with a reactive radical cation chain end (**E**), but would eventually undergo reduction to arrive at **F**.
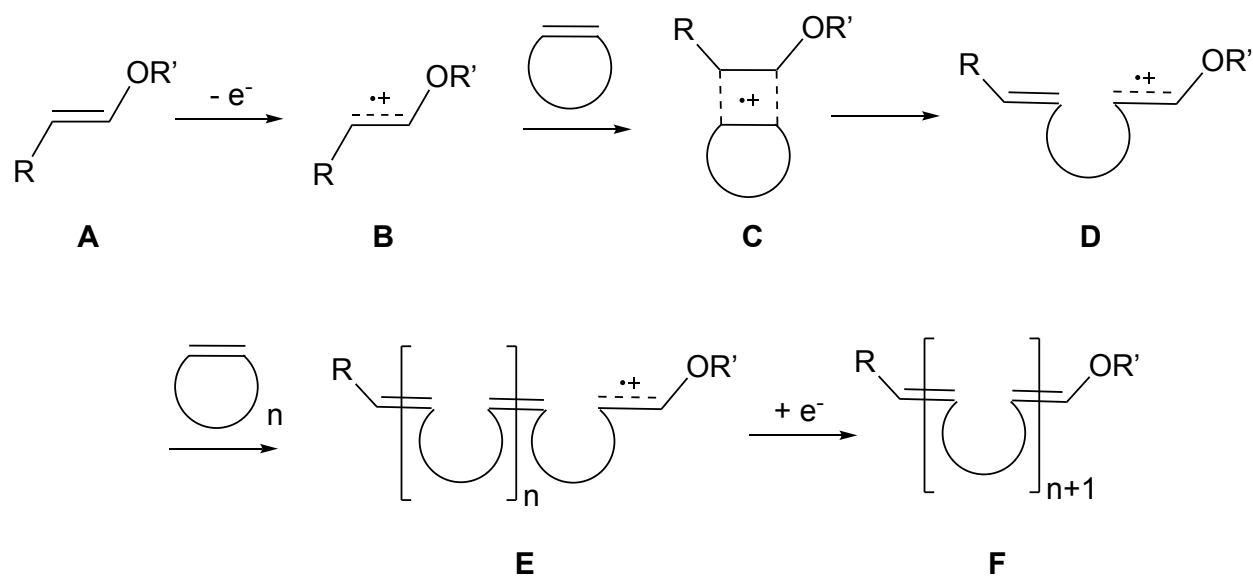
Scheme 3-3. Generalized mechanism of redox-initiated, metal-free ROMP

During this process, isomerizations that determine whether the final product structure will be *cis* or *trans* can take place. Scheme 3-4 shows important intermediates (**1-3**) during the ROMP processes that can occur as one of four isomers (**A-D**).

34
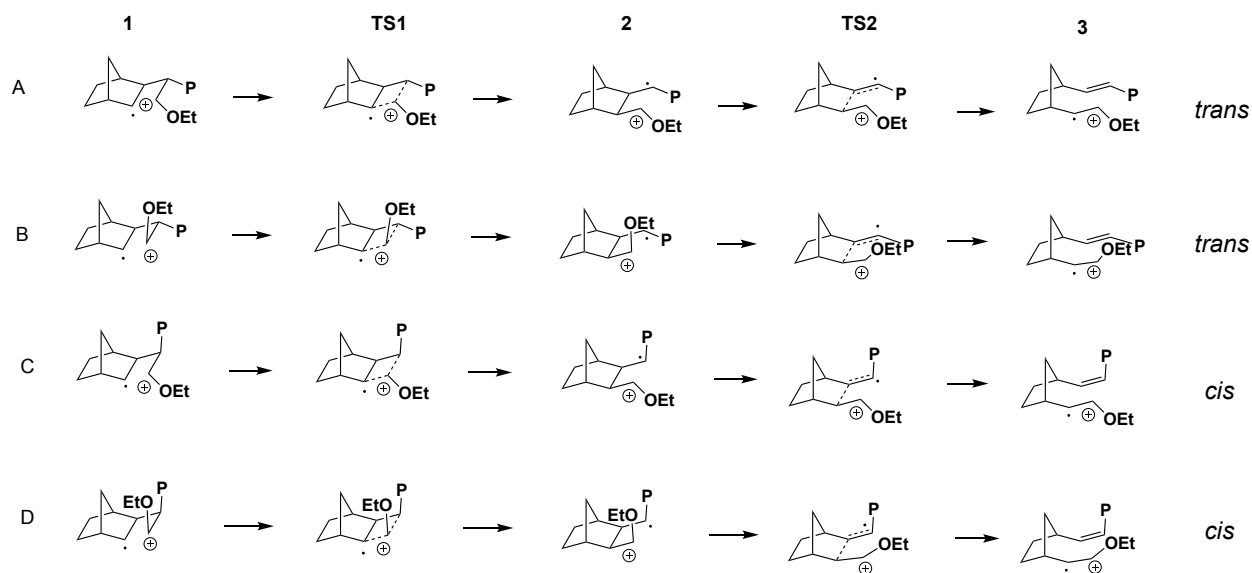
Scheme 3-4. Mechanism for propagation from four unique isomers of the monomer. For computations, the polymer (indicated here by "P") has been replaced by iPr to simplify calculations.

As demonstrated in Figure 3-2, at intermediate **2**, both of the bonds off of the norbornene can rotate allowing the transition from endo to exo and to other species **2** intermediates. For example, intermediate **2A**, in which both substituents are exo, can undergo rotations of either arm to the endo position to result in species **2B** or **2C**. Alternatively, both of the arms could rotate to the endo position in concert to isomerize to **2D**. Once the reaction proceeds from intermediate **2** to intermediate **3**, however, the geometry is locked in and the bonds can no longer rotate freely to move from one isomer to the next.
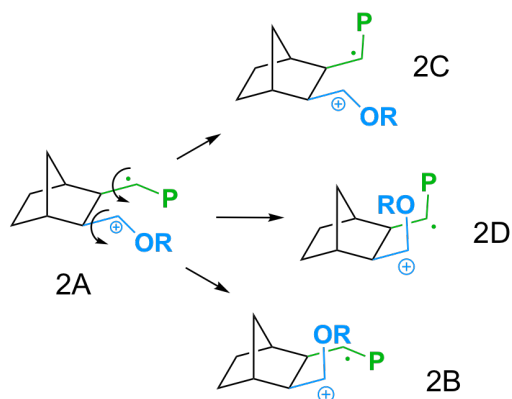
Figure 3-2. Possible isomerization routes from species 2A. The blue or green rotations may occur alone to result in species 2B or 2C, respectively, or both the blue and green rotations could happen in concert to isomerize to 2D.

As shown in Figure 3-3, the energy of activation for the isomerization from one isomer of species **3** to another is insurmountable at room temperature. In the representative example, the isomerization from **3A** to **3B** has an activation energy of 32.3 kcal/mol while the isomerization of the analogous structures from species **2** carries an activation energy of 8.6 kcal/mol. The high energy barriers for rotation of species **3** are due to steric clashes of the chain end and growing polymer at the transition state, as demonstrated in Figure 3-3, as well as electronic effects of the radical cation bond. The species **3** isomerizations are more difficult electronically because the radical cation bond introduces an electron into its C-C 2p orbital making bond rotation more

challenging. The isomerization from **2A** to **2B** has an activation energy well within the accepted limit for room temperature transformations.
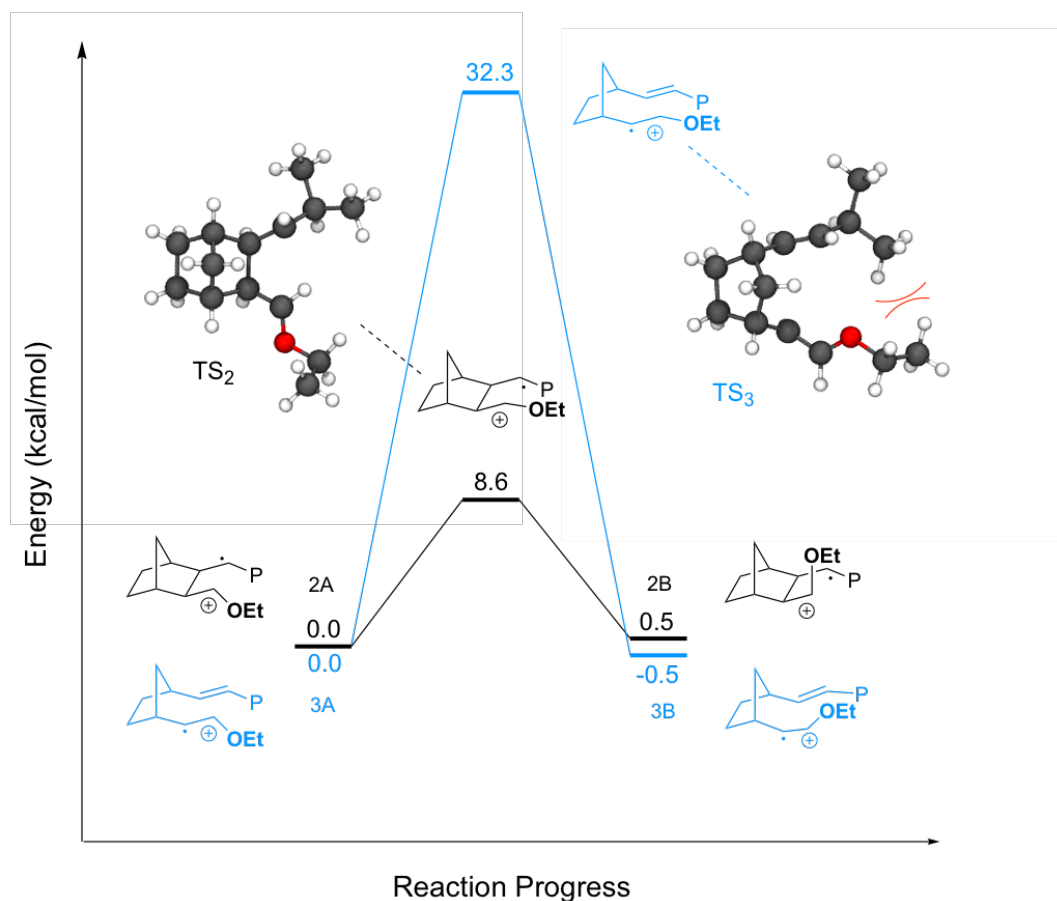
Figure 3-3. Isomerization from 2A to 2B shown in black while the isomerization from 3A to 3B is shown in green. The transition state structure for the species 3 isomerization (TS₃) shows steric hinderance compared to the species 2 isomerization transition structure (TS₂). All energies reported in kcal/mol.

These low barriers for the isomerization of species **2** allow all four isomers to exist in equilibrium. As the isomers proceed to species **3**, the isomers get fixed into either a *trans* product (3A, 3B) or a *cis* product (3C, 3D). As shown in Figure 3-4, the various reaction barriers for isomerization and ring-opening are all relatively low, allowing all of the species **2** and species **3** isomers to exist in thermodynamic equilibrium. The *trans* products are thermodynamically

preferred and experimentally, under room temperature conditions in toluene, the *trans* product is produced in a ratio of 1.18:1.
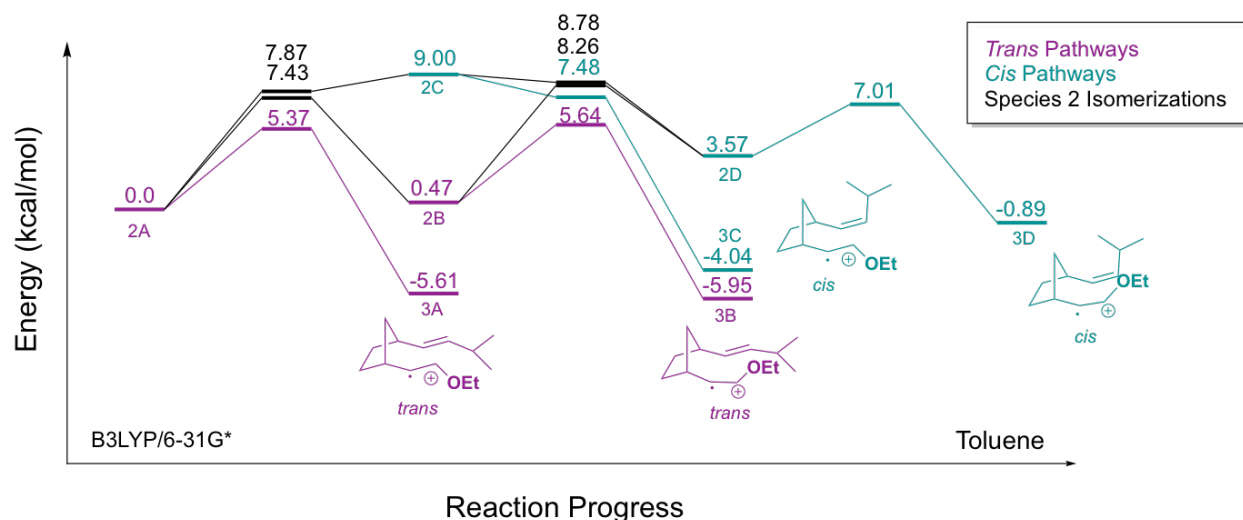
Figure 3-4. Potential energy surface for isomerization between species 2 isomers and the forward reaction to each of the four species 3 isomers. Trans pathways are shown in purple, cis pathways are shown in teal, and isomerizations from one isomer of species 2 to another are shown in black.

Under the vast majority of experimental reaction conditions, the *trans* product is preferred to varying degrees. Thus, the quantum chemical calculations are able to capture much of the experimental preference before other contributing factors are considered. There are specific reaction conditions, however, such as those in outlined in Table 3-1, under which the product ratio can shift toward the *cis* product. When ROMP is carried out in a nonpolar solvent with a large counter anion at low temperatures product ratios can lean toward *cis* as much as 1:1.70, *trans:cis*. It was therefore determined that in order to try to capture the full story, it would be important to consider and model some of the effects that these other conditions could have on the system.

Table 3-1. Temperature influence on stereoselectivity. Experimental data from the Boydston Group at University of Wisconsin, Madison.

Condition: NB : EPE : pyrylium = 100 : 1 : 0.05
Concentration: 2M
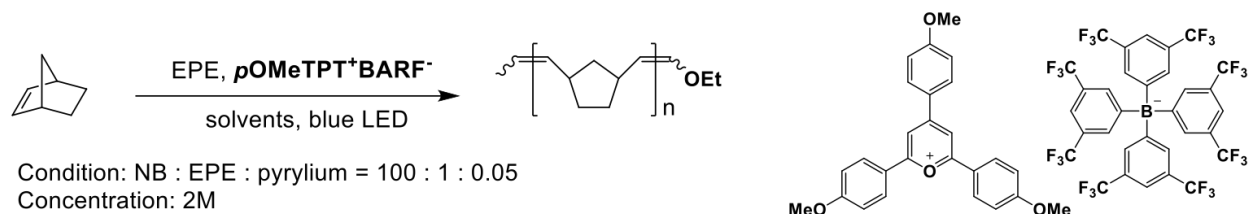
solvent	Temp (°C)	time	conversion (%)	$M_{n,exp}$ [kDa]	$M_{w,exp}$ [kDa]	Đ	trans:cis
Tol	-70	1 h	15.0	6.220	14.66	2.36	1:1.70
Tol	-29	4 h	25.7	8.542	15.82	1.85	1:1.24
Tol	3	13 min	19.6	4.182	6.572	1.57	1.04:1
Tol	22	1 h	8.61	2.717	3.482	1.28	1.18:1

Counter Anion Effects

The effect of varying counter-anion size was considered in order to expand the quantum chemical model to a wider span of reaction conditions. According to the experimental data presented in Table *3-2*, as the size of the counter anion increases, the *trans:cis* ratio decreases. To understand these effects, each of the four species **3** isomers were optimized with either the BF_4^- or BARF$^-$ counter anion.

Pyrylium$^+$($\mathbf{X^-}$)	trans:cis
BF$_4$	3.66:1
PF$_6$	2.78:1
BARF	1.29:1

Figure 3-5 reports the calculated energies of the species **3** isomers with coordinated BF$_4^-$ anions in relation to the energies of the species **3** isomers without a coordinated counterion. When BF$_4^-$ is coordinated, the energies of species **3B** and **3D** are selectively stabilized relative to the energies of **3A** and **3C**. This stabilization of **3B** and **3D**, which both have a *cis* radical cation bond, ultimately shifts the equilibrium toward **3B**, the lowest energy species. With the equilibrium further shifted toward **3B**, the *trans:cis* ratio will increase because the ΔG between the lowest energy *trans* product and the lowest energy *cis* product increases from 1.9 to 6.0 kcal/mol when the BF$_4^-$ anion is coordinated.
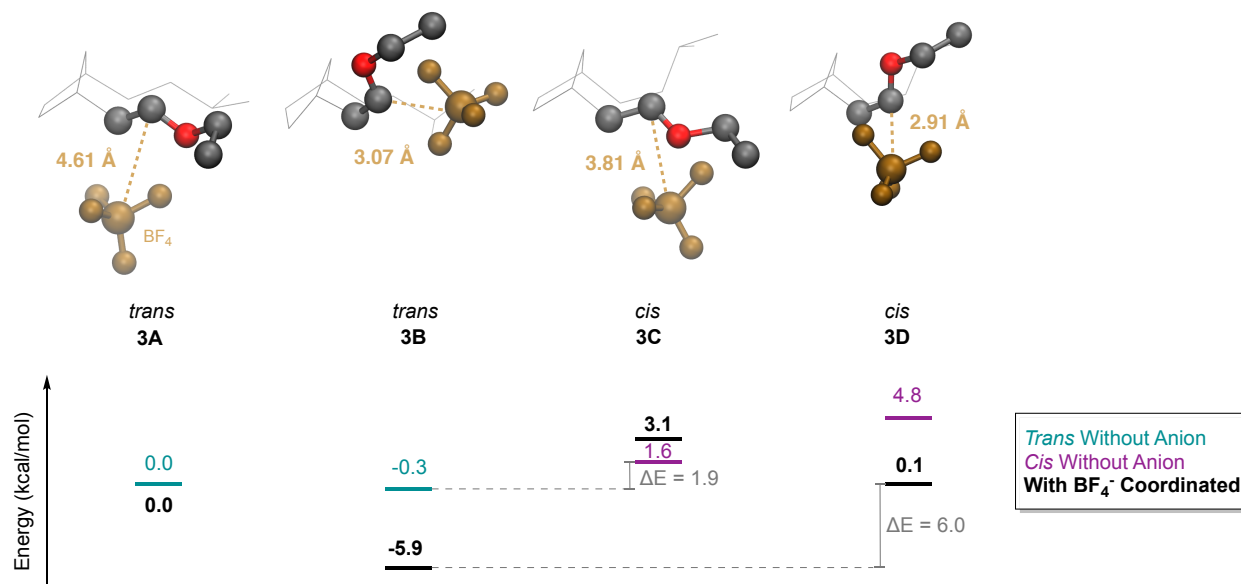
Figure 3-5. Relative energies of species 3 with and without counter anion. The black energies represent the energies of the species 3 isomers with the BF$_4$ anion coordinated relative to the energy of species 3A with the anion coordinated. The purple and teal energies are the energies without the anion coordinated. The gray energies are the difference in energy between the lowest energy cis and trans isomers. Charge separation reported in gold.

The two species with *cis* radical cation bonds (**3B** and **3D**) are stabilized when BF$_4^-$ counter anions are coordinated because having the chain end rotated up exposes the cation and allows the anion to coordinate more closely leading to stabilizing coulombic interactions between the charged species (Figure 3-5). In contrast, when the radical cation bond is in the *trans* conformation, such as in **3A** or **3C**, the anion is not able coordinate as closely, leading to greater charge separation (3.07 and 2.91 Å for **3B** and **3D** compared to 4.61 and 3.81 Å for **3A** and **3C**). Ultimately, this leads to a thermodynamic preference for species **3B** when BF$_4$ is coordinated and a high *trans:cis* ratio.

When the much larger BARF$^-$ counterion is coordinated to the various species **3** isomers, a different trend emerges. As shown in Figure 3-6, the *cis* isomers (**3C**, **3D**) are thermodynamically favored compared to the *trans* isomers (**3A**, **3B**) with the larger counter anion. While the rotation of the chain end was of significant energetic importance for the BF$_4^-$, BARF$^-$ is so large that the

local geometry is of less import, but that the geometry of the growing polymer chain becomes relevant. In the *cis* products, the growing polymer chain is pointed up, allowing for a large counterion to coordinate closely under the monomer and stabilize the cation. The *trans* products, however, have the growing polymer chain pointed down in such a way that the large BARF⁻ anion is unable to sufficiently stabilize the cation, leading to higher energies. When the BARF⁻ anion is coordinated, **3D** becomes the lowest energy isomer of species **3** and is 2.1 kcal/mol lower in energy than the most stable *trans* geometry. The stabilization of **3D** leads to a preference for the *cis* products, though this preference is not as strong as the *trans* preference with BF_4^- anions ($\Delta G = $ 2.1 vs 6.0 kcal/mol). Because the computational data considers a single low energy conformer, it most closely models the data taken at low temperatures.
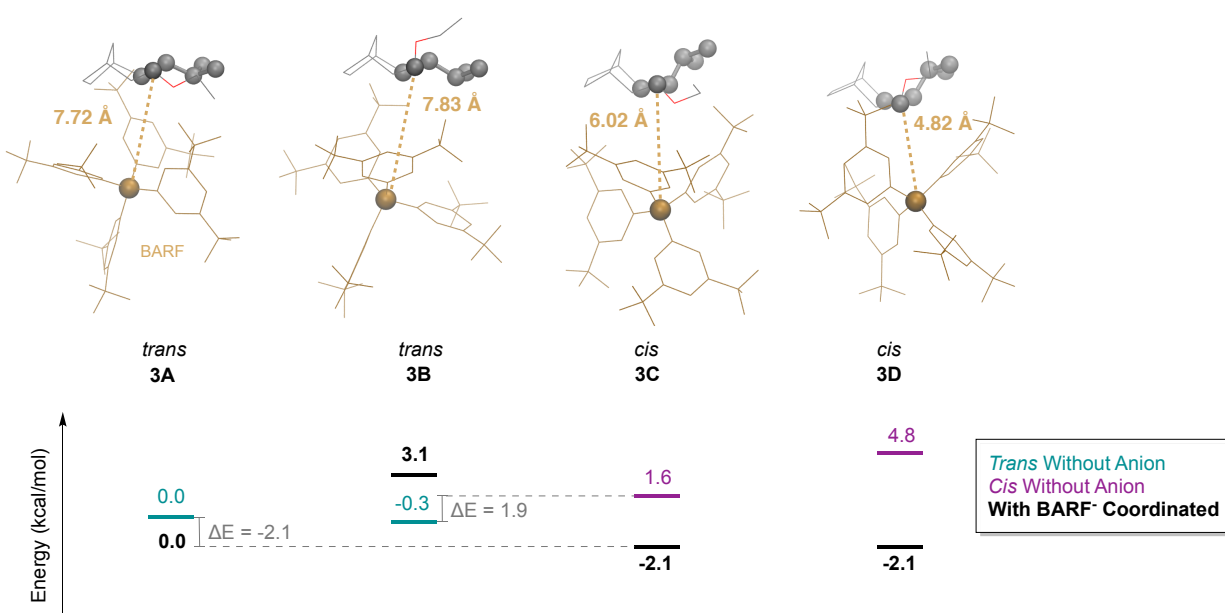
Figure 3-6. Relative energies of species 3 with and without counter anion. The black energies represent the energies of the species 3 isomers with the BARF anion coordinated relative to the energy of species 3A with the anion coordinated. The purple and teal energies are the energies without the anion coordinated. The gray energies are the difference in energy between the lowest energy cis and trans isomers. All energies reported in kcal/mol.

The data presented in Figure 3-5 and Figure 3-6 are solvent-corrected in a nonpolar solvent, toluene, but we expect the observed effects to disappear in polar solvents. If a polar solvent is used,

we don't expect the *trans* content to increase with increasing anion size. The polar solvents are already able to sufficiently stabilize the cation so exchanging for a smaller anion won't be as energetically impactful. Using a polar solvent or a small anion accomplishes the same task of stabilizing the cation which leads to higher *trans* content.

R-group Variations

Simulations then investigated the effect of chain-end R-group modification on reaction selectivity. Five different substitutions were made of varying steric size in place of ethyl to determine the effect of sterics on the *trans:cis* content of the product. In order of increasing size, the substituted groups were methyl (Me), ethyl (Et), cyclohexyl (Cy), adamantyl (Ad), and methyl-tri(ethyl) (CEt3). To quantify the steric size of each substitution, the Charton[124] parameter, derived from van der Waals radii, was considered. Charton values have long been used to construct linear free energy relationships in a variety of enantio- or stereoselective systems.[125–131] A linear relationship is obtained when the substituent Charton values are plotted against the logarithm of product enantiomeric ratios.[125,132] Computed ΔG between selected *cis* and *trans* products and the natural log of experimental *trans/cis* ratios showed linear correlation to the steric Charton parameter with R^2 values of 0.97 and 0.87 respectively (computed data in Figure 3-7, left).
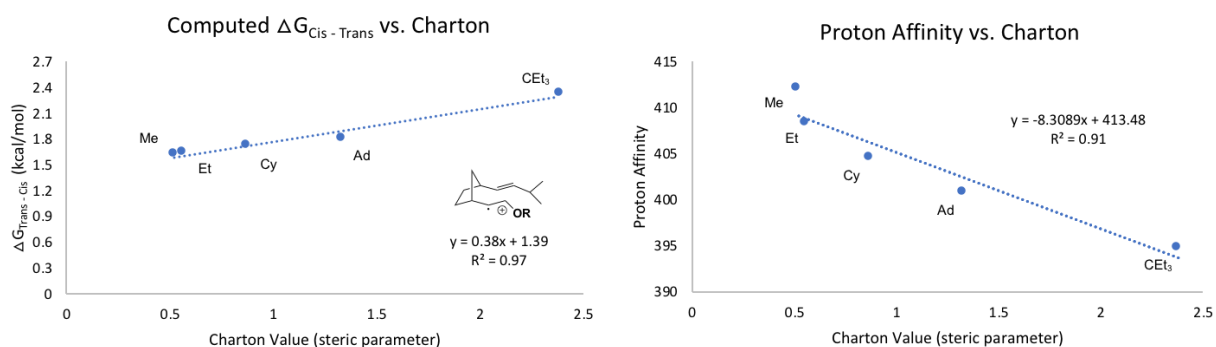
Figure 3-7. Computational ΔG quantities trend with the Charton value - a measure of steric size. Charton values (steric parameter) correlate with proton affinities (electronic parameter) for this subset of R-groups.

Although the substitutions had been made with sterics in mind, due to the nature of this data set, as these R-groups increase in size, they also have increased donating ability. As can be seen in Figure 3-7, right, for this subset of R-groups, the steric parameter trends reasonably well with the proton affinities of the alcohol of each R-group (R-OH). Thus, the experimental and computational data trend with the coupled electronic and steric parameters.

In order to delineate the electronic and steric contributions, the distortion/interaction model[133–135] of Houk was invoked (analogous model from Bickelhaupt is called the activation strain model[135–138]). In this model, the energy of a structure is decomposed into two contributions: the distortion energy, which is associated with the structural distortion that the reactants undergo, plus the interaction energy between the molecule and its substituents or the moleclues in a bimolecular reaction. In this work, the distortion energy comes from the increasing size of the R-groups, while the interaction energy comes from the increased donating ability of the R-groups. ΔG values were calculated for each of the stationary points with the various R-groups exchanged for a methyl group. The geometry from the initial calculations was maintained for all atoms aside from the methyl hydrogens to preserve the distortions enforced by the R-group while allowing the electronic contributions to be removed. The obtained energies were then analyzed to parse out the steric and electronic contributions to the total ΔG.

R-group	Electronic Contribution (kcal/mol)	Steric Contribution (kcal/mol)	Normalized $\Delta G_{cis\text{-}trans}$ (kcal/mol)
CEt$_3$	-0.320	1.023	0.703
Ad	-0.241	0.425	0.183
Cy	0.032	0.055	0.088
Et	-0.022	0.026	0.004
Me	0.000	0.000	0.000

Table 3-3. Electronic and steric contributions to the $\Delta G_{cis\text{-}trans}$ normalized to Me.

According to the calculated energies, sterics play an important role in determining the magnitude of the ΔG. A key geometric distortion to the structures that is dependent on the size of the R-group can explain the energetic differences due to sterics. As the R-groups decrease in size, the distance between the cation and the double bond decreases, allowing for more stabilizing π interactions in the structures with smaller R-groups (4.07 Å for CEt_3 to 3.73 Å for Me). More importantly, the difference in distance (*cis-trans*) decreases. For larger R-groups, there's a greater difference in distance between the cation and double bond (0.44 Å for CEt_3 to 0.18 Å for Me) and therefore a greater $\Delta G_{cis\text{-}trans}$.

R-group	distance (Å)
CEt_3	4.07
Ad	4.02
Cy	3.84
Et	3.74
Me	3.73
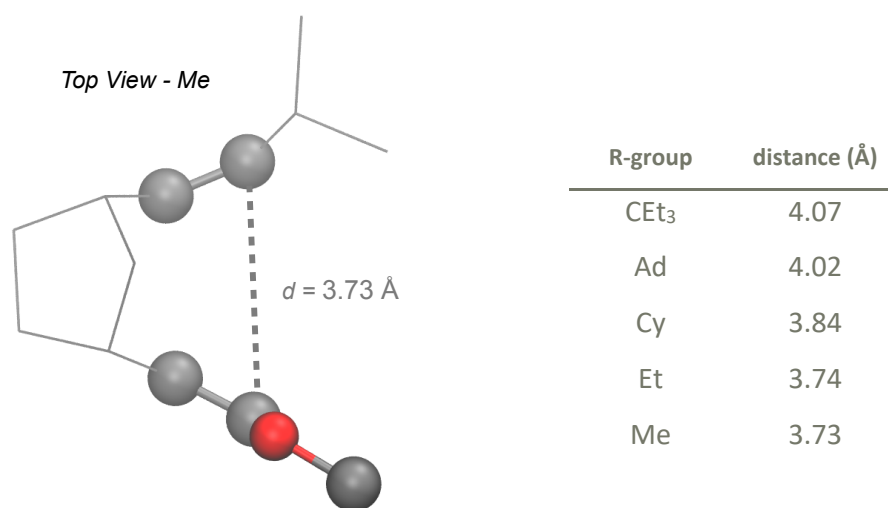
*Figure 3-8. Top view of Me-substituted **3D** showing atomic distance. Distances for other R-groups reported in the table. H atoms omitted for clarity.*

As the R-group increases in size, the ΔG increases which yields more highly *trans* product. Sterics contribute to increasing the ΔG because the change in cation-double bond distance increases with increasing steric size, effectively destabilizing the carbocation. Electronically, however, with increased R-group size, there is increased donating ability which provides

stabilization back to the cation. Thus, the steric and electronic effects of the R-groups are working against each other. In the CEt$_3$ case, there is 1.023 kcal/mol of steric destabilization combined with 0.320 kcal/mol of electronic stabilization resulting in a ΔG of 0.703 kcal/mol.

Based on the computations, it is clear that both electronic and steric factors are important for controlling the thermodynamic equilibrium of this system which regulates the microstructure of PNB. Whichever isomers best allow the cation to be stabilized are energetically preferred. Our results indicate that this photo-mediated ROMP process will produce PNB with high *trans* content when larger R-groups are on the chain end, or smaller counterions and more polar solvents are used, and that higher *cis* content can be achieved by exchanging to nonpolar solvents and larger counterions at low temperatures to minimize entropic effects.

Conclusions

Herein, we have reported the first mechanistic study of the metal-free ROMP process. We have demonstrated the ability of the metal-free ROMP system to polymerize norbornene monomers into PNB with varying degrees of stereoselectivity which can be modulated by various parameters including counter anion size, temperature, solvent, and size and donating ability of the R-group on the initiator. Using experimental and computational insights, a model was developed to explain the pattern of stereoselectivity exhibited in this metal-free redox-mediated system. A series of substituted initiators were evaluated in the ROMP of norbornene monomers. Highly *trans* polymers were generated in many cases. The data from both experiment and computation indicate that the *trans* products are thermodynamically favored under most reaction conditions, but product content can be shifted toward the *cis* product when the carbocation is sufficiently destabilized.

This trend is observed when ROMP is performed in toluene with BARF as the counterion at low temperatures. Higher degrees of *trans* preference can be obtained by stabilizing the carbocation.

Modifying the R-group on the initiator was observed to be stereo-electronically important. Larger R-groups shifted the product ratio toward greater *trans* content due to destabilization of the cation by pushing the double bond out of range for π stabilization. A sufficiently donating group could presumably overcome the steric effects to shift the equilibrium toward *cis* product.

The mechanistic insights gained in this study will not only aid in the development of new metal-free catalysts, but also provide increased predictive power in polymerizations mediated by these systems. Ability to have a high level of precision in tuning of the product content allows for complete modulation of the polymer. Insights gained in the studies presented in this chapter will provide a platform for the development of new metal-free systems capable of producing interesting and varied architectures via ring-opening metathesis polymerization.

Acknowlegements

Chapter 4. Investigating Steric and Electronic Variations of a Bimetallic Chromium Catalyst

This chapter is based on a collaborative project with the research group of Geoffrey Coates. Student contributors: Lilliana Morris, Anna Overholts, and Bryce Lipinski. Additional support from Timothy Jugovic from the Zimmerman Research Group.

Introduction

The vast majority of manufactured poly (propylene oxide) (PPO) is low molecular weight and atactic. Isotactic poly (propylene oxide) (*i*PPO), is not available commercially due in part to the high cost to obtain enantiopure propylene oxide and the lack of catalysts that can isospecifically polymerize *rac*-propylene oxide. A wide range of properties and precise tuning could be achieved through control of MW and tacticity.[139] Stereoregular polymers display superior mechanical and thermal properties compared to their atactic analogs. *i*PPO, for example, is a semicrystalline polymer with a T_m of 67 °C, while the atactic variation is an amorphous polymer with a T_g of -70 °C. Though the atactic variation is used in polyurethanes and commercially available foams, *i*PPO would be a semi-crystalline thermoplastic.[140] This increased strength allows for a much wider range of potential applications in plastics and packaging. A recent study revealed that *i*PPO possesses high tensile strength and yet can undergo photolytic degradation when exposed to UVA light, positioning it as a suitable replacement for nylon to reduce plastic waste.[141] An additional motivating desire to optimize an isospecific catalyst system comes from the potential to easily isolate enantiopure propylene oxide, a valuable synthetic building block.

In 2005, the Coates group reported the first production of highly isotactic PPO with a monometallic salen-based Co catalyst.[142] While this catalyst exhibited excellent selectivity, there

was little control over the molecular weight and therefore the dispersity of the polymers. Because the M_n was higher than predicted by monomer/catalyst ratios, this suggested that only a fraction of the catalyst was active.[142] It was proposed that polymerization occurs when the catalyst is in the crystalline phase by coordination of propylene oxide to a cobalt center adjacent to a cobalt-polymer alkoxide complex of the crystalline catalyst.[143] The reported crystal structure helped confirm that the selectivity occurred through enantiomorphic site control between chiral clefts of the packed catalyst.[143] Adjacent stacks in the crystal exhibited mirror image symmetry, precluding enantiopure crystals that would allow enantioselective polymerization.

Several catalyst systems aimed at achieving enantioselective polymerization of PO have since been developed. Three generations of these catalysts are outlined in Figure 4-1. First, a chiral bimetallic cobalt salen complex was designed (Figure 4-1, 1st Generation). This catalyst employed a chiral binaphthol linker to rigidly hold the metal centers with a similar spacing to that observed in the crystal structure. While the (salen)Co^{III} complex facilitated the synthesis of highly isotactic PPO, it produced polymers with uncontrolled molecular weight and high dispersity.[144,145] The lack of molecular weight control is attributed to slow or incomplete initiation and rapid propagation.

Next, a bimetallic (salen)Cr^{III} catalyst was investigated in an effort to gain more control over molecular weight (Figure 4-1, 2nd Generation). When used in conjunction with chain transfer agents (CTA), this catalyst produces *i*PPO of targeted molecular weight with moderate control of dispersity.[12,146] During polymerization, a dormant chain with an alcohol chain end enters the catalytic cleft, initiating proton transfer from the dormant chain to the active chain. This proton transfer makes the previously active chain dormant and the dormant chain active. Chain transfer allows for production of multiple polymer chains per catalyst and control of molecular weight by variation of the monomer to chain transfer agent ratio.[147–149] Molecular weight control from CTAs

comes from equilibrium with competition between the monomer binding and the CTA binding. At lower CTA concentrations then, the CTA is less likely to bind to the catalyst so the molecular weight will be larger. At higher CTA concentrations, the equilibrium shifts toward preferential CTA binding, so chains terminate at lower, albeit more predictable, molecular weights. This catalyst, however, requires high loading of chain transfer agent in order to control dispersity which in turn, impedes the synthesis of higher molecular weight polymers.

Finally, with the goal of attaining increased molecular weight control, a (salen)Cr^{III} catalyst originally developed by Jacobsen and co-workers for the asymmetric ring-opening of cyclopentane oxide was investigated (Figure 4-1, 3rd Generation).[150] The flexible alkyl linker allows for more conformational freedom compared to the more rigid binaphthol linker used in the 1st and 2nd generation catalysts. The flexibility of the alkyl linker introduces several new degrees of rotational and translational freedom that were previously inaccessible. The flexibility is hypothesized to allow the catalyst to use the added degrees of freedom to adapt a conformation for polymerization that may have been inaccessible to the catalyst operating in the crystalline form or with the rigid linker. This most recent linker modification has yielded catalysts with excellent enantioselectivity in addition to producing polymers with dispersities as low as 1.3-1.4.[151] Unfortunately, the most active catalysts only display a conversion of 47% compared with historic conversions of up to 93% for catalysts that readily produce atactic PPO.[152,153] Optimizing catalytic activity in the 3rd generation catalysts remains a goal of this research.
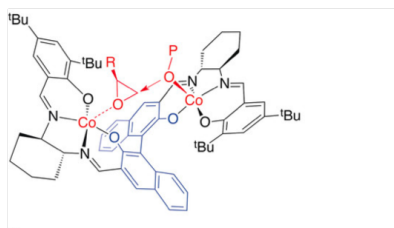
1st Generation
- Rigid binapthol linker
- Highly enantioselective
- Poor MW control
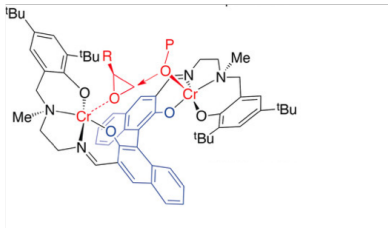
2nd Generation
- Rigid binapthol linker
- Highly isoselective
- Moderate MW control
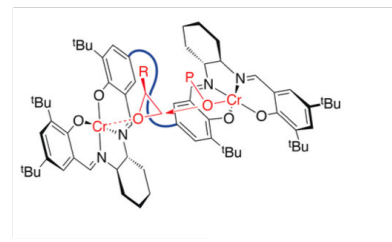
3rd Generation
- Flexible alkyl linker
- Excellent enantioselectivity
- Excellent MW control

Figure 4-1. Previous work on three generations of stereoselective bimetallic catalysts for PPO polymerization.

Historically, changing the catalyst anion[154–157] and ligand substituents[158–164] has been an effective way to modulate catalyst activity and selectivity. More recently, ongoing research has turned to catalyst ligand design to simultaneously control both molecular weight and isotacticity of poly (propylene oxide). Coates and co-workers demonstrated that ligands that are more electron withdrawing lead to decreased rates of polymerization but eliminate epimerization and transesterification side reactions.[164]

The project described within this chapter seeks to explore possible geometries of the highly flexible 3rd generation catalyst and subsequently report the configuration adapted by the metal centers and salen ligand. While a few simulation studies have been performed on previous versions of the catalyst to determine selectivity and mechanism,[12,143] this study will be the first investigation into the 3rd generation catalyst. We hypothesize that similarly reported steric constraints from older catalysts will still be relevant in the new system. Simulations of the propagation step will be employed to provide insight into the stereoelectronic features that control catalyst activity and enantioselectivity. These insights will subsequently be used propose and evaluate substitutions at various positions on the catalyst that modulate either sterics or electronics.

The proposed substitution sites at the ortho and para positions of the aromatic rings on the salen ligand are presented in Figure 4-2. Substitution at these sites has been selected due to previous reports of steric and electronic substituents being able to effect activity or selectivity of similar catalysts for PO polymerization. Steric hinderance in the ortho position has led to greater selectivity in a monometallic salen cobalt catalyst[157] and more electron deficient catalysts have been reported to exhibit lower rates of polymerization in an aluminum-based salen catalyst.[164]

Herein, quantum chemical calculations will be employed to find low-energy conformers of the new flexible catalyst, determine the stereoelectronic features that control enantioselectivity, and provide insight into how exchanging substituents effects catalytic activity.
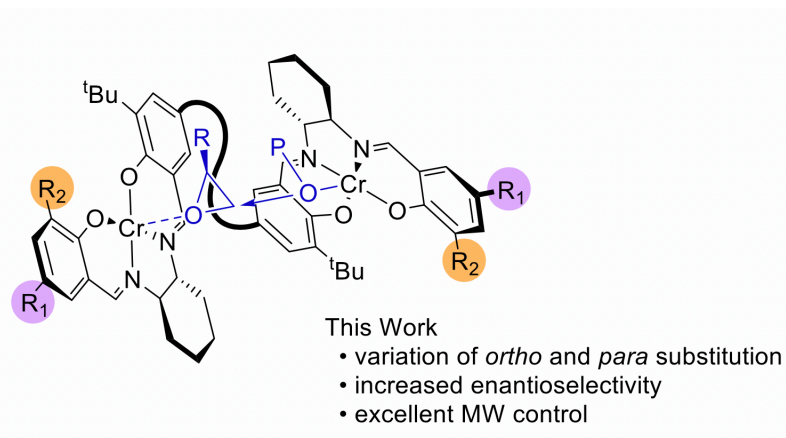
Figure 4-2. Design of a strategically substituted bimetallic chromium catalyst for the enantioselective polymerization of propylene oxide.

Computational Details

Quantum chemical calculations were conducted utilizing Density Functional Theory (DFT) with the Q-Chem 4.3 ab initio quantum chemistry package. Consistent with previous work,[162] gas phase geometry optimizations were performed with the B3LYP density functional[93] with spin unrestricted formalism and a mixed 6-31G/6-31G* basis set.[121] The 6-31G* basis set was applied to all heavy atoms and reactive carbons, while hydrogens and non-reactive carbons were treated with 6-31G basis set (Figure S12). In line with previous work,[12] it has been determined

that the heptet state corresponding to two chromium (III)s of spin 3/2 is the preferred electronic state. Single point energies calculated with the Solvent Model based on Density (SMD) solvation model were performed at B3LYP level of theory with def2-TZVP basis set and def2/J auxiliary set and RIJCOSX integration method.[122,123,165,166] Dimethoxyethane (DME, $\epsilon=7.2$) was used as the implicit solvent. The [OAc^{F3}]$^-$ anions were exchanged for [Cl]$^-$ anions on the metal centers. Transition state (TS) structures were determined using the double-ended Growing String Method (GSM).[50,51] GSM was used to determine the transition state between an optimized reactant and product by finding the minimum energy pathway and TS saddle point between the two structures on the potential energy surface (PES). GSM calculations were considered converged when the transition state node had an RMS gradient less than 0.0005 Ha/Å. The EMSL Basis Set Library was the source of all basis sets used.[167]
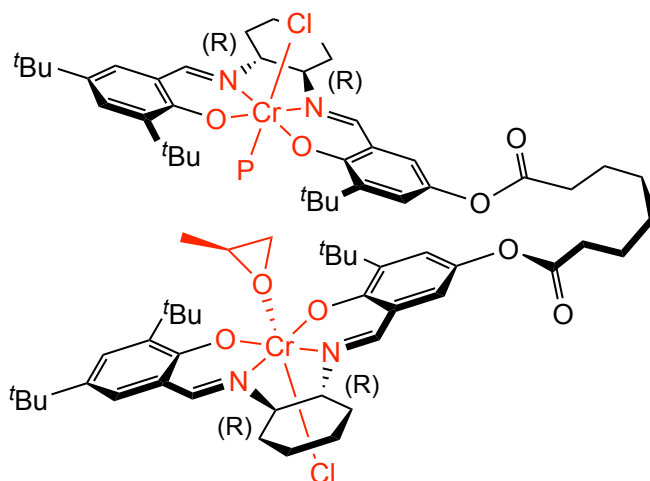
Figure 4-3. Representation of the mixed basis set application. Atoms in red were modeled with the 6-31G* basis set while black atoms were modeled with the 6-31G basis. "P" marks the place of the polymer.

Results and Discussion

To begin, we establish a computational model of the catalyst with geometric features that that can be assessed to determine a structure-activity relationship and incorporated into future catalyst design. In previous studies, bimetallic catalysts for the polymerization of PO contained a rigid binaphthol linker to hold the metal centers in proximity to each other. With the modification of the catalyst linker to the more flexible alkyl linker for this work, it was important to find low energy conformers that could provide insight into the tunable parameters that control propylene oxide polymerization including appropriate metal-metal spacing and enantiomorphic site control.[143,144,151] Ideal metal-metal separation will allow the metals to be close enough that frequent bond formation may occur between a bound monomer and alkoxide, but not so close as to prevent subsequent monomer coordination. Along these terms, a recent study confirmed that the length of the alkyl linker greatly impacted catalyst activity, and specifically, that a linker length of six methylenes yielded the most active catalyst.[151] Additional metrics that describe the active site and monomer alignment include S_N2 angles, bond formation distances, and ligand deformation angles that allow the catalyst to selectively enchain one enantiomer over the other.

For these initial conformational evaluations, the salen ligand is substituted with ^{t}Bu groups occupying each of the ortho and para positions of the salen ligands. Consistent with transition state structure geometries from a previous study,[162] stable catalyst confirmations were found which held the catalyst in a closed clam-shell configuration. The closed configuration is energetically favorable due to the invocation of stabilizing interactions between the pi systems of the salen ligands as well as dispersion interactions between the ^{t}Bu and cyclohexyl moieties. The π stacking and dispersion interactions provide an energy advantage of 53.3 kcal/mol for the closed conformation relative to the open catalyst. Figure 4-4 shows that this closed, clam-shell

54

configuration holds the aromatic rings within 3.4 to 3.9 Å and allows for stabilizing π stacking between the aromatic rings of the salen backbone. The closed configuration holds the chromium metal centers at a distance of 6.7 Å which is in the same range (6 - 7 Å) that previous generations of the catalyst have operated.[143,144,151]
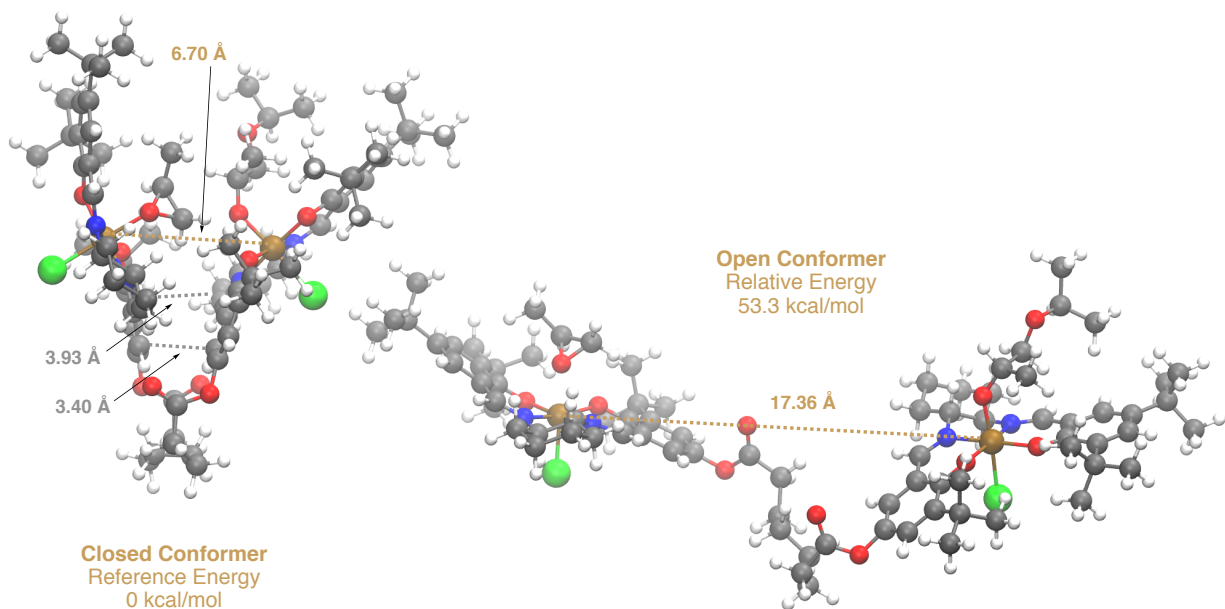
Figure 4-4. Closed and open conformers of the bimetallic Cr catalyst. In the closed conformer, the stabilizing pi stacking between the salen ligands is achieved, giving an energy advantage to the closer conformer.

Next, it was important to determine if the catalyst preferred to stack head-to-head or head-to-tail. The head-to-head configuration has the diaminocyclohexane moieties of the salen backbones aligned so that they are facing the same direction and stacked one on top of the other while the head-to-tail configuration has the *t*Bu region of one ligand stacked over the diaminocyclohexane region of the other ligand. Figure 4-5 illustrates the two models. The head-to-tail stacking was identified as the more likely configuration as the head-to-tail model provided an 18.8 kcal/mol energy advantage over the head-to-head model.

In the head-to-tail model, the ^{t}Bu groups from one salen ligand are able to provide stabilizing dispersion interactions with the cyclohexyl groups of the other salen ligand. This stabilization is possible due to the close proximity between the ^{t}Bu and cyclohexyl moieties (between 2.2 and 2.4 Å). In the head-to-head conformation, the cyclohexyl moieties from opposite ligands are able to interact in the same range (~2.4 Å), but the ^{t}Bu moieties are at a further distance. In addition, the bulkiness of the ^{t}Bu groups confers steric hinderance on the head-to-head model that is avoided in the head-to-tail model.

In the head-to-head model, the charged species on the salen ligands are aligned directly on top of each other leading to electrostatic repulsion between pairs of oxygen atoms. In order to mitigate these repulsions, the geometry offsets. By contrast, in the head-to-tail model, the geometry is oriented such that nitrogen atoms are aligned over oxygen atoms which mitigates the electrostatic repulsions between oxygen pairs as shown in Figure 4-5.

Finally, the Cr-Cr separation in these models is 6.70 Å for the head-to-tail model and 5.83 Å for the head-to-head model. Because this is a charged species and much of the charge would reside on the Cr(III) metal centers, it is plausible that repulsive electrostatic forces additionally elevate the energy of the head-to-head model.

Previously reported crystal structures of a salen-Co catalyst from the Coates group have revealed preference for head-to-tail stacking,[143,168] and Jacobsen monometallic and linked salen-Cr catalysts have also been reported to work in a bimetallic fashion with this head-to-tail orientation, further strengthening the conclusion.[150]

Head-to-Tail
Reference Energy
0.0 kcal/mol

Head-to-Head
Relative Energy
18.8 kcal/mol
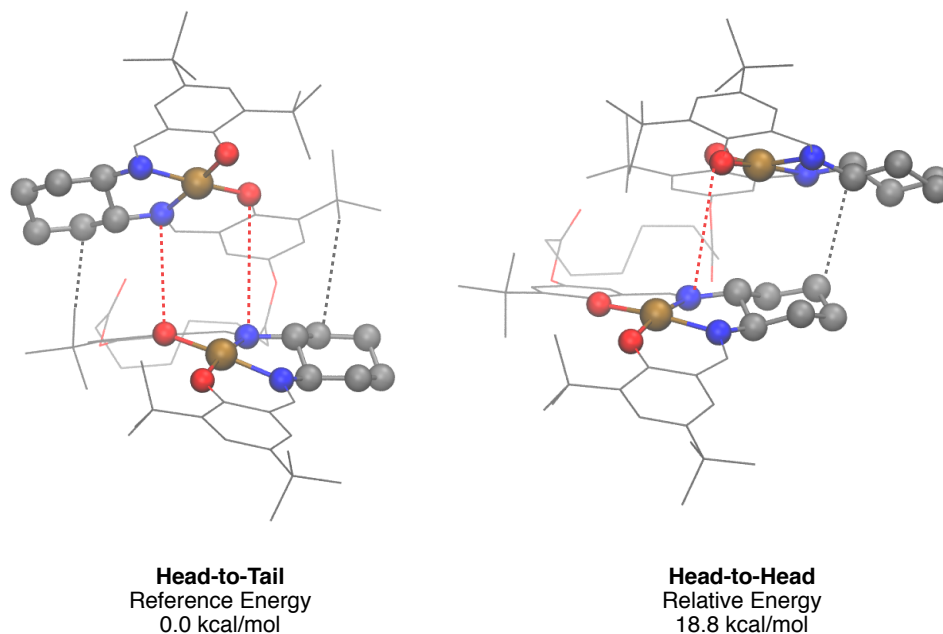
Figure 4-5. Head-to-head vs head-to-tail stacking. The head-to-tail configuration is energetically preferred by 18.8 kcal/mol. H atoms have been omitted for clarity.

Two possible configurations for the catalyst emerged based on how the flexible alkyl linker can attach to the two salen arms of the catalyst. As shown in Figure 4-6, the linker could attach to one side or the other of the salen ligands, all else being the same. The minimum energy reaction path for the *(S)*-conformer is lower in energy than the propagation step for the *(R)*-conformer. Upon monomer addition with *(S)*-PO, there is a 4.53 kcal/mol energy preference for the *(S)*-conformer of the catalyst. The relative transition state energies are 15.37 kcal/mol and 8.61 kcal/mol for the *(R)*- and *(S)*-conformers, respectively.

The preference for the *(S)*-conformer comes from orientation of the PO in the catalytic cleft. In the *(S)*-conformer, the PO methyl points toward sterically unhindered space, while the *(R)*-conformer causes the PO methyl to point toward the sterically hindered linker region of the catalyst. These data demonstrate a preference for the *(S)*-conformer of the catalyst which has been used as the model throughout the rest of the calculations for this chapter.

(S)-conformer　　　　　　　*(R)*-conformer
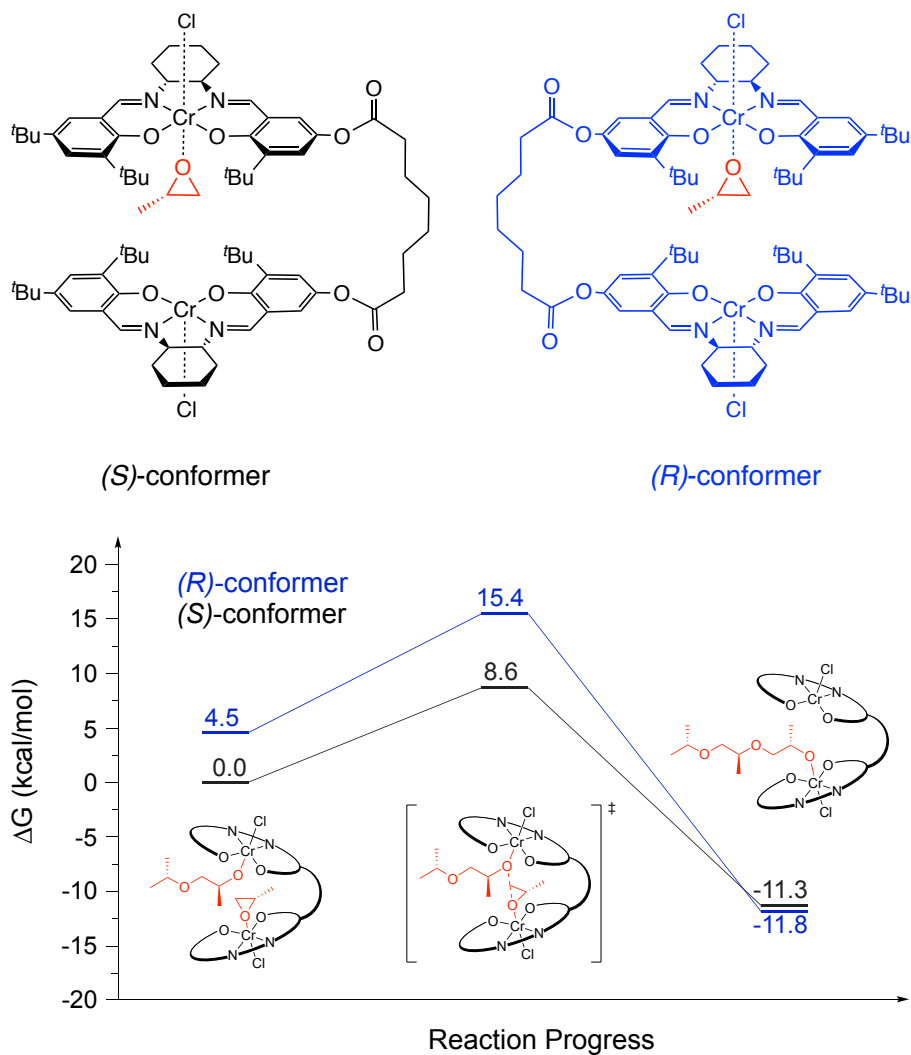
Figure 4-6. Propagation of (S)-PPO in (R)- and (S)-conformers of the catalyst (blue and black, respectively). The (S)-conformer has the lower energy reaction path and transition state energy. All energies reported in kcal/mol.

Finally, while modeling these structures, an unexpected degree of freedom presented itself in the formation of a kink in the salen ligand. When optimizing, the metal center with a coordinated polymer chain often found a minimum when the salen ligand bent away from the other metal center. There is evidence from previous generations of the catalyst that this kink is found in its crystal structures,[145,168] presumably to help with packing, but this is the first indication that the salen ligand may adapt this deformation during polymerization in solution.

As demonstrated in Figure 4-7, there is little energetic penalty for one arm of the catalyst to bend away from the other via a kink in the salen ligand. If this feature is new to the catalysts that incorporate the flexible alkyl linker, then this geometric insight could explain why this generation of the catalyst supplies greater molecular weight control. The kink in the salen ligand opens up the catalytic cleft which in turn reduces congestion for each monomer addition.
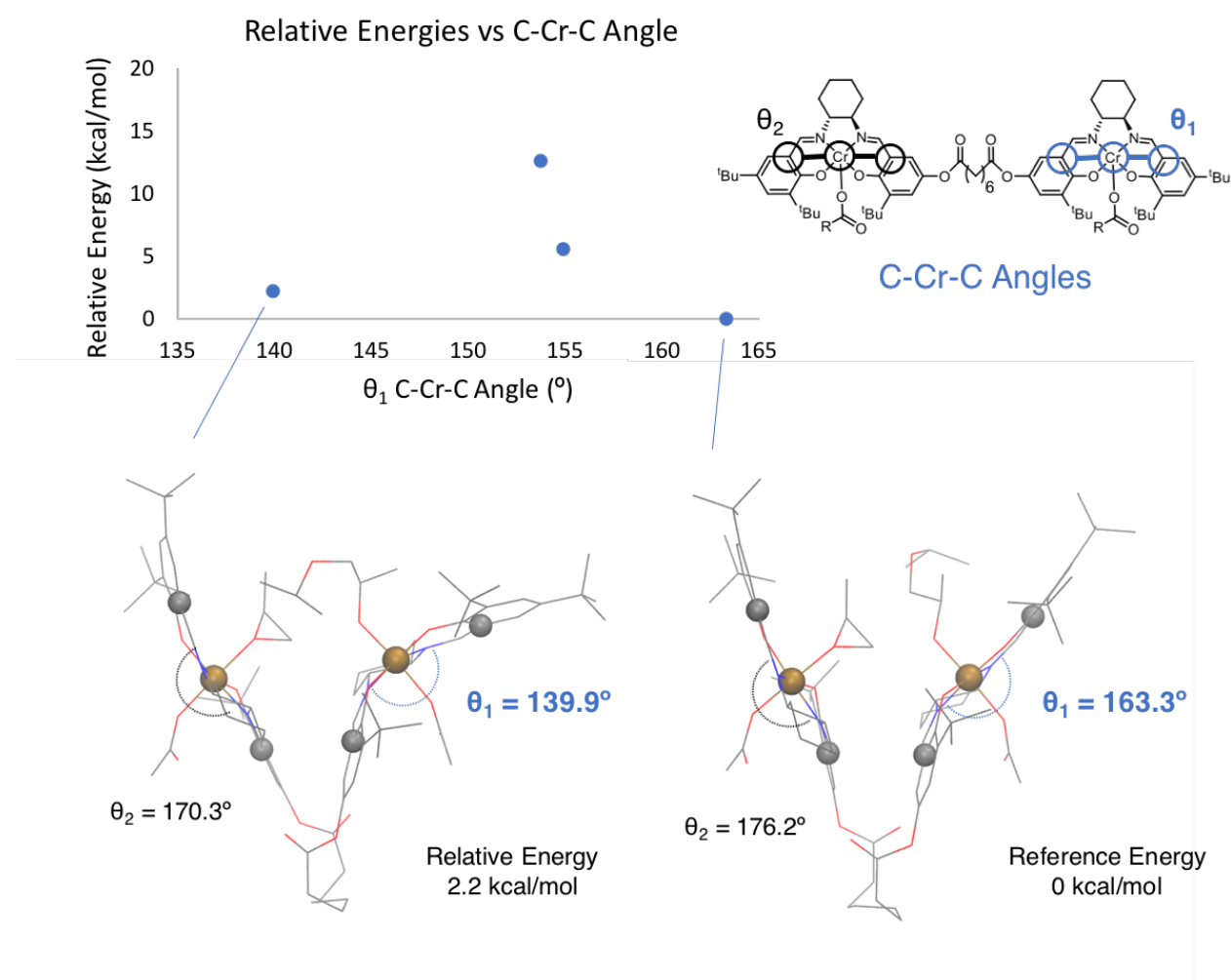
Figure 4-7. The kink found in the salen ligand of optimized geometries is measured through the C-Cr-C angles highlighted. Despite wide variation in these angles, the energies of the structures are stable. Hydrogen atoms omitted for clarity.

With this model of the catalyst in place (closed, head-to-tail, *(S)*-conformer, kinked), our efforts turned toward modeling and understanding the enantioselectivity of the catalyst by comparing the ability of the catalyst to polymerize *(R)*-PO verses its ability to polymerize *(S)*-PO. For our purposes, the calculations are all performed with all *(R)* stereocenters on the diaminocyclohexanes of the catalyst, as seen in Figure 4-3, which enantioselectively polymerize *(S)*-PO.[144,145,169]

For the *t*Bu catalyst, the *(S)*-PO provides the lower energy of activation, confirming that our model is capturing the steric interactions that have been previously observed and reported as controlling the catalyst selectivity.[12] The atomistic simulations provide a 3D structural explanation for the observed *(S)*-PO selectivity. First, monomer rotation gives an advantage to the *(S)* enantiomer in terms of proximity of the reactive atoms to each other since the distances of the breaking and forming bonds are closer than in the TS for *(R)*-PO (2.23 and 2.06 Å for (R) and (S), respectively). As shown in Figure 4-8, the *(R)*- and *(S)*- monomers take different orientations at the propagation steps, TS_R and TS_S. In the *(R)*-PO TS (Figure 4-8, Left), the methyl group points up, leading to steric interactions with both the salen ligand and the growing polymer. In the *(S)*-PO TS (Figure 4-8, Right), however, the methyl points out of the cleft, avoiding steric clashes with surrounding atoms. Additionally, the rotation of the propylene oxide monomer allows the *(S)*-PO monomer to achieve slightly better alignment for an S_N2-type attack (155.9° for *(R)*-PO and 161.8° for *(S)*-PO, compared to the preferred angle of 180°). The greater strain on TS_R leads to the higher energy transition state.
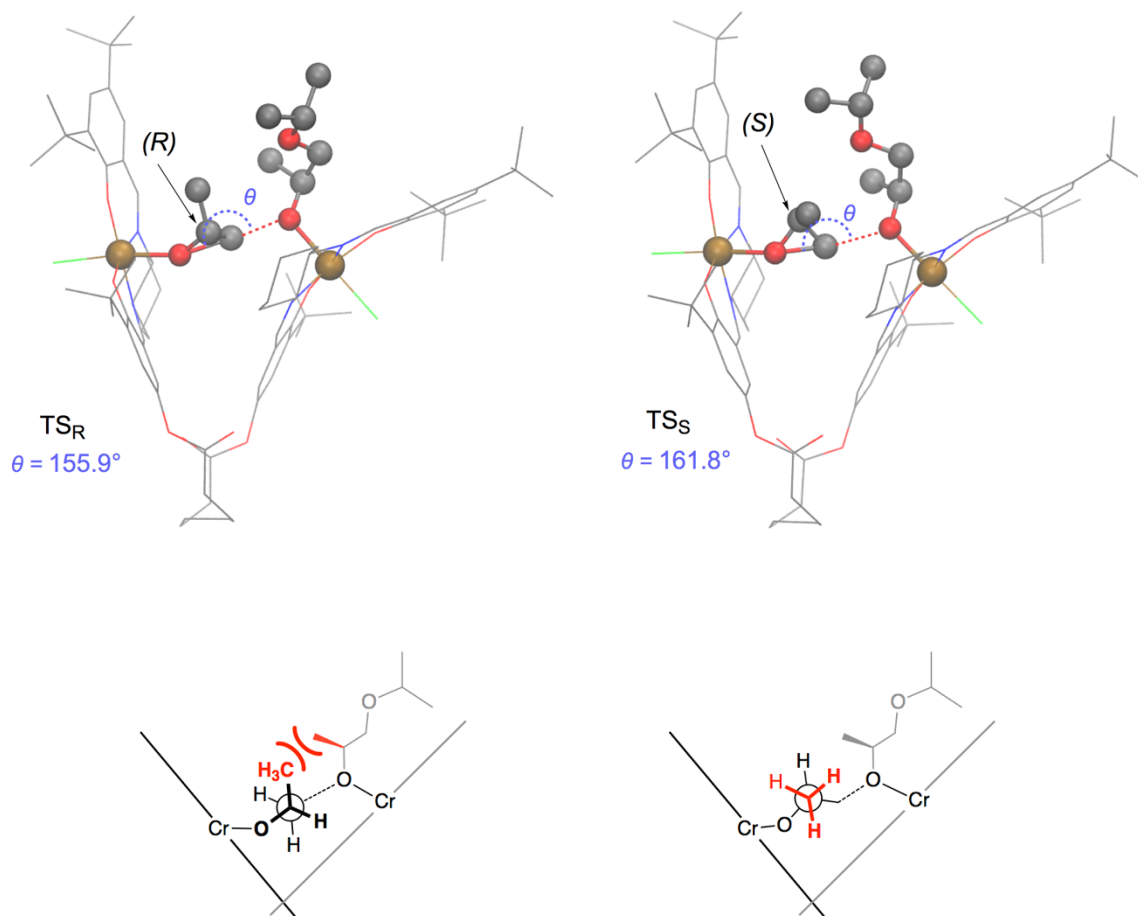
Figure 4-8. Stereochemical model for propagation transition states for (R)-PPO and (S)-PPO. H atoms have been omitted for clarity.

Para Substitutions

Though these systems have been evaluated with a variety of epoxides,[145,170] and thorough analyses have been performed on the effects of the cocatalyst,[170] chain transfer agents,[12] and linker,[151,169] little is known about substituent effects on the catalyst itself. In order to determine if a more active or more selective catalyst could be designed, we began by substituting ligands of varying size[124] and electronic properties[171] at the para position of the salen ligand (Figure 4-9). The expectation was that increasing bulk in the para position would diminish activity while

decreasing bulk could lead to more frequent ring-opening between the bound monomer and polymer alkoxide species. It has been observed that electron deficient catalysts exhibit lower rates of polymerization in salen alumninum based catalysts[164] so we hypothesized similar trends would hold in our system.
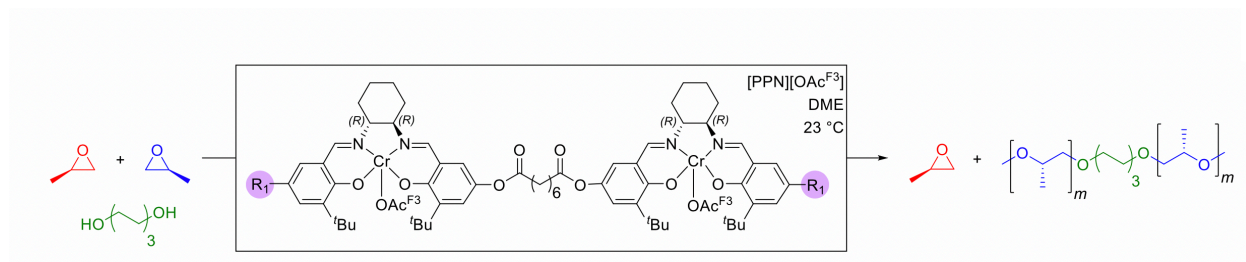
Figure 4-9. Substitution at the R1 para position highlighted in purple.

R_1	σ	υ_{ef}	Conversion (%)[b]	TOF (h^{-1})[c]	M_n theo. (kDa)[d]	M_n GPC (kDa)[e]	Đ[e]	k_{rel}
Me	-0.17	0.52	19.5	257	07.0	10.5	1.08	43
Ad	-0.13	1.33	11.2	147	04.2	7.4	1.09	52
^tBu	-0.12	1.24	25.5	347	09.0	12.3	1.10	57
CPh$_3$	0.02	2.92	5.6	079	02.7	-[g]	-[g]	37
OMe	-0.27	0.36	2.5	034	01.1	-[g]	-[g]	45
F	0.06	0.27	7.8	105	03.2	04.7	1.13	37
Cl	0.23	0.55	26.0	357	10.4	14.1	1.11	32
Br	0.23	0.65	11.4	163	05.0	-[g]	-[g]	31

Table 4-1. Effect of variation of para group on catalyst activity for the polymerization of propylene oxide. Experimental data from the Coates Group at Cornell University.[a]

[a] Polymerization conditions: 1 mL PO; [PO] = 4.8 M in DME; [PO]:[catalyst]:[cocatalyst] = 4,000:1:1; trxn = 3 h. [b] Determined gravimetrically. [c] mmol PO consumed·mmol catalyst-1·trxn-1. [d] mg polymer/(mmol catalyst + mmol CTA). [e] Determined by GPC relative to polystyrene standards at 30 °C in THF. [g] Not determined because peak fell outside the calibration region.

Substituting to adamantyl at the R1 para position decreases activity with little effect on selectivity. Exchange to a larger and more withdrawing -CPh$_3$ group drastically decreased conversion and selectivity factor (k_{rel}). It is suspected that this is due to the bimetallic nature of the

catalyst – with increased bulk in the para position, the two metals are no longer able to reach an ideal distance for cooperative interaction. Exchange to a smaller methyl group had little diminishing effect on either activity or selectivity.

The most promising catalyst, para methyl, was selected for further evaluation via computation. Transition states and reaction paths for propagation were obtained using GSM for the ^{t}Bu catalyst to compare with the para methyl substituted catalyst. Figure 4-10 shows the potential energy surfaces for these two catalysts. The computed mechanism for propagation involves an S_N2-type attack on the epoxide for a ring opening which involves both metal centers. Comparable S_N2 angles (163.3 vs 163.5, para methyl vs ^{t}Bu) at the transition states correspond to the similar energies of activation and experimentally reported activities. The bond formation distances (2.03 vs 2.13 Å, para methyl vs ^{t}Bu) give a slight geometric advantage to the para methyl catalyst which results in a slightly lower computed energy via quantum chemical calculations.
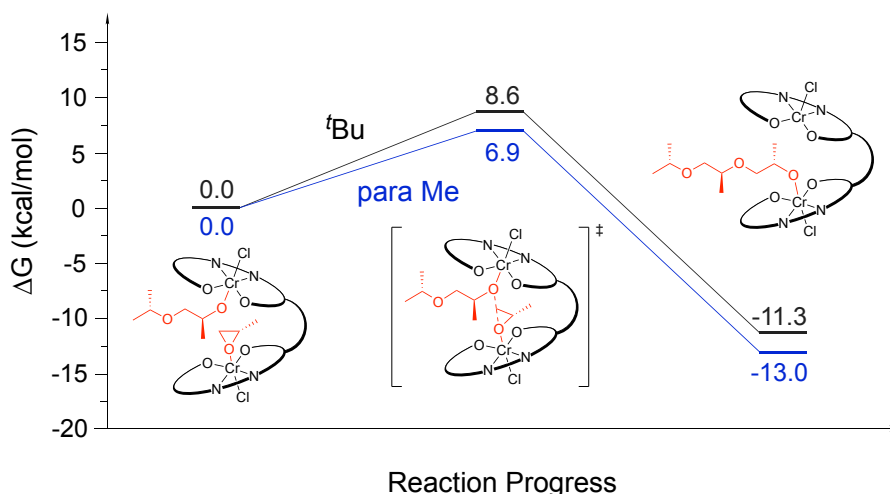
Figure 4-10. Propagation potential energy surfaces and mechanism for the tBu catalyst and the para methyl substituted catalyst

Electronic effects were next considered by substituting methoxy, fluoro, chloro, and bromo at the R1 para position. Catalyst activity was observed to depend significantly on the electronic parameter. Comparing the fluoro substituent to the methoxy, for example, there is a clear

distinction between activities of the respective catalysts. While the methoxy catalyst had negligible conversion, the fluoro catalyst produced a small amount. It can therefore be concluded that electron donating groups reduced catalytic activity. Similarly, using a para chloro group yields the same activity as a para ^{t}Bu group even with its decreased size. Again, comparable activation energies correspond to comparable bond formation distances (2.08 vs 2.13 Å, para chloro vs ^{t}Bu) and S_N2 angles (163.9 vs 163.5 °) at the transition states. Unfortunately, however, the catalyst with the para chloro group has a relative rate of *(R)*-PO and *(S)*-PO enchainment that is less selective than the ^{t}Bu catalyst (selectivity factor k_{rel} of 32 vs 57, respectively). Figure 4-11 shows the potential energy surfaces for the ^{t}Bu and para substituted chloro catalysts. The computed energies of activation are within approximately 1 kcal/mol – within DFT error for catalysts with similarly reported rates.
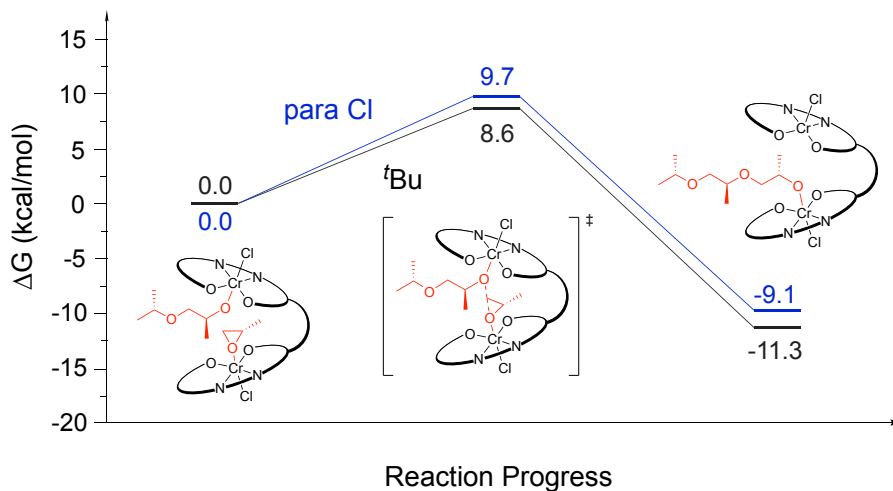
Figure 4-11. Propagation potential energy surfaces and mechanism for the tBu catalyst and the para chloro substituted catalyst.

Ortho Substitutions
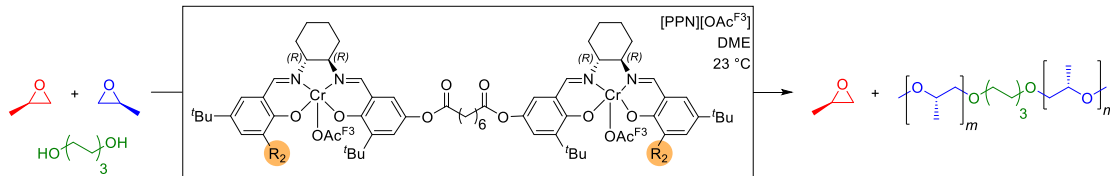
Figure 4-12. Substitution at the R2 ortho position highlighted in orange.

R_2	σ	υ_{ef}	Conversion (%)[b]	TOF (h^{-1})[c]	M_n theo. (kDa)[d]	M_n GPC (kDa)[e]	$Đ^e$	k_{rel}
Me	-0.17	0.52	<1	-	-	-[g]	-[g]	-
*t*Bu	-0.12	1.24	25.5	347	9.0	12.3	1.10	57
Ad	-0.13	1.33	9.0	104	3.6	06.2	1.14	134

Table 4-2. Effect of variation of the ortho group on catalyst activity for the polymerization of propylene oxide. Experimental data from the Coates Group at Cornell University.

[a] *Polymerization conditions: 1 mL PO; [PO] = 4.8 M in DME; [PO]:[catalyst]:[cocatalyst] = 4,000:1:1; trxn = 3 h.* [b] *Determined gravimetrically.* [c] *mmol PO consumed·mmol catalyst-1·trxn-1.* [d] *mg polymer/(mmol catalyst + mmol CTA).* [e] *Determined by GPC relative to polystyrene standards at 30 °C in THF.* [g] *Not determined because peak fell outside the calibration region.*

While substituting at the para position enabled synthesis of a more active catalyst in the para chloro catalyst, the increase to activity was small and at a significant cost to selectivity. In an attempt to create a more selective catalyst, the ortho position was exchanged to a methyl and adamantyl. Previous studies on a salen cobalt catalyst suggest that steric bulk in the ortho position leads to increased selectivity while steric bulk around the metal center leads to decreased selectivity.[146,172] The ortho methyl substituted catalyst yielded negligible *i*PPO. The ortho adamantyl substituted catalyst also exhibited lower activity but yielded a significantly increased selectivity. The k_{rel} of the ortho-substituted adamantyl catalyst was found to be 134 compared to 57 for when *t*Bu was substituted at the para position.

The ortho adamantyl catalyst's selectivity is observed computationally by having an increased $\Delta\Delta G^{\ddagger}$ between the reaction paths for the *(R)*-PO and *(S)*-PO relative to the other catalysts

that were studied. The $\Delta\Delta G^{\ddagger}$ for the ortho adamantyl catalyst is 3.3 kcal/mol compared to $\Delta\Delta G^{\ddagger}$s of 0.1 to 0.3 kcal/mol for the other computed catalysts. Figure 4-13 reports the minimum energy reaction paths for the propagation of an *(S)*-PO and an *(R)*-PO in the ortho adamantyl substituted catalyst.
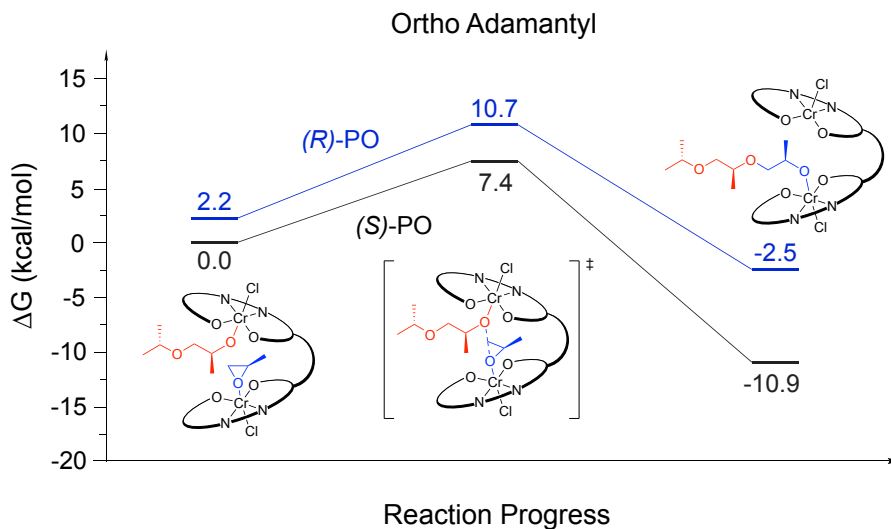
Figure 4-13. Potential energy surfaces for the propagation of both (S)- and (R)-PO in the ortho adamantyl catalyst. The ortho adamantyl substituted catalyst has the greatest ΔΔG‡ of 3.3 kcal/mol compared to 0.1 to 0.3 kcal/mol for other observed catalysts. The pathway for (S)-PO is in black while the pathway for (R)-PO is in blue.

This increased selectivity is due to the ability of the adamantyl group to more closely interact with the PO monomer. Due to its inability to rotate, the adamantyl group cannot accommodate an *(R)*-PO monomer like the *t*Bu group can. As demonstrated in Figure 4-14, compared to the *t*Bu catalyst, the ortho adamantyl substituted catalyst holds the PO monomer and growing *i*PPO polymer more rigidly in place, leading to increased selectivity for the *(S)*-PO monomer. The distance between the ortho adamantyl groups is shorter than the distance between ortho *t*Bu groups (8.33 vs 9.65 Å) leading to a narrower catalytic cleft. The distance between the PO methyl and the closer ortho group is comparable between the two catalysts (4.85 vs 4.49 Å),

but the distance between the PO methyl and the opposite ortho group is shorter in the ortho adamantyl catalyst (4.75 vs 5.71 Å). The fact that adamantyl has no rotatable bonds in addition to its proximity to the monomer means that it cannot rotate out of the way to accommodate an *(R)*-PO monomer.

The geometric factors previously considered for activity; metal-metal distances (6.86 vs 6.82 Å, ortho Ad vs *t*Bu), S_N2 angle (164.7 vs 163.5°), and O-C bond formation distance (2.11 vs 2.03 Å); are all similar which suggests that the proximity of the ortho adamantyl groups is responsible for selectivity.

Ortho Adamantyl   Ortho *t*-Butyl
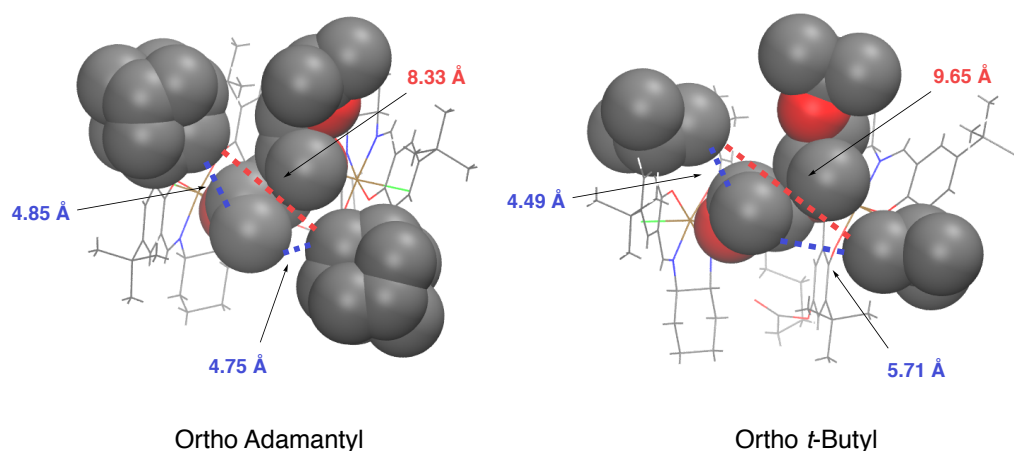
Figure 4-14. Stereochemical model for ortho adamantyl's increased selectivity. On the left is the transition state for propagation of the tBu catalyst and on the right is the transition state for propagation of the ortho substituted adamantyl catalyst. The increased steric bulk and rigidity in the ortho position holds the (S)-PO more firmly in place in the adamantyl catalyst.

Based on the simulations, it is evident that exchanging for a larger, more rigid group in the ortho position provides increased selectivity. The increased selectivity comes at the cost of diminished activity, however. Because the adamantyl groups make the active space tighter, this means that monomers will enter it less often, but when they do, they will all be oriented the same way, leading to high enantioselectivity.

Experimentalists were unable to improve upon the *t*Bu catalyst in terms of increased

activity and selectivity. Computationally, we were able to determine that chemically intuitive features thought to control activity are similar in the catalysts that performed well. Optimizing these features would lead to increased activity. The metrics considered were Cr-Cr distance, S_N2 angle, and O-C forming bond distance. In the most active catalysts, the Cr-Cr distances was found to be 6.8 Å, the S_N2 angle was found to be 163.5º, and the O-C bond forming distance was found to be 2.03 Å.

Conclusions

Isotactic poly (propylene oxide) (*i*PPO) is a desirable material due to its tensile strength and high glass transition temperature. It is not available due in part to the high cost to obtain enantiopure propylene oxide and the lack of catalysts that can isospecifically polymerize *rac*-propylene oxide. Development of an enantioselective catalyst will deliver two valuable products: *i*PPO and enantiopure epoxide, an advantageous synthetic building block.

This computational investigation modeled a promising but not yet fully optimized catalyst for obtaining *i*PPO. Using quantum chemical calculations, the molecular geometry of the catalyst was determined, and tunable stereocontrolling features were developed for probing the relationship between catalyst structure and activity. The Cr-Cr distance at the transition state was constant across all four investigated catalysts varying from 6.82 to 6.86 Å.

We found that modification of the structure to increase steric bulk at the ortho position lead to increased enantioselectivity at the cost of decreased activity. The decrease in overall reactivity is explained by the observation that increased steric bulk reduces the accessibility of the active site for monomer addition.

The capacity of our tunable features to predict and evaluate reactivity and selectivity will continue to prove useful for improved catalyst design and, ultimately, for the production of *i*PPO.

Chapter 5. Final Thoughts

Advancements in computing power and the development of new computational methods have positioned computational chemists to be able to provide key insights by being able to accurately and efficiently assess chemical mechanisms via quantum chemical simulations. As theoretical methods become more efficient, theoretical and experimental chemists can work together in real time providing insights and direction to each other, ultimately increasing the pace of chemical discovery. Advancements in automated reaction discovery methods are central to developing cost-effective tools to explore potential energy surfaces. The ability to efficiently probe the relevant chemical space has allowed computational chemists to begin to move from the role of experimental confirmation into the more essential role of guiding work being done in the laboratory.

Our efforts have focused on uncovering features of a chemical transformation that control its reactivity that are measurable and tunable. Examples of these features include geometric quantities (i.e. bond lengths, angles, and torsions), functional group electronegativity, molecular polarity, nucleophilicity or electrophilicity, size of functional group, ΔE_{rxn}, coordination number of reactive atoms, and metal center spin state. These added insights from simulation enhance chemical understanding of a system by establishing important structure-reactivity relationships which allow chemists to design more effective systems which exploit these newfound characteristics.

Research Summary

Chapter Two

The studies contained herein demonstrate the utility of reaction path exploration to investigate chemical reactivity. In chapter 2, mechanistic details of three diverse mechanochemical transformations are uncovered using a functionality developed for the Growing String Method (GSM) to study reactions under an external mechanical force. Mechanochemistry is an important, emerging branch of chemistry that encompasses a wide range of chemical transformations. Because mechanically enhanced reactions can permit otherwise disallowed or unfavorable reactions, it is vital that principles governing these new reactivities are probed. The use of single-ended GSM proved invaluable in the identification of transition states and products for reactions that do not easily fit into the scope of well-established chemical intuition. The ability to elucidate the details of these complex reactions was demonstrated, in finding the *cis* and *trans* isomers of the spiropyran to merocyanin transformation under the application of varying magnitudes of force, the fundamental means of flex-activation of mechanophores, and revealing the physical principles of force transmittance through different polymer backbones. First principles simulation's capacity for discovering reaction mechanisms under force will continue to prove useful for developing improved mechanochemical reactions, mechanophores, and ultimately, advanced functional materials.

Chapter Three

In chapter 3, the first mechanistic study of the metal-free ring-opening metathesis polymerization (ROMP) process is reported. We have demonstrated the ability of the metal-free ROMP system to polymerize norbornene monomers into PNB with varying degrees of

stereoselectivity which can be modulated by various parameters including counter anion size, temperature, solvent, and donating ability of the R-group on the initiator. Using experimental and computational insights, a model was developed to explain the pattern of stereoselectivity exhibited in this metal-free redox-mediated system. When small anions or polar solvents are used, the carbocation is stabilized, and product ratios lean more heavily toward *trans* product. Destabilizing the cation by using a larger anion or nonpolar solvents leads to product with higher *cis* product. A series of substituted initiators were evaluated in the ROMP of norbornene monomers. Highly *trans* polymers were generated as the steric size of the R-group increased. A stereoelectronic effect was reported in which larger R-groups sterically destabilized the cation by distorting the geometry and preventing π interaction while the larger R-groups electronically stabilized the cation by their increased donating ability. The data from both experiment and computation indicate that the *trans* products are thermodynamically favored under most reaction conditions, but product content can be shifted toward the *cis* product when the carbocation is sufficiently destabilized.

The mechanistic insights gained in this study will not only aid in the development of new metal-free catalysts, but also provide increased predictive power in polymerizations mediated by these systems. Ability to have a high level of precision in tuning of the polymer's product content allows for an unprecedented level of control over PNB microstructure. Insights gained in the studies presented in this chapter will provide a platform for the development of new metal-free systems capable of producing interesting and varied architectures via ring-opening metathesis polymerization.

Chapter Four

The mechanistic investigation described in chapter 4 modeled a promising but not yet fully optimized catalyst for obtaining *isotactic* poly (propylene oxide) (*i*PPO). Using quantum chemical calculations, the molecular geometry of the catalyst was determined, and tunable stereocontrolling features were developed for probing the relationship between catalyst structure and activity. Relevant features included S_N2 angle, metal-metal separation, and atomic distance between reactive atoms. Catalysts which had S_N2 angles closer to the preferred angle for S_N2-type transformations, $180°$, has lower activation barriers and were therefore found to be the more reactive catalysts. Metal-metal distances, reactive atom distances, and angle of kink in the salen ligand provided important steric information about the preferred conformation in the catalytic cleft. These principles can be used to design more efficient catalysts moving forward.

Additionally, in making substitutions on the catalyst, we found that modification of the structure to increase steric bulk at the ortho position lead to increased enantioselectivity at the cost of decreased activity. The decrease in overall reactivity is explained by the observation that increased steric bulk reduces the accessibility of the catalytic cleft for monomer addition. Exchanging the ^{t}Bu group for a methyl or chloro group at the para position lead to similar activity. The capacity of our tunable features to predict and evaluate catalytic reactivity and selectivity will continue to prove useful for improved catalyst design and, ultimately, for more efficient production of *i*PPO.

Open Questions and Future Considerations

Although the included studies have made significant contributions to a better understanding of polymer mechanochemistry and two unique polymerization methods, many questions and open pathways for research remain.

Chapter Two

Much is still unknown about the emerging area of mechanochemistry. GSM has proven to be a valuable tool for uncovering the unexpected chemistries that are a result of the force induced deformations to the potential energy surface (PES). In order to begin to uncover the relationships between various moieties and PES deformations, extensive exploration of mechanically biased PESs must be performed. By creating analogs of mechanophores which have been substituted with moieties that modulate steric and electronic properties and understanding how each biases the PES, we can begin to predict mechanophore reactivity more reliably and design mechanophore scaffolds that activate under desired conditions.

Chapter Three

Though the metal-free ROMP process has been able to be optimized to yield highly *trans* polymers, it is the *cis* product that is of more commercial value. Moving forward, experiments and computations are being designed to probe and further understand the stereoelectronic dependence of the product content ratios. In order to synthesize highly *cis* ROMP polymers, initiators substituted with groups that destabilize the carbocation will be utilized. Additionally, steric substitutions on the monomer which prevent close coordination and stabilizing interactions from a counter anion will be explored.

Chapter Four

The simulations models reported within chapter four provide valuable insight into the mechanistic details of enantioselective propylene oxide polymerization by a bimetallic chromium catalyst. Though these will be valuable in proposing new structures for the catalytic scaffold, moving forward, so far, we have been unable to develop a catalyst that performed better than the *t*Bu catalyst in terms of both activity and enantioselectivity. We have demonstrated that an increase in selectivity may be obtained by exchanging for large non-rotatable groups at the ortho position such as seen with adamantyl. Increasing activity while maintaining high selectivity, however, may prove to be challenging as the increased selectivity comes from reducing the size of the catalytic cleft which appears to be directly responsible for diminished activity. Future work will focus on making substitutions at other positions on the catalyst such as on the alkyl linker in order to more strongly force enantiomorphic site control in the catalytic cleft.

Final Remarks

I hope that these principles will enable real progress in theoretical materials research. The studies contained within this work demonstrate the ability of computational reaction exploration methods to inform experiment and enhance chemical understanding. Accurate chemical models can be used to uncover insightful structure-activity or structure-selectivity relationships by measuring meaningful chemical descriptors. These insights allow experimentalists to learn from the model and tune the features of the reaction that have been demonstrated to control chemical reactivity and selectivity.

Bibliography

(1)   Sperger, T.; Sanhueza, I. A.; Schoenebeck, F. Computation and Experiment: A Powerful Combination to Understand and Predict Reactivities. *Acc. Chem. Res.* **2016**, *49* (6), 1311–1319. https://doi.org/10.1021/acs.accounts.6b00068.

(2)   Jackson, K.; Jaffar, S. K.; Paton, R. S. Computational Organic Chemistry. *Annu. Reports Prog. Chem. - Sect. B* **2013**, *109*, 235–255. https://doi.org/10.1039/c3oc90007j.

(3)   Raghavachari, K.; Trucks, G. W.; Pople, J. A.; Head-gordon, M. Krishnan RAGHAVACHARI, Gary W. TRUCKS. *Chem. Phys. Lett.* **1989**, *157* (6), 479–483.

(4)   Deegan, M. J. O.; Knowles, P. J. Perturbative Corrections to Account for Triple Excitations in Closed and Open Shell Coupled Cluster Theories. *Chem. Phys. Lett.* **1994**, *227* (3), 321–326. https://doi.org/10.1016/0009-2614(94)00815-9.

(5)   Sousa, S. F.; Ribeiro, A. J. M.; Neves, R. P. P.; Brás, N. F.; Cerqueira, N. M. F. S. A.; Fernandes, P. A.; Ramos, M. J. Application of Quantum Mechanics/Molecular Mechanics Methods in the Study of Enzymatic Reaction Mechanisms. *Wiley Interdiscip. Rev. Comput. Mol. Sci.* **2017**, *7* (2). https://doi.org/10.1002/wcms.1281.

(6)   Bretonnet, J. L. Basics of the Density Functional Theory. *AIMS Mater. Sci.* **2017**, *4* (6), 1372–1405. https://doi.org/10.3934/MATERSCI.2017.6.1372.

(7)   Cramer, C. J.; Truhlar, D. G. Density Functional Theory for Transition Metals and Transition Metal Chemistry. *Phys. Chem. Chem. Phys.* **2009**, *11* (46), 10757–10816. https://doi.org/10.1039/b907148b.

(8)   Neese, F. Prediction of Molecular Properties and Molecular Spectroscopy with Density Functional Theory: From Fundamental Theory to Exchange-Coupling. *Coord. Chem. Rev.* **2009**, *253* (5–6), 526–563. https://doi.org/10.1016/j.ccr.2008.05.014.

(9)   Tsipis, A. C. DFT Flavor of Coordination Chemistry. *Coord. Chem. Rev.* **2014**, *272*, 1–29. https://doi.org/10.1016/j.ccr.2014.02.023.

(10)   Nguyen, Q. N. N.; Tantillo, D. J. The Many Roles of Quantum Chemical Predictions in Synthetic Organic Chemistry. *Chem. - An Asian J.* **2014**, *9* (3), 674–680. https://doi.org/10.1002/asia.201301452.

(11)   Niu, S.; Hall, M. B. Theoretical Studies on Reactions of Transition-Metal Complexes. *Chem. Rev.* **2000**, *100* (2), 353–405. https://doi.org/10.1021/cr980404y.

(12)   Childers, M. I.; Vitek, A. K.; Morris, L. S.; Widger, P. C. B.; Ahmed, S. M.; Zimmerman,

P. M.; Coates, G. W. Isospecific, Chain Shuttling Polymerization of Propylene Oxide Using a Bimetallic Chromium Catalyst: A New Route to Semicrystalline Polyols. *J. Am. Chem. Soc.* **2017**, *139* (32), 11048–11054. https://doi.org/10.1021/jacs.7b00194.

(13)   Harvey, J. N. On the Accuracy of Density Functional Theory in Transition Metal Chemistry. *Annu. Reports Prog. Chem. - Sect. C* **2006**, *102* (1), 203–226. https://doi.org/10.1039/b419105f.

(14)   Feng, X.; Gu, J.; Xie, Y.; King, R. B.; Schaefer, H. F. Homoleptic Carbonyls of the Second-Row Transition Metals: Evaluation of Hartree-Fock and Density Functional Theory Methods. *J. Chem. Theory Comput.* **2007**, *3* (4), 1580–1587. https://doi.org/10.1021/ct7000254.

(15)   Tirado-Rives, J.; Jorgensen, W. L. Performance of B3LYP Density Functional Methods for a Large Set of Organic Molecules. *J. Chem. Theory Comput.* **2008**, *4* (2), 297–306. https://doi.org/10.1021/ct700248k.

(16)   Silva-Junior, M. R.; Schreiber, M.; Sauer, S. P. A.; Thiel, W. Benchmarks for Electronically Excited States: Time-Dependent Density Functional Theory and Density Functional Theory Based Multireference Configuration Interaction. *J. Chem. Phys.* **2008**, *129* (10). https://doi.org/10.1063/1.2973541.

(17)   Dreuw, A.; Head-Gordon, M. Failure of Time-Dependent Density Functional Theory for Long-Range Charge-Transfer Excited States: The Zincbacteriochlorin-Bacteriochlorin and Bacteriochlorophyll-Spheroidene Complexes. *J. Am. Chem. Soc.* **2004**, *126* (12), 4007–4016. https://doi.org/10.1021/ja039556n.

(18)   Stein, T.; Kronik, L.; Baer, R. Reliable Prediction of Charge Transfer Excitations in Molecular Complexesusing Time-Dependent Density Functional Theory. *J. Am. Chem. Soc.* **2009**, *131* (8), 2818–2820. https://doi.org/10.1021/ja8087482.

(19)   Risthaus, T.; Grimme, S. Benchmarking of London Dispersion-Accounting Density Functional Theory Methods on Very Large Molecular Complexes. *J. Chem. Theory Comput.* **2013**, *9* (3), 1580–1591. https://doi.org/10.1021/ct301081n.

(20)   Schwabe, T.; Grimme, S. Theoretical Thermodynamics for Large Molecules: Walking the Thin Line between Accuracy and Computational Cost. *Acc. Chem. Res.* **2008**, *41* (4), 569–579. https://doi.org/10.1021/ar700208h.

(21)   Klimeš, J.; Michaelides, A. Perspective: Advances and Challenges in Treating van Der Waals Dispersion Forces in Density Functional Theory. *J. Chem. Phys.* **2012**, *137* (12). https://doi.org/10.1063/1.4754130.

(22)   Chai, J. Da; Head-Gordon, M. Systematic Optimization of Long-Range Corrected Hybrid Density Functionals. *J. Chem. Phys.* **2008**, *128* (8). https://doi.org/10.1063/1.2834918.

(23)   Chai, J. Da; Head-Gordon, M. Long-Range Corrected Hybrid Density Functionals with Damped Atom-Atom Dispersion Corrections. *Phys. Chem. Chem. Phys.* **2008**, *10* (44),

6615–6620. https://doi.org/10.1039/b810189b.

(24)   Bühl, M.; Kabrede, H. Geometries of Transition-Metal Complexes from Density-Functional Theory. *J. Chem. Theory Comput.* **2006**, *2* (5), 1282–1290. https://doi.org/10.1021/ct6001187.

(25)   Minenkov, Y.; Singstad, Å.; Occhipinti, G.; Jensen, V. R. The Accuracy of DFT-Optimized Geometries of Functional Transition Metal Compounds: A Validation Study of Catalysts for Olefin Metathesis and Other Reactions in the Homogeneous Phase. *Dalt. Trans.* **2012**, *41* (18), 5526–5541. https://doi.org/10.1039/c2dt12232d.

(26)   Wei, Z.; Ning, N.; Zhang, L.; Tian, M.; Mi, J. Density Functional Theory of Polymer Structure and Conformations. *Polymers (Basel).* **2016**, *8* (4). https://doi.org/10.3390/polym8040121.

(27)   McGarrigle, E. M.; Gilheany, D. G. *Chromium-and Manganese-Salen Promoted Epoxidation of Alkenes*; 2005; Vol. 105. https://doi.org/10.1021/cr0306945.

(28)   Blankenburg, J.; Kersten, E.; Maciol, K.; Wagner, M.; Zarbakhsh, S.; Frey, H. The Poly(Propylene Oxide-: Co -Ethylene Oxide) Gradient Is Controlled by the Polymerization Method: Determination of Reactivity Ratios by Direct Comparison of Different Copolymerization Models. *Polym. Chem.* **2019**, *10* (22), 2863–2871. https://doi.org/10.1039/c9py00500e.

(29)   Simón, L.; Goodman, J. M. How Reliable Are DFT Transition Structures? Comparison of GGA, Hybrid-Meta-GGA and Meta-GGA Functionals. *Org. Biomol. Chem.* **2011**, *9* (3), 689–700. https://doi.org/10.1039/c0ob00477d.

(30)   Bell, A. T.; Head-Gordon, M. Quantum Mechanical Modeling of Catalytic Processes. *Annu. Rev. Chem. Biomol. Eng.* **2011**, *2* (1), 453–477. https://doi.org/10.1146/annurev-chembioeng-061010-114108.

(31)   Mardirossian, N.; Head-Gordon, M. Thirty Years of Density Functional Theory in Computational Chemistry: An Overview and Extensive Assessment of 200 Density Functionals. *Mol. Phys.* **2017**, *115* (19), 2315–2372. https://doi.org/10.1080/00268976.2017.1333644.

(32)   Marcelli, T. Organocatalysis: Cinchona Catalysts. *Wiley Interdiscip. Rev. Comput. Mol. Sci.* **2011**, *1* (1), 142–152. https://doi.org/10.1002/wcms.2.

(33)   Cohen, A. J.; Mori-Sánchez, P.; Yang, W. Insights into Current Limitations of Density Functional Theory. *Science (80-.).* **2008**, *321* (5890), 792–794. https://doi.org/10.1126/science.1158722.

(34)   Karton, A.; Tarnopolsky, A.; Lamère, J. F.; Schatz, G. C.; Martin, J. M. L. Highly Accurate First-Principles Benchmark Data Sets for the Parametrization and Validation of Density Functional and Other Approximate Methods. Derivation of a Robust, Generally Applicable, Double-Hybrid Functional for Thermochemistry and Thermochemical . *J.*

Phys. Chem. A **2008**, *112* (50), 12868–12886. https://doi.org/10.1021/jp801805p.

(35)   Hu, L.; Chen, H. Assessment of DFT Methods for Computing Activation Energies of Mo/W-Mediated Reactions. *J. Chem. Theory Comput.* **2015**, *11* (10), 4601–4614. https://doi.org/10.1021/acs.jctc.5b00373.

(36)   Quintal, M. M.; Karton, A.; Iron, M. A.; Daniel Boese, A.; Martin, J. M. L. Benchmark Study of DFT Functionals for Late-Transition-Metal Reactions. *J. Phys. Chem. A* **2006**, *110* (2), 709–716. https://doi.org/10.1021/jp054449w.

(37)   Zhao, Y.; Truhlar, D. G. Benchmark Energetic Data in a Model System for Grubbs II Metathesis Catalysis and Their Use for the Development, Assessment, and Validation of Electronic Structure Methods. *J. Chem. Theory Comput.* **2009**, *5* (2), 324–333. https://doi.org/10.1021/ct800386d.

(38)   Weymuth, T.; Couzijn, E. P. A.; Chen, P.; Reiher, M. New Benchmark Set of Transition-Metal Coordination Reactions for the Assessment of Density Functionals. *J. Chem. Theory Comput.* **2014**, *10* (8), 3092–3103. https://doi.org/10.1021/ct500248h.

(39)   Seth, M.; Ziegler, T.; Steinmetz, M.; Grimme, S. Modeling Transition Metal Reactions with Range-Separated Functionals. *J. Chem. Theory Comput.* **2013**, *9* (5), 2286–2299. https://doi.org/10.1021/ct301112m.

(40)   Halgren, T. A.; Lipscomb, W. N. The Synchronous-Transit Method for Determining Reaction Pathways and Locating Molecular Transition States. *Chem. Phys. Lett.* **1977**, *49* (2), 225–232. https://doi.org/10.1016/0009-2614(77)80574-5.

(41)   Müller, K.; Brown, L. D. Location of Saddle Points and Minimum Energy Paths by a Constrained Simplex Optimization Procedure. *Theor. Chim. Acta* **1979**, *53* (1), 75–93. https://doi.org/10.1007/BF00547608.

(42)   Dewar, M. J. S.; Healy, E. F.; Stewart, J. J. P. Location of Transition States in Reaction Mechanisms. *J. Chem. Soc. Faraday Trans. 2 Mol. Chem. Phys.* **1984**, *80* (3), 227–233. https://doi.org/10.1039/F29848000227.

(43)   Ionova, I. V.; Carter, E. A. Ridge Method for Finding Saddle Points on Potential Energy Surfaces. *J. Chem. Phys.* **1993**, *98* (8), 6377–6386. https://doi.org/10.1063/1.465100.

(44)   Cerjan, C. J.; Miller, W. H. On Finding Transition States. *J. Chem. Phys.* **1981**, *75* (6), 2800–2806. https://doi.org/10.1063/1.442352.

(45)   Henkelman, G.; Jónsson, H. A Dimer Method for Finding Saddle Points on High Dimensional Potential Surfaces Using Only First Derivatives. *J. Chem. Phys.* **1999**, *111* (15), 7010–7022. https://doi.org/10.1063/1.480097.

(46)   Trygubenko, S. A.; Wales, D. J. A Doubly Nudged Elastic Band Method for Finding Transition States. *J. Chem. Phys.* **2004**, *120* (5), 2082–2094. https://doi.org/10.1063/1.1636455.

(47)   Henkelman, G.; Uberuaga, B. P.; Jónsson, H. Climbing Image Nudged Elastic Band
        Method for Finding Saddle Points and Minimum Energy Paths. *J. Chem. Phys.* **2000**, *113*
        (22), 9901–9904. https://doi.org/10.1063/1.1329672.

(48)   Henkelman, G.; Jónsson, H. Improved Tangent Estimate in the Nudged Elastic Band
        Method for Finding Minimum Energy Paths and Saddle Points. *J. Chem. Phys.* **2000**, *113*
        (22), 9978–9985. https://doi.org/10.1063/1.1323224.

(49)   Maragakis, P.; Andreev, S. A.; Brumer, Y.; Reichman, D. R.; Kaxiras, E. Adaptive
        Nudged Elastic Band Approach for Transition State Calculation. *J. Chem. Phys.* **2002**, *117*
        (10), 4651–4658. https://doi.org/10.1063/1.1495401.

(50)   Zimmerman, P. Reliable Transition State Searches Integrated with the Growing String
        Method. *J. Chem. Theory Comput.* **2013**, *9* (7), 3043–3050.
        https://doi.org/10.1021/ct400319w.

(51)   Zimmerman, P. M. Growing String Method with Interpolation and Optimization in
        Internal Coordinates: Method and Examples. *J. Chem. Phys.* **2013**, *138* (18).
        https://doi.org/10.1063/1.4804162.

(52)   Petersandreas, B.; Bellarup, H. T.; Peters, B.; Heyden, A.; Bell, A. T. A Growing String
        Method for Determining Transition States : Comparison to the Nudged Elastic Band and
        String Methods A Growing String Method for Determining Transition States :
        Comparison to the Nudged Elastic Band and String Methods. **2004**, *7877*.
        https://doi.org/10.1063/1.1691018.

(53)   E, W.; Ren, W.; Vanden-Eijnden, E. Finite Temperature String Method for the Study of
        Rare Events. *J. Phys. Chem. B* **2005**, *109* (14), 6688–6693.
        https://doi.org/10.1021/jp0455430.

(54)   E, W.; Ren, W.; Vanden-Eijnden, E. String Method for the Study of Rare Events. *Phys.
        Rev. B - Condens. Matter Mater. Phys.* **2002**, *66* (5), 523011–523014.
        https://doi.org/10.1103/PhysRevB.66.052301.

(55)   Zimmerman, P. M. Single-Ended Transition State Finding with the Growing String
        Method. *J. Comput. Chem.* **2015**, *36* (9), 601–611. https://doi.org/10.1002/jcc.23833.

(56)   Aldaz, C.; Kammeraad, J. A.; Zimmerman, P. M. Discovery of Conical Intersection
        Mediated Photochemistry with Growing String Methods. *Phys. Chem. Chem. Phys.* **2018**,
        20 (43), 27394–27405. https://doi.org/10.1039/c8cp04703k.

(57)   Jafari, M.; Zimmerman, P. M. Reliable and Efficient Reaction Path and Transition State
        Finding for Surface Reactions with the Growing String Method. **2017**, 645–658.
        https://doi.org/10.1002/jcc.24720.

(58)   Jafari, M.; Zimmerman, P. M. Uncovering Reaction Sequences on Surfaces through
        Graphical Methods. *Phys. Chem. Chem. Phys.* **2018**, *20* (11), 7721–7729.
        https://doi.org/10.1039/c8cp00044a.

(59)   Roessler, A. G.; Zimmerman, P. M. Examining the Ways to Bend and Break Reaction
       Pathways Using Mechanochemistry. *J. Phys. Chem. C* **2018**, *122* (12).
       https://doi.org/10.1021/acs.jpcc.8b00467.

(60)   Larsen, M. B.; Boydston, A. J. "Flex-Activated" Mechanophores: Using Polymer
       Mechanochemistry to Direct Bond Bending Activation. *J. Am. Chem. Soc.* **2013**, *135* (22),
       8189–8192. https://doi.org/10.1021/ja403757p.

(61)   Larsen, M. B.; Boydston, A. J. Successive Mechanochemical Activation and Small
       Molecule Release in an Elastomeric Material. *J. Am. Chem. Soc.* **2014**, *136* (4), 1276–
       1279. https://doi.org/10.1021/ja411891x.

(62)   Klukovich, H. M.; Kouznetsova, T. B.; Kean, Z. S.; Lenhardt, J. M.; Craig, S. L. A
       Backbone Lever-Arm Effect Enhances Polymer Mechanochemistry. *Nat. Chem.* **2013**, *5*
       (2), 110–114. https://doi.org/10.1038/nchem.1540.

(63)   Ogawa, K. A.; Goetz, A. E.; Boydston, A. J. Metal-Free Ring-Opening Metathesis
       Polymerization. *J. Am. Chem. Soc.* **2015**, *137* (4), 1400–1403.
       https://doi.org/10.1021/ja512073m.

(64)   Caruso, M. M.; Davis, D. A.; Shen, Q.; Odom, S. A.; Sottos, N. R.; White, S. R.; Moore,
       J. S. Mechanically-Induced Chemical Changes in Polymeric Materials. *Chem. Rev.* **2009**,
       109 (11), 5755–5798. https://doi.org/10.1021/cr9001353.

(65)   Beyer, M. K.; Clausen-Schaumann, H. Mechanochemistry: The Mechanical Activation of
       Covalent Bonds. *Chem. Rev.* **2005**, *105* (8), 2921–2948.
       https://doi.org/10.1021/cr030697h.

(66)   May, P. A.; Moore, J. S. Polymer Mechanochemistry: Techniques to Generate Molecular
       Force via Elongational Flows. *Chem. Soc. Rev.* **2013**, *42*, 7497–7506.
       https://doi.org/10.1039/c2cs35463b.

(67)   Li, J.; Nagamani, C.; Moore, J. S. Polymer Mechanochemistry: From Destructive to
       Productive. *Acc. Chem. Res.* **2015**, *48* (8), 2181–2190.
       https://doi.org/10.1021/acs.accounts.5b00184.

(68)   Brantley, J. N.; Wiggins, K. M.; Bielawski, C. W. Polymer Mechanochemistry: The
       Design and Study of Mechanophores. *Polym. Int.* **2013**, *62* (1), 2–12.
       https://doi.org/10.1002/pi.4350.

(69)   Black, A. L.; Lenhardt, J. M.; Craig, S. L. From Molecular Mechanochemistry to Stress-
       Responsive Materials. *J. Mater. Chem.* **2011**, *21* (6), 1655–1663.
       https://doi.org/10.1039/c0jm02636k.

(70)   Ong, M. T.; Leiding, J.; Tao, H.; Virshup, A. M.; Martínez, T. J. First Principles
       Dynamics and Minimum Energy Pathways for Mechanochemical Ring Opening of
       Cyclobutene. *J. Am. Chem. Soc.* **2009**, *131* (18), 6377–6379.
       https://doi.org/10.1021/ja8095834.

(71) Hickenboth, C. R.; Moore, J. S.; White, S. R.; Sottos, N. R.; Baudry, J.; Wilson, S. R. Biasing Reaction Pathways with Mechanical Force. *Nature* **2007**, *446* (7134), 423–427. https://doi.org/10.1038/nature05681.

(72) Potisek, S. L.; Davis, D. A.; Sottos, N. R.; White, S. R.; Moore, J. S. Mechanophore-Linked Addition Polymers. *J. Am. Chem. Soc.* **2007**, *129* (45), 13808–13809. https://doi.org/10.1021/ja076189x.

(73) Granick, S.; Bae, S. C. Stressed Molecules Break Down. *Nature* **2006**, *440* (March), 160–161. https://doi.org/10.1038/440160a.

(74) Berkowski, K. L.; Potisek, S. L.; Hickenboth, C. R.; Moore, J. S. Ultrasound-Induced Site-Specific Cleavage of Azo-Functionalized Poly(Ethylene Glycol). *Macromolecules* **2005**, *38* (22), 8975–8978. https://doi.org/10.1021/ma051394n.

(75) Todres, Z. V. Recent Advances in the Study of Mechanochromic Transitions of Organic Compounds. *J. Chem. Res.* **2004**, *2004* (2), 89–93. https://doi.org/10.3184/030823404323000332.

(76) Davis, D. a; Hamilton, A.; Yang, J.; Cremar, L. D.; Van Gough, D.; Potisek, S. L.; Ong, M. T.; Braun, P. V; Martínez, T. J.; White, S. R.; et al. Force-Induced Activation of Covalent Bonds in Mechanoresponsive Polymeric Materials. *Nature* **2009**, *459* (7243), 68–72. https://doi.org/10.1038/nature07970.

(77) Zhang, H.; Gao, F.; Cao, X.; Li, Y.; Xu, Y.; Weng, W.; Boulatov, R. Mechanochromism and Mechanical-Force-Triggered Cross-Linking from a Single Reactive Moiety Incorporated into Polymer Chains. *Angew. Chemie - Int. Ed.* **2016**, *55* (9), 3040–3044. https://doi.org/10.1002/anie.201510171.

(78) Sohma, J. Mechanochemistry of Polymers. *Prog. Polym. Sci.* **1989**, *14* (4), 451–596. https://doi.org/10.1016/0079-6700(89)90004-X.

(79) Chen, X.; Dam, M. A.; Ono, K.; Mal, A.; Shen, H.; Nutt, S. R.; Sheran, K.; Wudl, F. A Thermally Re-Mendable Cross-Linked Polymeric Material. *Science* **2002**, *295* (5560), 1698–1702. https://doi.org/10.1126/science.1065879.

(80) Cordier, P.; Tournilhac, F.; Soulié-Ziakovic, C.; Leibler, L. Self-Healing and Thermoreversible Rubber from Supramolecular Assembly. *Nature* **2008**, *451* (7181), 977–980. https://doi.org/10.1038/nature06669.

(81) Reutenauer, P.; Buhler, E.; Boul, P. J.; Candau, S. J.; Lehn, J. M. Room Temperature Dynamic Polymers Based on Diels-Alder Chemistry. *Chem. - A Eur. J.* **2009**, *15* (8), 1893–1900. https://doi.org/10.1002/chem.200802145.

(82) Gossweiler, G. R.; Hewage, G. B.; Soriano, G.; Wang, Q.; Welshofer, G. W.; Zhao, X.; Craig, S. L. Mechanochemical Activation of Covalent Bonds in Polymers with Full and Repeatable Macroscopic Shape Recovery. *ACS Macro Lett.* **2014**, *3* (3), 216–219. https://doi.org/10.1021/mz500031q.

(83)   Diesendruck, C. E.; Steinberg, B. D.; Sugai, N.; Silberstein, M. N.; Sottos, N. R.; White, S. R.; Braun, P. V.; Moore, J. S. Proton-Coupled Mechanochemical Transduction: A Mechanogenerated Acid. *J. Am. Chem. Soc.* **2012**, *134* (30), 12446–12449. https://doi.org/10.1021/ja305645x.

(84)   Nagamani, C.; Liu, H.; Moore, J. S. Mechanogeneration of Acid from Oxime Sulfonates. *J. Am. Chem. Soc.* **2016**, *138* (8), 2540–2543. https://doi.org/10.1021/jacs.6b00097.

(85)   Gossweiler, G. R.; Kouznetsova, T. B.; Craig, S. L. Force-Rate Characterization of Two Spiropyran-Based Molecular Force Probes. *J. Am. Chem. Soc.* **2015**, *137* (19), 6148–6151. https://doi.org/10.1021/jacs.5b02492.

(86)   Kim, T. A.; Beiermann, B. A.; White, S. R.; Sottos, N. R. Effect of Mechanical Stress on Spiropyran-Merocyanine Reaction Kinetics in a Thermoplastic Polymer. *ACS Macro Lett.* **2016**, *5*, 1312–1316. https://doi.org/10.1021/acsmacrolett.6b00822.

(87)   Brown, C. L.; Craig, S. L. Molecular Engineering of Mechanophore Activity for Stress-Responsive Polymeric Materials. *Chem. Sci.* **2015**, *6*, 2158–2165. https://doi.org/10.1039/C4SC01945H.

(88)   Konda, S. S. M.; Brantley, J. N.; Bielawski, C. W.; Makarov, D. E. Chemical Reactions Modulated by Mechanical Stress: Extended Bell Theory. *J. Chem. Phys.* **2011**, *135* (16). https://doi.org/10.1063/1.3656367.

(89)   Evans, E.; Ritchie, K. Dynamic Strength of Molecular Adhesion Bonds. *Biophys. J.* **1997**, *72* (4), 1541–1555. https://doi.org/10.1016/S0006-3495(97)78802-7.

(90)   Shao, Y.; Molnar, L. F.; Jung, Y.; Kussmann, J.; Ochsenfeld, C.; Brown, S. T.; Gilbert, A. T. B.; Slipchenko, L. V; Levchenko, S. V; O'Neill, D. P.; et al. Advances in Methods and Algorithms in a Modern Quantum Chemistry Program Package. *Phys. Chem. Chem. Phys.* **2006**, *8* (27), 3172–3191. https://doi.org/10.1039/b517914a.

(91)   Becke, A. D. Density-Functional Exchange-Energy Approximation with Correct Asymptotic Behavior. *Phys. Rev. A* **1988**, *38* (6), 3098–3100. https://doi.org/10.1103/PhysRevA.38.3098.

(92)   Lee, C.; Yang, W.; Parr, R. G. Development of the Colle-Salvetti Correlation-Energy Formula into a Functional of the Electron Density. *Phys. Rev. B* **1988**, *37* (2), 785–789. https://doi.org/10.1103/PhysRevB.37.785.

(93)   Becke, A. D. A New Mixing of Hartree–Fock and Local Density-Functional Theories. *J. Chem. Phys.* **1993**, *98* (2), 1372. https://doi.org/10.1063/1.464304.

(94)   Hariharan, P. C.; Pople, J. A. The Influence of Polarization Functions on Molecular Orbital Hydrogenation Energies. *Theor. Chim. Acta* **1973**, *28* (3), 213–222. https://doi.org/10.1007/BF00533485.

(95)   Shao, Y.; Gan, Z.; Epifanovsky, E.; Gilbert, A. T. B.; Wormit, M.; Kussmann, J.; Lange,

A. W.; Behn, A.; Deng, J.; Feng, X.; et al. Advances in Molecular Quantum Chemistry Contained in the Q-Chem 4 Program Package. *Mol. Phys.* **2015**, *113* (2), 184–215. https://doi.org/10.1080/00268976.2014.952696.

(96) Humphrey, W.; Dalke, A.; Schulten, K. VMD: Visual Molecular Dynamics. *J. Mol. Graph.* **1996**, *14* (1), 33–38. https://doi.org/10.1016/0263-7855(96)00018-5.

(97) Wang, J.; Kouznetsova, T. B.; Kean, Z. S.; Fan, L.; Mar, B. D.; Martínez, T. J.; Craig, S. L. A Remote Stereochemical Lever Arm Effect in Polymer Mechanochemistry. *J. Am. Chem. Soc.* **2014**, *136* (43), 15162–15165. https://doi.org/10.1021/ja509585g.

(98) Akbulatov, S.; Tian, Y.; Boulatov, R. Force − Reactivity Property of a Single Monomer Is Sufficient To Predict the Micromechanical Behavior of Its Polymer. *J. Am. Chem. Soc.* **2012**, *134*, 7620–7623.

(99) Rivero, D.; Valentini, A.; Fernández-González, M. Á.; Zapata, F.; García-Iriepa, C.; Sampedro, D.; Palmeiro, R.; Frutos, L. M. Mechanical Forces Alter Conical Intersections Topology. *J. Chem. Theory Comput.* **2015**, *11* (8), 3740–3745. https://doi.org/10.1021/acs.jctc.5b00375.

(100) Chen, Y.; Spiering, a. J. H.; Karthikeyan, S.; Peters, G. W. M.; Meijer, E. W.; Sijbesma, R. P. Mechanically Induced Chemiluminescence from Polymers Incorporating a 1,2-Dioxetane Unit in the Main Chain. *Nat. Chem.* **2012**, *4* (7), 559–562. https://doi.org/10.1038/nchem.1358.

(101) Haselwander, T. F. A.; Heitz, W.; Krügel, S. A.; Wendorff, J. H. Polynorbornene: Synthesis, Properties and Simulations. *Macromol. Chem. Phys.* **1996**, *197* (10), 3435–3453. https://doi.org/10.1002/macp.1996.021971029.

(102) Ensing, B.; De Vivo, M.; Liu, Z.; Moore, P.; Klein, M. L. Metadynamics as a Tool for Exploring Free Energy Landscapes of Chemical Reactions. *Acc. Chem. Res.* **2006**, *39* (2), 73–81. https://doi.org/10.1021/ar040198i.

(103) Patil, A. O.; Zushma, S.; Stibrany, R. T.; Rucker, S. P.; Wheeler, L. M. Vinyl-Type Polymerization of Norbornene by Nickel(II) Bisbenzimidazole Catalysts. *J. Polym. Sci. Part A Polym. Chem.* **2003**, *41* (13), 2095–2106. https://doi.org/10.1002/pola.10725.

(104) Ivin, K. J.; Mol, J. C. *Olefin Metathesis and Metathesis Polymerization*; Academic Press: San Diego, 1997.

(105) Schrock, R. R. Synthesis of Stereoregular Polymers through Ring-Opening Metathesis Polymerization. *Acc. Chem. Res.* **2014**, *47* (8), 2457–2466. https://doi.org/10.1021/ar500139s.

(106) Bielawski, C. W.; Grubbs, R. H. Living Ring-Opening Metathesis Polymerization. *Prog. Polym. Sci.* **2007**, *32* (1), 1–29. https://doi.org/10.1016/j.progpolymsci.2006.08.006.

(107) Rosebrugh, L. E.; Herbert, M. B.; Marx, V. M.; Keitz, B. K.; Grubbs, R. H. Highly Active

Ruthenium Metathesis Catalysts Exhibiting Unprecedented Activity and Z-Selectivity. *J. Am. Chem. Soc.* **2013**, *135* (4), 1276–1279. https://doi.org/10.1021/ja311916m.

(108) Jeong, H.; Kozera, D. J.; Schrock, R. R.; Smith, S. J.; Zhang, J.; Ren, N.; Hillmyer, M. A. Z - Selective Ring-Opening Metathesis Polymerization of 3 - Substituted Cyclooctenes by Monoaryloxide Pyrrolide Imido Alkylidene (MAP) Catalysts of Molybdenum and Tungsten. **2013**. https://doi.org/10.1021/om400583t.

(109) Forrest, W. P.; Axtell, J. C.; Schrock, R. R. Tungsten Oxo Alkylidene Complexes as Initiators for the Stereoregular Polymerization of 2,3-Dicarbomethoxynorbornadiene. *Organometallics* **2014**, *33* (9), 2313–2325. https://doi.org/10.1021/om5002364.

(110) Flook, M. M.; Ng, V. W. L.; Schrock, R. R. Synthesis of Cis,Syndiotactic ROMP Polymers Containing Alternating Enantiomers. *J. Am. Chem. Soc.* **2011**, *133* (6), 1784–1786. https://doi.org/10.1021/ja110949f.

(111) Rosebrugh, L. E.; Marx, V. M.; Keitz, B. K.; Grubbs, R. H. Synthesis of Highly Cis, Syndiotactic Polymers via Ring-Opening Metathesis Polymerization Using Ruthenium Metathesis Catalysts. *J. Am. Chem. Soc.* **2013**, *135* (27), 10032–10035. https://doi.org/10.1021/ja405559y.

(112) Lee, L.-B. W.; Register, R. A. Hydrogenated Ring-Opened Polynorbornene: A Highly Crystalline Atactic Polymer. *Macromolecules* **2005**, *38* (4), 1216–1222. https://doi.org/10.1021/ma048013a.

(113) Schrock, R. R. Synthesis of Stereoregular ROMP Polymers Using Molybdenum and Tungsten Imido Alkylidene Initiators. *Dalt. Trans.* **2011**, *40* (29), 7484–7495. https://doi.org/10.1039/c1dt10215j.

(114) Hyvl, J.; Autenrieth, B.; Schrock, R. R. Proof of Tacticity of Stereoregular ROMP Polymers through Post Polymerization Modification. *Macromolecules* **2015**, *48* (9), 3148–3152. https://doi.org/10.1021/acs.macromol.5b00477.

(115) Coates, G. W. Precise Control of Polyolefin Stereochemistry Using Single-Site Metal Catalysts. *Chem. Rev.* **2000**, *100* (4), 1223–1252. https://doi.org/10.1021/cr990286u.

(116) Forrest, W. P.; Weis, J. G.; John, J. M.; Axtell, J. C.; Simpson, J. H.; Swager, T. M.; Schrock, R. R. Stereospecific Ring-Opening Metathesis Polymerization of Norbornadienes Employing Tungsten Oxo Alkylidene Initiators. *J. Am. Chem. Soc.* **2014**, *136* (31), 10910–10913. https://doi.org/10.1021/ja506446n.

(117) Schrock, R. R. Recent Advances in High Oxidation State Mo and W Imido Alkylidene Chemistry. *Chem. Rev.* **2009**, *109* (8), 3211–3226. https://doi.org/10.1021/cr800502p.

(118) Vougioukalakis, G. C.; Grubbs, R. H. Ruthenium-Based Heterocyclic Carbene-Coordinated Olefin Metathesis Catalysts. *Chem. Rev.* **2010**, *110* (3), 1746–1787. https://doi.org/10.1021/cr9002424.

(119) Amir-Ebrahimi, V.; Hamilton, J. G.; Rooney, J. J. Blockiness and Tacticity in Ring-Opened Metathesis Polymers. In *Ring Opening Metathesis Polymerisation and Related Chemistry. NATO Science Series (Series II: Mathematics, Physics and Chemistry)*; Khosravi, E., Szymanska-Buzar, T., Eds.; Springer, Dordrecht, 2002. https://doi.org/https://doi.org/10.1007/978-94-010-0373-5_4.

(120) Vougioukalakis, G. C. Removing Ruthenium Residues from Olefin Metathesis Reaction Products. *Chem. - A Eur. J.* **2012**, *18* (29), 8868–8880. https://doi.org/10.1002/chem.201200600.

(121) Rassolov, V. A.; Pople, J. A.; Ratner, M. A.; Windus, T. L. 6-31G* Basis Set for Atoms K through Zn. *J. Chem. Phys.* **1998**, *109* (4), 1223–1229. https://doi.org/10.1063/1.476673.

(122) Marenich, A. V.; Cramer, C. J.; Truhlar, D. G. Universal Solvation Model Based on Solute Electron Density and on a Continuum Model of the Solvent Defined by the Bulk Dielectric Constant and Atomic Surface Tensions. *J. Phys. Chem. B* **2009**, *113* (18), 6378–6396. https://doi.org/10.1021/jp810292n.

(123) Neese, F. Software Update: The ORCA Program System, Version 4.0. *Wiley Interdiscip. Rev. Comput. Mol. Sci.* **2018**, *8* (1), 4–9. https://doi.org/10.1002/wcms.1327.

(124) Charton, M. The Upsilon Steric Parameter — Definition and Determination. *Steric Eff. Drug Des.* **2007**, 57–91. https://doi.org/10.1007/bfb0111213.

(125) Miller, J. J.; Sigman, M. S. Quantitatively Correlating the Effect of Ligand-Substituent Size in Asymmetric Catalysis Using Linear Free Energy Relationships. *Angew. Chemie - Int. Ed.* **2008**, *47* (4), 771–774. https://doi.org/10.1002/anie.200704257.

(126) Von Matt, P.; Pfaltz, A. Chiral Phosphinoaryldihydrooxazoles as Ligands in Asymmetric Catalysis: Pd-Catalyzed Allylic Substitution. *Angew. Chemie - Int. Ed.* **1993**, *32* (4), 566–568.

(127) Denmark, S. E.; Christenson, B. L.; O'Connor, S. P. Catalytic Enantioselective Cyclopropanation with Bis(Halomethyl)Zinc Reagents. II. The Effect of Promoter Structure on Selectivity. *Tetrahedron Lett.* **1995**, *36* (13), 2219–2222. https://doi.org/10.1016/0040-4039(95)00259-F.

(128) Minakata, S.; Ando, T.; Nishimura, M.; Ryu, I.; Komatsu, M. Novel Asymmetric and Stereospecific Aziridination of Alkenes with a Chiral Nitridomanganese Complex. *Angew. Chemie - Int. Ed.* **1999**, *37* (24), 3392–3394. https://doi.org/10.1002/(SICI)1521-3773(19981231)37:24<3392::AID-ANIE3392>3.0.CO;2-G.

(129) Park, J.; Quan, Z.; Lee, S.; Ahn, K. H.; Cho, C. W. Synthesis of Chiral 1′-Substituted Oxazolinylferrocenes as Chiral Ligands for Pd-Catalyzed Allylic Substitution Reactions. *J. Organomet. Chem.* **1999**, *584* (1), 140–146. https://doi.org/10.1016/S0022-328X(99)00125-4.

(130) Wu, H. L.; Uang, B. J. Asymmetric Epoxidation of Allylic Alcohols Catalyzed by New

Chiral Vanadium(V) Complexes. *Tetrahedron Asymmetry* **2002**, *13* (24), 2625–2628. https://doi.org/10.1016/S0957-4166(02)00741-3.

(131) Quintard, A.; Alexakis, A. 1,2-Sulfone Rearrangement in Organocatalytic Reactions. *Org. Biomol. Chem.* **2011**, *9* (5), 1407–1418. https://doi.org/10.1039/c0ob00818d.

(132) Zahrt, A. F.; Athavale, S. V.; Denmark, S. E. Quantitative Structure-Selectivity Relationships in Enantioselective Catalysis: Past, Present, and Future. *Chem. Rev.* **2020**, *120* (3), 1620–1689. https://doi.org/10.1021/acs.chemrev.9b00425.

(133) Ess, D. H.; Houk, K. N. Distortion/Interaction Energy Control of 1,3-Dipolar Cycloaddition Reactivity. *J. Am. Chem. Soc.* **2007**, *129* (35), 10646–10647. https://doi.org/10.1021/ja0734086.

(134) Ess, D. H.; Houk, K. N. Theory of 1,3-Dipolar Cycloadditions: Distortion/Interaction and Frontier Molecular Orbital Models. *J. Am. Chem. Soc.* **2008**, *130* (31), 10187–10198. https://doi.org/10.1021/ja800009z.

(135) Bickelhaupt, F. M.; Houk, K. N. Analyzing Reaction Rates with the Distortion/Interaction-Activation Strain Model. *Angew. Chemie - Int. Ed.* **2017**, *56* (34), 10070–10086. https://doi.org/10.1002/anie.201701486.

(136) Bickelhaupt, M.; Bickelhaupt, M. Understanding Reactivity with Kohn•Sham Molecular Orbital Theory: E2•S. *J. Comput. Chem.* **1999**, *20*, 114–128.

(137) Fernández, I.; Bickelhaupt, F. M. The Activation Strain Model and Molecular Orbital Theory: Understanding and Designing Chemical Reactions. *Chem. Soc. Rev.* **2014**, *43* (14), 4953–4967. https://doi.org/10.1039/c4cs00055b.

(138) Wolters, L. P.; Bickelhaupt, F. M. The Activation Strain Model and Molecular Orbital Theory. *Wiley Interdiscip. Rev. Comput. Mol. Sci.* **2015**, *5* (4), 324–343. https://doi.org/10.1002/wcms.1221.

(139) Brintzinger, H. H.; Fischer, D.; Mülhaupt, R.; Rieger, B.; Waymouth, R. M. Stereospecific Olefin Polymerization with Chiral Metallocene Catalysts. *Angew. Chemie Int. Ed. English* **1995**, *34* (11), 1143–1170. https://doi.org/10.1002/anie.199511431.

(140) Wegener, G.; Brandt, M.; Duda, L.; Hofmann, J.; Klesczewski, B.; Koch, D.; Kumpf, R. J.; Orzesek, H.; Pirkl, H. G.; Six, C.; et al. Trends in Industrial Catalysis in the Polyurethane Industry. *Appl. Catal. A Gen.* **2001**, *221* (1–2), 303–335. https://doi.org/10.1016/S0926-860X(01)00910-3.

(141) Lipinski, B. M.; Morris, L. S.; Silberstein, M. N.; Coates, G. W. Isotactic Poly(Propylene Oxide): A Photodegradable Polymer with Strain Hardening Properties. *J. Am. Chem. Soc.* **2020**. https://doi.org/10.1021/jacs.0c01768.

(142) Peretti, K. L.; Ajiro, H.; Cohen, C. T.; Lobkovsky, E. B.; Coates, G. W. A Highly Active, Isospecific Cobalt Catalyst for Propylene Oxide Polymerization. *J. Am. Chem. Soc.* **2005**,

127 (33), 11566–11567. https://doi.org/10.1021/ja053451y.

(143) Ajiro, H.; Peretti, K. L.; Lobkovsky, E. B.; Coates, G. W. On the Mechanism of Isospecific Epoxide Polymerization by Salen Cobalt(III) Complexes: Evidence for Solid-State Catalysis. *Dalt. Trans.* **2009**, No. 41, 8828–8830. https://doi.org/10.1039/b914573g.

(144) Hirahata, W.; Thomas, R. M.; Lobkovsky, E. B.; Coates, G. W. Enantioselective Polymerization of Epoxides: A Highly Active and Selective Catalyst for the Preparation of Stereoregular Polyethers and Enantiopure Epoxides. *J. Am. Chem. Soc.* **2008**, *130* (52), 17658–17659. https://doi.org/10.1021/ja807709j.

(145) Thomas, R. M.; Widger, P. C. B.; Ahmed, S. M.; Jeske, R. C.; Hirahata, W.; Lobkovsky, E. B.; Coates, G. W. Enantioselective Epoxide Polymerization Using a Bimetallic Cobalt Catalyst. *J. Am. Chem. Soc.* **2010**, *132* (46), 16520–16525. https://doi.org/10.1021/ja1058422.

(146) Childers, M. I.; Longo, J. M.; Van Zee, N. J.; Lapointe, A. M.; Coates, G. W. Stereoselective Epoxide Polymerization and Copolymerization. *Chem. Rev.* **2014**, *114* (16), 8129–8152. https://doi.org/10.1021/cr400725x.

(147) Hustad, P. D.; Kuhlman, R. E.; Carnahan, E. M.; Wenzel, T. T.; Arriola, D. J. An Exploration of the Effects of Reversibility in Chain Transfer to Metal in Olefin Polymerization. *Macromolecules* **2008**, *41* (12), 4081–4089. https://doi.org/10.1021/ma800357n.

(148) Arriola, D. J.; Carnahan, E. M.; Hustad, P. D.; Kuhlman, R. L.; Wenzel, T. T. Catalytic Production of Olefin Black CoPolymers via Chain Shuttling Polymerization. *Science (80-.).* **2006**, *312* (5774), 714–719. https://doi.org/10.1126/science.1125268.

(149) Sita, L. R. Ex Uno Plures ("Out of One, Many"): New Paradigms for Expanding the Range of Polyolefins through Reversible Group Transfers. *Angew. Chemie - Int. Ed.* **2009**, *48* (14), 2464–2472. https://doi.org/10.1002/anie.200802661.

(150) Konsler, R. G.; Karl, J.; Jacobsen, E. N. Cooperative Asymmetric Catalysis with Dimeric Salen Complexes [11]. *J. Am. Chem. Soc.* **1998**, *120* (41), 10780–10781. https://doi.org/10.1021/ja982683c.

(151) Morris, L. S.; Childers, M. I.; Coates, G. W. Bimetallic Chromium Catalysts with Chain Transfer Agents: A Route to Isotactic Poly(Propylene Oxide)s with Narrow Dispersities. *Angew. Chemie - Int. Ed.* **2018**, *57* (20), 5731–5734. https://doi.org/10.1002/anie.201801380.

(152) Milgrom, J. Method of Making a Polyether Using a Double Metal Cyanide Complex Compound, 1966.

(153) Pruitt, M. E.; Jackson, L.; Bagett, J. M. Catalysts for the Polymerization of Olefin Oxides. **1955**, 3.

(154) Cohen, C. T.; Chu, T.; Coates, G. W. Cobalt Catalysts for the Alternating Copolymerization of Propylene Oxide and Carbon Dioxide: Combining High Activity and Selectivity. *J. Am. Chem. Soc.* **2005**, *127* (31), 10869–10878. https://doi.org/10.1021/ja051744l.

(155) Nielsen, L. P. C.; Stevenson, C. P.; Blackmond, D. G.; Jacobsen, E. N. Mechanistic Investigation Leads to a Synthetic Improvement in the Hydrolytic Kinetic Resolution of Terminal Epoxides. *J. Am. Chem. Soc.* **2004**, *126* (5), 1360–1362. https://doi.org/10.1021/ja038590z.

(156) Nielsen, L. P. C.; Zuend, S. J.; Ford, D. D.; Jacobsen, E. N. Mechanistic Basis for High Reactivity of (Salen)Co-OTs in the Hydrolytic Kinetic Resolution of Terminal Epoxides. *J. Org. Chem.* **2012**, *77* (5), 2486–2495. https://doi.org/10.1021/jo300181f.

(157) Cohen, C. T.; Thomas, C. M.; Peretti, K. L.; Lobkovsky, E. B.; Coates, G. W. Copolymerization of Cyclohexene Oxide and Carbon Dioxide Using (Salen)Co(Iii) Complexes: Synthesis and Characterization of Syndiotactic Poly(Cyclohexene Carbonate). *J. Chem. Soc. Dalt. Trans.* **2006**, *60* (11), 237237–249249. https://doi.org/10.1039/b513107c.

(158) Palucki, M.; Finney, N. S.; Pospisil, P. J.; Güler, M. L.; Ishida, T.; Jacobsen, E. N. The Mechanistic Basis for Electronic Effects on Enantioselectivity in the (Salen)Mn(III)-Catalyzed Epoxidation Reaction. *J. Am. Chem. Soc.* **1998**, *120* (5), 948–954. https://doi.org/10.1021/ja973468j.

(159) Norrby, P. O.; Linde, C.; Åkermark, B. On the Chirality Transfer in the Epoxidation of Alkenes Catalyzed by Mn(Salen) Complexes. *J. Am. Chem. Soc.* **1995**, *117* (44), 11035–11036. https://doi.org/10.1021/ja00149a038.

(160) Jacobsen, E. N.; Zhang, W.; Güler, M. L. Electronic Tuning of Asymmetric Catalysts. *J. Am. Chem. Soc.* **1991**, *113* (17), 6703–6704. https://doi.org/10.1021/ja00017a069.

(161) Darensbourg, D. J.; Phelps, A. L. Effective, Selective Coupling of Propylene Oxide and Carbon Dioxide to Poly(Propylene Carbonate) Using (Salen)CrN3 Catalysts. *Inorg. Chem.* **2005**, *44* (13), 4622–4629. https://doi.org/10.1021/ic050443+.

(162) Ford, D. D.; Nielsen, L. P. C.; Zuend, S. J.; Musgrave, C. B.; Jacobsen, E. N. Mechanistic Basis for High Stereoselectivity and Broad Substrate Scope in the (Salen)Co(III)-Catalyzed Hydrolytic Kinetic Resolution. *J. Am. Chem. Soc.* **2013**, *135* (41), 15595–15608. https://doi.org/10.1021/ja408027p.

(163) Diciccio, A. M.; Longo, J. M.; Rodríguez-Calero, G. G.; Coates, G. W. Development of Highly Active and Regioselective Catalysts for the Copolymerization of Epoxides with Cyclic Anhydrides: An Unanticipated Effect of Electronic Variation. *J. Am. Chem. Soc.* **2016**, *138* (22), 7107–7113. https://doi.org/10.1021/jacs.6b03113.

(164) Van Zee, N. J.; Sanford, M. J.; Coates, G. W. Electronic Effects of Aluminum Complexes in the Copolymerization of Propylene Oxide with Tricyclic Anhydrides: Access to Well-

Defined, Functionalizable Aliphatic Polyesters. *J. Am. Chem. Soc.* **2016**, *138* (8), 2755–2761. https://doi.org/10.1021/jacs.5b12888.

(165) Weigend, F.; Ahlrichs, R. Balanced Basis Sets of Split Valence, Triple Zeta Valence and Quadruple Zeta Valence Quality for H to Rn: Design and Assessment of Accuracy. *Phys. Chem. Chem. Phys.* **2005**, *7* (18), 3297–3305. https://doi.org/10.1039/b508541a.

(166) Grimme, S.; Antony, J.; Ehrlich, S.; Krieg, H. A Consistent and Accurate Ab Initio Parametrization of Density Functional Dispersion Correction (DFT-D) for the 94 Elements H-Pu. *J. Chem. Phys.* **2010**, *132* (15). https://doi.org/10.1063/1.3382344.

(167) Schuchardt, K. L.; Didier, B. T.; Elsethagen, T.; Sun, L.; Gurumoorthi, V.; Chase, J.; Li, J.; Windus, T. L. Basis Set Exchange: A Community Database for Computational Sciences. *J. Chem. Inf. Model.* **2007**, *47* (3), 1045–1052. https://doi.org/10.1021/ci600510j.

(168) Ahmed, S. M.; Poater, A.; Childers, M. I.; Widger, P. C. B.; Lapointe, A. M.; Lobkovsky, E. B.; Coates, G. W.; Cavallo, L. Enantioselective Polymerization of Epoxides Using Biaryl-Linked Bimetallic Cobalt Catalysts: A Mechanistic Study. *J. Am. Chem. Soc.* **2013**, *135* (50), 18901–18911. https://doi.org/10.1021/ja409521z.

(169) Widger, P. C. B.; Ahmed, S. M.; Hirahata, W.; Thomas, R. M.; Lobkovsky, E. B.; Coates, G. W. Isospecific Polymerization of Racemic Epoxides: A Catalyst System for the Synthesis of Highly Isotactic Polyethers. *Chem. Commun.* **2010**, *46* (17), 2935–2937. https://doi.org/10.1039/b926888j.

(170) Widger, P. C. B.; Ahmed, S. M.; Coates, G. W. Exploration of Cocatalyst Effects on a Bimetallic Cobalt Catalyst System: Enhanced Activity and Enantioselectivity in Epoxide Polymerization. *Macromolecules* **2011**, *44* (14), 5666–5670. https://doi.org/10.1021/ma201078m.

(171) Hansch, C.; Leo, A.; Taft, R. W. A Survey of Hammett Substituent Constants and Resonance and Field Parameters. *Chem. Rev.* **1991**, *91* (2), 165–195. https://doi.org/10.1021/cr00002a004.

(172) Ren, W.; Zhang, W.; Lu, X. Highly Regio-and Stereo-Selective Copolymerization of CO2 with Racemic Propylene Oxide Catalyzed by Unsymmetrical (S,S,S)-SalenCo(III) Complexes. *Sci. China Chem.* **2010**, *53* (8), 1646–1652. https://doi.org/10.1007/s11426-010-4049-1.